On the Identification and Mitigation of Life-limiting Mechanisms of Ionic Liquid Ion Sources Envisaged for Propulsion of Microspacecraft

by

Natalya Anna Brikner

Submitted to the Department of Aeronautics and Astronautics
in partial fulfillment of the requirements for the degree of

Doctor of Philosophy in Aeronautics and Astronautics

at the

MASSACHUSETTS INSTITUTE OF TECHNOLOGY

February 2015

Signature redacted

Author .....
Department of Aeronautics and Astronautics
Signature redacted January 29, 2015

Certified by .....
Paulo C. Lozano
Associate Professor of Aeronautics and Astronautics
Thesis Supervisor

Signature redacted

Certified by .....
Jeffrey H. Lang
Professor of Electrical Engineering
Committee Member

Signature redacted

Certified by .....
Manuel Martínez-Sánchez
Professor Emeritus of Aeronautics and Astronautics
Committee Member

Signature redacted

Accepted by .....
Paulo C. Lozano
Chairman, Aeronautics and Astronautics Committee on Graduate Theses

On the Identification and Mitigation of Life-limiting Mechanisms of Ionic Liquid Ion Sources Envisaged for Propulsion of Microspacecraft

by

Natalya Anna Brikner

Submitted to the Department of Aeronautics and Astronautics
on January 29, 2015, in partial fulfillment of the
requirements for the degree of
Doctor of Philosophy in Aeronautics and Astronautics

Abstract

Life-limiting processes affecting ionic liquid ion sources (ILIS) are investigated in this research, motivated by the development of ILIS for propulsion of microspacecraft and other industrial applications. Micropropulsion in particular has received considerable interest in recent years due to the increasing utility of and demand for small satellites and the services they provide. A passively-fed, porous ILIS system which includes the ion thruster head, propellant supply system, and power electronics has been proposed by researchers in the Space Propulsion Laboratory at the Massachusetts Institute of Technology to address the gap in micropropulsion and provides the primary impetus for the work presented in this thesis.

Spacecraft mission durations can reach up to 15 years with ongoing propulsion requirements and in ground-based applications, minimal servicing to replace the ion source is desirable. Thus, any embodiment of ILIS would benefit from operational lifetimes in excess of 1000 h. To date, successful long-duration operation of porous ILIS beyond tens of hours has not been achieved, precluded primarily by two critical challenges: electrochemistry and electrical discharges. Electrochemistry—chemical reactions between the source emitter and the ionic liquid—has been shown to be capable of fully deteriorating the source in fewer than 100 h. Electrical discharges, on the other hand, can cause source failure within a matter of seconds and are also challenging to predict and avoid. ILIS as a subcomponent of a larger spacecraft system exposed to the environment of space must also overcome challenges such as

radiation and threats of micrometeorite impact. This research aims to investigate, quantify, and mitigate the primary life-limiting mechanisms of ILIS to support their successful long-life operation.

A description of the onset of electrochemistry is applied to ILIS, and it is shown that existing methods for preventing electrochemistry would present a challenge to the drive electronics, requiring alternation of the polarity applied to the devices at kilohertz frequency. The relevance of an alternative contact method is revealed—the distal contact, which is shown to be effective at avoiding electrochemistry at the critical emission site. By contrast, a metal emitter with the traditional, direct electrical contact was electrochemically etched as it operated for a similar time and conditions, showing severe degradation. The distal technique has been implemented in the current version of the MIT propulsion system and more in-depth studies are ongoing to aid in distal electrode material selection and design.

The source of another severe life-limiting mechanism was unknown prior to this work, but was known to be capable of causing device failure within seconds through electrical shorting, material ablation, polycondensation of the ionic liquid, and so on. Experiments performed as part of this effort revealed that electrical discharges were transpiring under certain conditions and inducing these source failures. An analytical framework for predicting the steady-state discharge is outlined for ILIS, though the process is likely complicated by the electrohydrodynamic interactions during porous ILIS operations. Given this difficulty, an experimental study was undertaken to preliminarily explore the operational and design conditions that support discharges so that they may be avoided in practical implementations and to guide future modeling efforts. Gas contamination and flooding of the substrate or unrestricted flow from the porous substrate are identified as the likely factors leading to this failure mechanism. Qualitative descriptions of those processes are provided along with suggestions for techniques for preventing them.

The work concludes with a summary of other life-limiting mechanisms such as grid erosion and micrometeorite impact. Suggestions for future work related to electrochemistry include optimizing the distal electrode material properties, and understanding gas evolution there. For electrical discharges, an experimental study that resolves the challenges of the setup presented could provide more detail to the actual processes by helping to identify the ionized species. It is the hope of the author that the work discussed here and the work to come on mitigating these processes will contribute to the successful embodiment of ILIS as an appealing option for micropropulsion and for ground-based applications.

Thesis Supervisor: Paulo C. Lozano

Title: Associate Professor of Aeronautics and Astronautics

Acknowledgments

There are several people in my life without whom I never would have reached this milestone. My family has been supportive and encouraging, and provided a compelling excuse to take a break to visit them at home in Oregon when work was especially challenging. Thanks for letting me come home and sleep the whole time, Family. My lab mate and dear friend, Louis, never failed to offer a hand on days I couldn't finish everything myself, whether it was printing drafts of this document or dicing wafers. And I am grateful for my boyfriend and the lifelong friends I made from MIT, who provided sounding boards for ideas and presentations as well as much-needed companionship in the form of yoga classes and ice cream breaks.

I would like to thank my committee members Profs. Manuel Martínez-Sánchez and Jeffrey Lang and my thesis readers Dr. Vadim Khayms and Mr. John Dankanich for providing support, poking holes in my arguments, and pointing me in the right direction when I was stuck. I will forever be grateful to my research advisor Prof. Paulo Lozano for his encouragement, friendship, and guidance throughout my doctoral work. I will always search for ways to pay forward the opportunities he afforded me, and will strive to emulate his enduring positive attitude and desire to keep learning. And if not for my research advisor at Duke University, Prof. Jon Protz, I would not have come to MIT in the first place to work in a field I continue to be truly passionate about.

Most of my tenure at MIT was supported through the National Science Foundation's Graduate Research Fellowship Program, the Asian Office of Aerospace Research and Development, and NASA. The Aeronautics and Astronautics Department at MIT provided support I am thankful for as well, including Beth Marois's help navigating the logistics of graduate school. Lastly, I would like to thank Flour Bakery

for supplying the caffeine that made this document possible.

Contents

List of Figures

List of Tables

Chapter 1

Introduction

1.1 Motivation

The last decade has brought about several financial, technological, and industrial changes: rapid advances in manufacturing and integrated circuit technology, increasing demand for global communications and "big data" from persistent Earth coverage, and a transition in the space industry from government to the private sector. In response, the space industry has seen a shift away from large, multi-billion dollar satellites toward smaller yet increasingly capable platforms. Compared to their conventional counterparts, small satellites afford shorter development and manufacturing timelines, less expensive launches, the opportunity for rapid redesign and redeployment, and a growing inventory of modular, standardized off-the-shelf components. These factors are having the effect of extending access to space to existing and emerging firms, countries, and markets.

Lagging behind the miniaturization of electronics is the miniaturization of in-space propulsion systems. Electric propulsion, which is often preferred for higher-

ΔV missions because of the potential for significant propellant weight-savings, has proven very difficult to miniaturize. Chemical propulsion is often prohibited from launch on small satellite rideshare launches; varieties that are less dangerous tend to be comparatively inefficient. As a result, a majority of CubeSats—an increasingly popular class of small satellite, commonly comprised of one to six units, each 10 cm $\times$ 10 cm $\times$ 10 cm (see Figure 1-1)—launched to date have been done so without propulsion.

Figure 1-1: A 3U CubeSat, a common form factor used by organizations like Planet Labs, universities, and the government [1].

In the best case, this critical lack of functionality results in significant missed revenues; in the worst case, it renders promising space missions untenable. The intent of this research has been to support the development of the ion electrospray propulsion technology under development in the Space Propulsion Laboratory (SPL) at the Massachusetts Institute of Technology (MIT) that addresses this technological gap. Concepts for a spacecraft thruster based on such a technology were first demonstrated by Legge and Lozano [18]; in subsequent years, several prototypes incorporating various technological and design improvements have been built and

tested, and the work is ongoing today.

In this thesis, we present thorough analytic and experimental investigations into the most severe life-limiting challenges facing ILIS development for long-life operation, as well as strategies for their mitigation, with the objective of enabling small satellites and providing an alternative to current technologies for large satellites.

1.1.1 Space propulsion overview

Space propulsion refers to the acceleration of a spacecraft that is already in orbit, and is distinct from the propulsion used for launch. The momentum for acceleration is obtained through the expulsion of mass that is carried onboard the spacecraft[1]; the energy for expulsion can be obtained from stored chemical energy that heats and accelerates a gas through a nozzle (chemical propulsion), or an onboard power supply that utilizes electrical energy to accelerate charged particles (electric propulsion).

Basic propulsion metrics

In order to understand the challenges facing small satellites, it is helpful to develop a working knowledge of fundamental propulsion metrics. Here, we present an abbreviated introduction to important quantities; Jahn [19] and Sutton [20] offer thorough derivations of these terms and more.

The thrust from an in-space propulsion system is

$$F = \dot{m}_p \bar{c} \tag{1.1}$$

[1]There are some niche propulsion technologies such as solar sails and tethers that do not expel mass that was carried onboard the spacecraft. Given the high mass penalties particularly for interplanetary travel, these technologies may become increasingly relevant.

where $\dot{m}_p$ is the portion of propellant mass flow contributing to thrust and $\bar{c}$ is the average exhaust velocity. Specific impulse, I_{sp}, is a measure of propellant economy for propulsion systems. For constant $\bar{c}$,

$$I_{sp} = \frac{\bar{c}}{g} \tag{1.2}$$

The efficiency with which the system converts electrical power, P_{in}, into propulsive power, P_{prop}, is given as

$$\eta_T = \frac{P_{prop}}{P_{in}} = \frac{\frac{1}{2}\dot{m}_p \bar{c}^2}{IV} \tag{1.3}$$

Equations 1.1–1.3 provide a basis for evaluating propulsion systems for various missions. These quantities in turn elucidate several other considerations for designers:

1. Required power draw for a desired thrust level,

$$P_{in} = \frac{Fc}{2\eta_T} \tag{1.4}$$

   This power must be supplied from onboard batteries or solar panels, the amount of which can be carried within small satellite volume and mass constraints is rather limited.

2. Required fraction of propellant mass to total spacecraft mass,

$$\frac{m_p}{m_o} = 1 - e^{-\Delta V / I_{sp} g}; \tag{1.5}$$

   More efficient mass utilization permits lower propellant and higher payload mass fractions.

3. Total mission time to achieve mission ΔV,

$$t = \int \frac{m}{F} dV \tag{1.6}$$

Mission time affects the total realized operational (which is oftentimes synonymous with profitable) lifetime of satellites, but is often sacrificed for cost or mass savings.

Other key quantities mission designers consider that are not given by the above equations are total system mass, volume, and price.

Table 1.1 shows the specific impulse, input power, efficiency range, and propellant for thrusters with flight heritage and some in the developmental phase [7, 13, 14].

Differences between electric and chemical propulsion systems

Fundamentally, chemical and electric propulsion differ in two regards: the energy source that ultimately provides kinetic energy for accelerating the spacecraft, and the momentum-exchange media. It is nearly impossible to optimize propulsion metrics across generalized missions because of the intricate interplay between stakeholders, subsystem or component performance and reliability, and various objectives and requirements. We provide the following example to illustrate various trades between performance and drivers.

Let us compare the required propellant mass fraction (Equation 1.5) and total mission time (Equation 1.6) over a range of ΔV for both an Aerojet Rocketdyne XR-5 electric Hall thruster (I_{sp} = 2000 s, F = 0.282 N [21]) and an Aerojet Rocketdyne MR-104 chemical monopropellant system (I_{sp} = 230 s, F = 300 N [22]). Figure 1-2 shows that over the entire range of ΔV, the electric propulsion option takes 1000 times longer than the chemical system (t scales linearly with thrust for constant

Table 1.1: A limited survey of performance of propulsion systems, including those with flight heritage and those in the developmental stage (indicated by †) [7, 13, 14].

Thruster	Specific Impulse (s)	Input Power (kW)	Efficiency Range (%)	Propellant
Cold gas	50-75	—	—	Various
Chemical (monopropellant)	150-225	—	—	N_2H_4, H_2O_2
Chemical (bipropellant)	300-450	—	—	Various
Resistojet	300	0.5-1	65-90	N_2H_4 monoprop
Arcjet	500-600	0.9-2.2	25-45	N_2H_4 monoprop
Ion thruster	2500-3600	0.4-4.3	40-80	Xenon
Hall thruster	1500-2000	1.5-4.5	35-60	Xenon
PPTs	850-1200	<0.2	7-13	Teflon
Ion Electrospray (MIT)†	800-3500	60e-6	50-70	Various
DSSP thruster†	<900	1e-4–23e-4		Solid
Warm gas (VACCO)†	70	.015	13	Warm gas

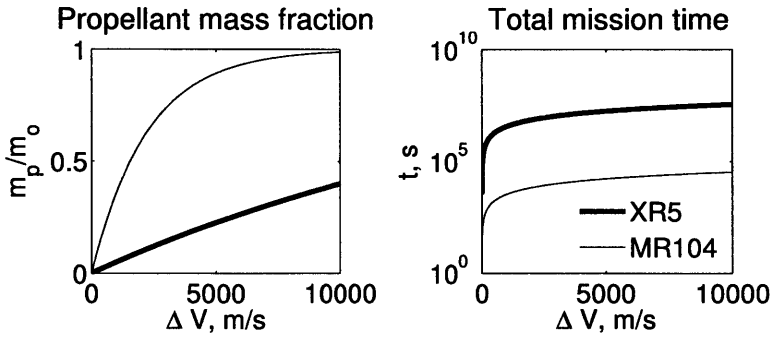

Figure 1-2: Comparison of XR-5 to MR-104 propellant mass fraction and total mission time in seconds for a range of ΔV. $m_o = 1000$ kg.

m); however, for higher ΔV values, nearly all of the wet mass of the spacecraft must be propellant in the chemical system scenario. These trades are frequently at odds, complicating subsystem design for manufacturers, and subsystem selection for mission designers.

1.1.2 Challenges for small satellite propulsion

Medium and large satellites (150-1000+ kg) enjoy a wide range of commercially-available electric and chemical propulsion systems that meet their mission requirements, and are comparatively unencumbered by restrictions imposed by launch providers. Small satellites (1-50 kg), on the other hand, are extremely constrained by available propulsion systems. Mueller, Hofer, and Ziemer [23] provide a review of state of the art propulsion systems and their applicability to CubeSats. Mono- and bipropellant systems are prohibited from launch because of the risk of explosion. Cold gas systems are simple and inexpensive, but characteristically low I_{sp} means a large quantity of propellant must be carried onboard and expended. This dearth of options has forced manufacturers to launch small satellites without any propulsion, leading to shortened lifetimes, lack of orbit transfer capability, and untenable missions.

Example: Deorbiting a CubeSat

End-of-life deorbit typifies many of the limitations and suboptimal trades designers must make for small satellite missions. Current National Aeronautics and Space Administration (NASA) regulations (NASA-STD-8719.14A) require that satellites be transferred to a graveyard orbit or reentered through Earth's atmosphere within 25 years from launch [24]. Without an onboard propulsion system for deorbit, this

regulation implies that CubeSats must be launched to orbits below roughly 600 km—the highest altitude from which they will naturally deorbit within the allowable time due to the non-negligible atmospheric drag forces at 600 km and below. Missions that require higher orbits, orbits where collisions are less likely, or those to which launch opportunities may be more frequent are thereby precluded.

An onboard propulsion system would permit a downward spiral orbit transfer to 300 km (drag forces at 300 km are strong enough to cause reentry within 10 days, see Equation 1.7) within hundreds of days from most reasonable CubeSat orbits (<1200 km). Natural deorbit time versus altitude is compared to deorbit with an electric propulsion system, calculated from Equation 1.7, in Figure 1-3 for a 3-kg spacecraft with $I_{sp} = 1800$ s and $\eta = .75$, showing the relative quickness with which a CubeSat with a propulsion system can be deorbited.

$$t = \frac{mgI_{sp}}{F}\left(1 - e^{-\frac{\Delta V}{gI_{sp}}}\right) \tag{1.7}$$

Example: Detumbling a CubeSat

Another promising application of CubeSat propulsion is detumble after a perturbation or spacecraft separation. Assume the thrust vector configuration in Figure 1-4(a). The torque imparted on the spacecraft about its central axis causes a change in rotational speed in time given by

$$\Delta\dot{\theta} = \frac{3Ft}{ma} \tag{1.8}$$

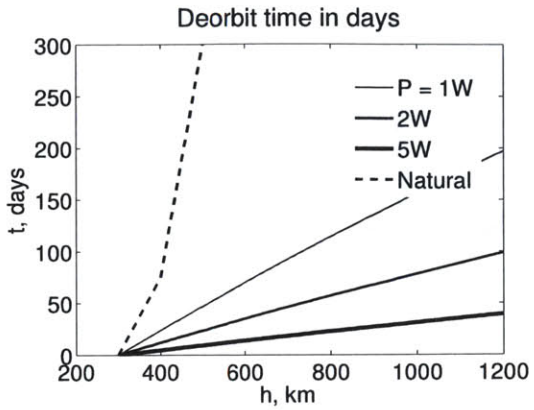

Figure 1-3: Time in days to deorbit (spiral to 300 km) a CubeSat versus initial orbit altitude for several power levels, compared to a natural deorbit. For the powered deorbits, $m = 3$ kg, $I_{sp} = 1800$ s, and $\eta = .75$.

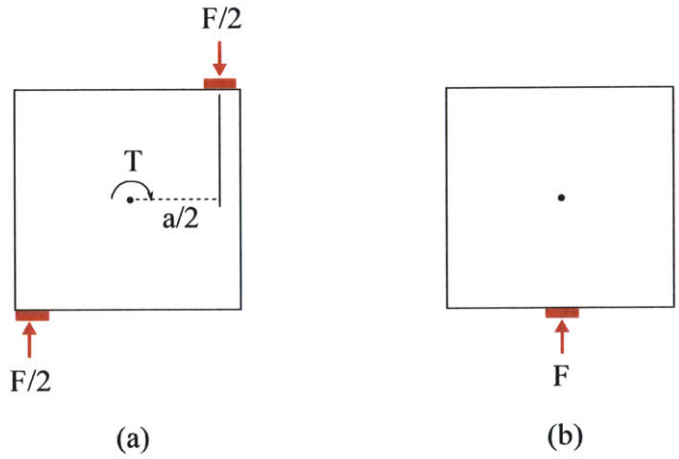

Figure 1-4: Possible thrust vector configurations for missions such as (a) slewing or detumble, and (b) deorbit or orbit raising.

where a is the length of the moment arm. For a CubeSat launched to orbit with some initial spin about its central axis, and for $m = 1$ kg, the time to stop the spin from 1 Hz is 1.7 hrs, and 2 Hz in 3.3 hrs. These times are relatively short compared to the total expected lifetime of CubeSats launched at the time of this writing (2–3 years).

Propulsion systems that will fill this technological gap face a different set of requirements than those for large satellites. Suitable options must be relatively low-power, light and compact, and free of explosive or volatile propellants. To meet demand in the growing university and developing nation satellite markets, they must also be low-cost. A novel type of ion propulsion, introduced in the following section, offers a solution that addresses these critical requirements for small satellite propulsion systems.

1.2 Porous ionic liquid ion sources: a subclass of electrospray

Electrosprays make use of strong electric fields to extract streams of charged particles from conductive liquids, most of the time held at the tip of a sharp emitter electrode over which a Taylor cone forms—an equipotential surface deformation that results from the balance between electric and surface tension forces (Figure 1-5) [25]:

$$\frac{1}{2}\epsilon_o E_n^2 = k\gamma - P_c \approx k\gamma \tag{1.9}$$

where $k = \cot\theta/r$, γ is the surface tension of the liquid, and P_c is the internal liquid pressure which is assumed to be negligible. At the apex of a Taylor cone, the electric field intensity is such that emission of charged species occurs. The species are emitted

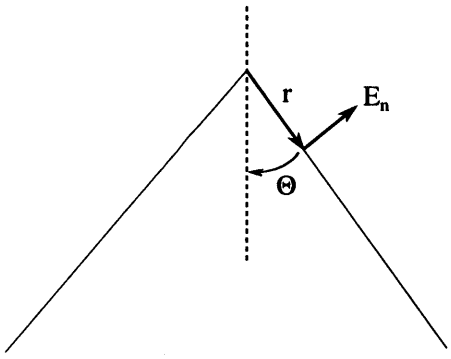

Figure 1-5: Schematic of Taylor cone geometry.

in the form of charged droplets (colloid electrospray), pure ions (ion electrospray), or a mixture of both.

Colloid emission was first observed in the early 20th century during Zeleny's experiments on cone-jet formations of ethyl alcohol and glycerol [26]. The technique has since been widely used in analytical chemistry as a means of obtaining intact macromolecules [27].

Emission of beams of pure ions was achieved using liquid metals such as cesium, gallium, and indium since the 1960s [28, 29, 30, 31]. Being highly conductive, these liquid metal ion sources (LMIS) emit pure ions without the formation of a cone jet or droplet spray. High surface tensions require starting potentials on the order of 2 kV and operating potentials greater than 4 kV which can be cumbersome to generate and manage onboard a spacecraft.

Emission in the purely ionic regime from conductive liquids was reported by Romero [32] in capillary emitters, followed by a series of works in externally wetted tungsten [33] and porous nickel [34]. The technique has been suggested for fabrication of microelectromechanical systems (MEMS) devices via maskless direct writing of materials [35], other focused ion beam applications [36, 37], and micro propulsion of

spacecraft [38, 39].

1.2.1 ILIS principles

Ionic liquid ion sources (ILIS) are a subclass of electrosprays that produce jets of pure ions from electrically-stressed conductive ionic liquids. At the apex of the Taylor cone the field is intensified (on the order of 1 V/nm) [32], prompting field emission of ions (Figure 1-6).

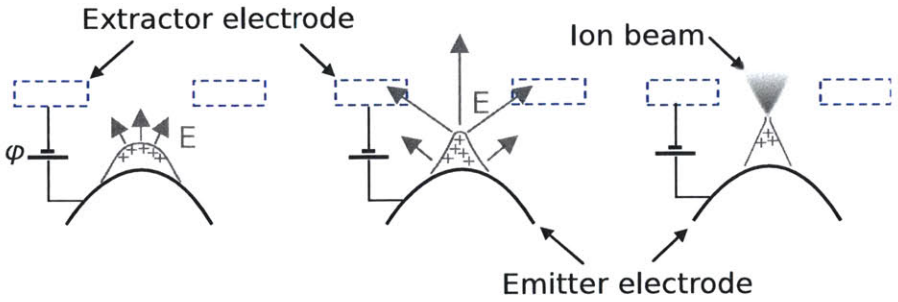

Figure 1-6: The process of Taylor cone formation and ion emission, shown sequentially for increasing ϕ until emission is achieved.

Ionic liquids (ILs), room temperature molten salts composed exclusively of positive and negative ions, are preferred over other conductive media (such as liquid metals) for some applications where lower startup potentials are desired, or ease of storage and handling is crucial. Additionally, near-negligible vapor pressures [40] permit pure ion electrospray from ILs in vacuum, thereby enabling operation in space. Furthermore, a considerable catalog of ILs exists, with new liquids being synthesized often, permitting the tailoring of ion properties for desired performance. Properties of several ionic liquids used for testing are given in Table 1.2.

Table 1.2: Properties of ILs used in ILIS [15].

Liquid	K (S/m)	ρ (g/cm^3)	γ (dyn/cm)	M^+ (amu)	M^- (amu)
EMI-N(CN)2	2.8	1.08	49.05	111.2	66
EMI-2.3HF	10	1.13		111.2	59, 79
EMI-BF_4	1.36	1.24	45.2	111.2	86.8
EMI-C(CN)3	2.2	1.11	47.9	111.2	90.1
EMI-GaCl4	2.2	1.53	48.6	111.2	211.5
EMI-Im	0.84	1.52	41.6	111.2	280.1

1.2.2 Applications of ILIS

ILIS in focused ion beam applications

ILIS are appealing alternatives to traditional focused ion beam (FIB) sources such as gallium that are used for: scanning ion microscopy; lithography, particularly on sensitive media; ion implantation and injection of reactive gases and metallic precursors; and localized engraving or device editing [37]. They are capable of emitting positive or negative ions, thereby avoiding substrate charging; operation at room temperature in vacuum simplifies design and can increase the source lifetime; and an immense catalog of ionic liquids exists that allows for emitted species that can be tailored for particular applications. Additionally, ILIS are characterized by low energy spreads [41, 42] and can operate at low currents, thereby lessening spherical and chromatic aberrations. Lastly, some ILs contain species that form volatiles with the substrate material, resulting in an increased etching rate over other FIB tools [2].

Perez *et al.* [2] demonstrated an ILIS for micro fabrication of silicon structures. The setup is shown in Figure 1-7. Figure 1-8 shows the pattern etched by the source with the ionic liquid 1-ethyl-3-methylimidazolium tetrafluoroborate (EMI-BF_4) operated at 1 μA and 15 keV for 0.5 h. The mean depth measured was 24 ($\pm$ 5) nm, giving a sputtering yield of 35 silicon atoms per incident ion. This yield is

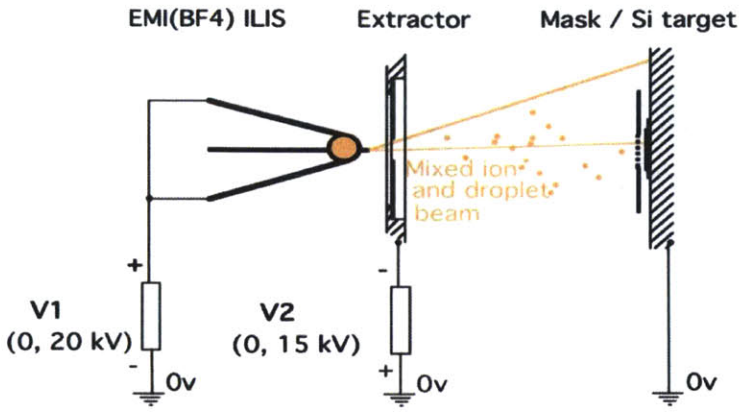

Figure 1-7: Schematic of an ILIS used to etch micro-features onto a silicon wafer [2].

particularly interesting, as it is significantly higher than yields typical of similarly-configured gallium FIB [43]), suggesting a chemical enhancement of the sputtering process. The process in [2] used a mask for patterning, though one could easily envisage future implementations where a mask-free pencil-like writing process is used with the source mounted on a mobile stage.

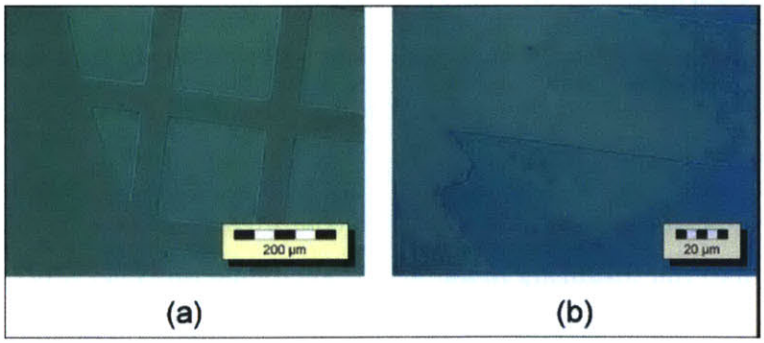

Figure 1-8: (a) Optical microscopy image of the pattern engraved into the silicon sample by the ILIS using EMI-BF_4 (15 kV, 1 μA); (b) detail of a transferred structure revealing clear submicron details assessing the excellent stability of the emission process [2].

Micropropulsion of spacecraft

Benefits such as high efficiency and precise current control, all realizable on the micro-scale, have led to the investigation of ILIS as a means of providing the momentum exchange to propel microspacecraft [38, 39]. The research group in the Space Propulsion Laboratory (SPL) is developing an ion Electrospray Propulsion System (iEPS), derived from ILIS technology. The concept incorporates hundreds of emitter tips microfabricated from a porous substrate, each capable of supporting at least one ion emission site that produces $\sim 0.1\mu$N thrust and whose geometry is prescribed to lower the required emission potential as compared to a flat surface and to minimize interception with the extractor electrode. As a potential is applied to the liquid with respect to the extractor grid, ionic liquid flows from the propellant reservoir toward the emitter tips. Ions are extracted from the tips and accelerated through the grid apertures by the electric field, generating thrust in the opposite direction (Figure 1-9). A passive, unpressurized propellant supply system, made

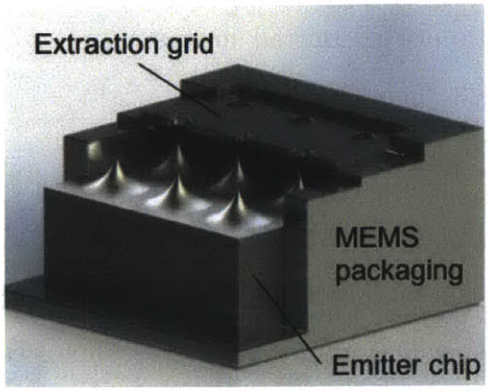

Figure 1-9: iEPS thruster design. Courtesy of D.G. Courtney and F.M. Hicks.

feasible by the porous nature of the design and the negligible vapor pressures of candidate propellants, circumvents launch restrictions and obviates the need for heavy

pressurized tanks. Furthermore, the extraction of positive and negative ions from adjacent sources results in a neutral beam without the need for an external cathode. Lastly, the micro-scale features lend themselves to cost-effective MEMS batch manufacturing.

Beyond design advantages, it is useful to expound on the theoretical performance of ILIS as a propulsion candidate in order to understand the relevant merit of the concept and motivation for its ongoing development. Present day manufacturing, materials, and operational limitations set the likely maximum achievable thrust density to 100 N/m^2, which corresponds to an emitter spacing, or pitch, of 10 μm. For comparison, conventional ion engines produce 1–2 N/m^2 and Hall thrusters 10–100. Even with the current pitch of 450 μm, the ILIS iEPS design achieves comparatively low values of mass- and volume-per-unit-thrust of roughly 10 kg/N and 3 cm^3/mN, respectively. MEMS and batch manufacturing processes help realize lower costs and modular, flexible designs.

For an ion electrospray, the specific impulse is determined by the applied voltage and the charge-to-mass ratio of the emitted species:

$$c_i = \sqrt{2V_e \bar{q}/\bar{m}_i} \tag{1.10}$$

where $\bar{q}/\bar{m}_i$ is the mass-weighted average charge-to-mass ratio for the beam. EMI-BF4 and the "heavier" 1-ethyl-3-methylimidazolium bis(trifluoromethylsulfonyl)imide (EMI-IM) give predicted specific impulse values, assuming singly-charged ions, of 3500 s [32] and 2500 s [42], respectively.

The total thruster efficiency, η_T, takes into account several individual contributions to overall efficiency:

$$\eta_T = \eta_h \eta_{tr}^2 \eta_\theta \eta_E \eta_p \tag{1.11}$$

The transmission efficiency, η_{tr}, accounts for interception of charged particles by solid surfaces; η_i is the ionization efficiency—a measure of the fraction of non-neutral particles emitted by the source; η_θ is a reduction of thrust due to beam divergence; η_E is the beam energy divided by the applied energy; and η_p is the polydispersive efficiency, a result of wasted energy by accelerating particles of dissimilar specific charge. Lozano [44] provides a detailed analysis of the various efficiencies.

1.3 Electrospray thruster development

1.3.1 Background

The application of colloid electrospray to micropropulsion was first introduced in the 1960s: concepts used high extraction voltages (5–15 kV) to produce thrust levels on the order of 0.1–1 mN [45, 46]. Serious consideration of electrospray for propulsion was abandoned after this brief period of exploration due to challenges such as limited propellant selection and the required active feed systems, immature fabrication techniques, competition from ion engines, and high startup voltages that contributed to electrical insulation and power issues.

More recently, electrospray reemerged in Busek Co.'s colloid thruster system design for the Space Technology 7 (ST7) mission, onboard the Laser Interferometer Space Antenna (LISA) spacecraft [47]. The design employs nine actively-fed capillary emitters, and uses an external cathode to neutralize the beam. Other colloid and mixed ion-droplet thrusters have been developed by [48, 49, 50, 51, 52].

Compared to colloid electrospray, ILIS are capable of providing higher specific impulse, but the current produced by a single source is too low to cause a significant

change to the orbit of even the smallest of spacecraft in a reasonable time[2]. By the early 2000s, micro-manufacturing and IL synthesis had advanced to the point that thruster designs could incorporate arrays of hundreds of ILIS, densely patterned on the surfaces of porous substrates. The concept, an ion electrospray propulsion system, was first published by Legge and Lozano [18, 53], and is described in more detail in the following section.

1.3.2 The Ion Electrospray Propulsion System (iEPS)

Courtney [3] developed the first version of the concept of a porous ion Electrospray Propulsion System (iEPS) that is still heavily under development in the SPL today (see Figure 1-9). The thruster system is based on the high ion velocity realized through the ILIS electrospray mechanism, and leverages modern MEMS fabrication techniques for manufacturing the electrodes and packaging. Low flow rates and negligible vapor pressures of ionic liquids allow for passive feeding systems, which can remain exposed to the vacuum of space thereby obviating the need for pressurized propellant tanks or valves, both of which are difficult to miniaturize for small satellites. Ion beams of opposite polarities are always fired together in envisaged implementations for beam neutralization without the need for an external cathode.

Early versions featured porous nickel substrates that were electrochemically etched to produce square centimeter arrays of 480 emitter tips (see Figure 1-10). Each such thruster "chip" was attached to a silicon frame to which the downstream extractor electrode was optically aligned and fixed. Practical implementation of iEPS can include as many as hundreds to thousands of thruster chips arranged side-by-side to achieve a desired thrust level and direction. High-level details of the fabrication and

[2]These low currents and correspondingly low thrust levels may have utility in ultra-precise pointing applications.

assembly process are given in Figure 1-11.

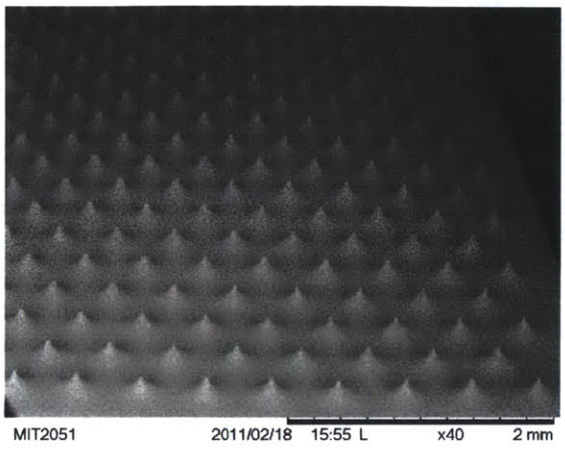

Figure 1-10: Porous nickel array developed for iEPS [3].

Subsequent design iterations have gone on to address issues such as poor electrical isolation, incompatible bonding materials, and so on [54]. A contribution of this thesis (see Section 2.3.1), together with the low repeatability of the electrochemical etching process, provided the impetus for the transition from conductive substrates to dielectrics, which brought with it new manufacturing challenges but will hopefully enable less expensive molding techniques for emitter fabrication in the near term. The current state-of-the-art iEPS device now features borosilicate emitters manufactured by a laser ablation process. The realized packing density is roughly $5 \times 10^6/\mathrm{m}^2$, which corresponds to a thrust density of 0.5 $\mathrm{N/m}^2$. A specific impulse of 1800 s has been demonstrated in the laboratory. Measured power per unit (inferred) thrust is $\sim$ 12 kW/N (not including η_{PE}). Continuous operation for over 70 h has been achieved.

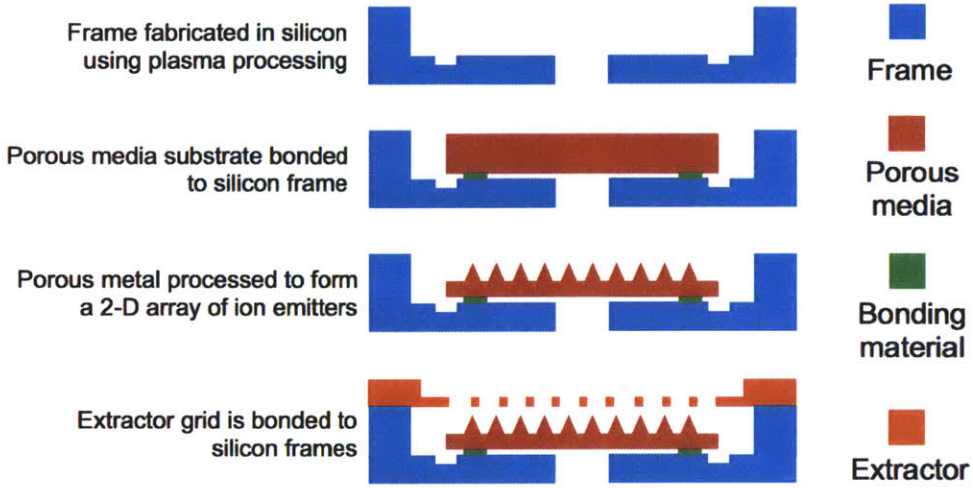

Figure 1-11: High-level schematic of iEPS fabrication process. Beginning from the top, a structurally supporting frame that will provide the mounting interface between the propellant tank and the emitter substrate is fabricated using MEMS techniques; a blank porous substrate is bonded to the frame; the substrate is processed to form an array of micro-emitter structures; a MEMS-fabricated extractor electrode is aligned and bonded to the frame. The port for the tank is visible in the bottom of the frame.

1.3.3 Challenges to long-life operation of ILIS that are addressed through this work

Long thrusting times are typical of missions that employ electric propulsion; operation for upwards of 1000 h is common, making operational lifetime of any propulsion device a critical metric. Other implementations would also benefit from increased lifetimes. Prior to this work, operation of a porous ILIS emitter (the primary component in iEPS devices) for more than 30 h had not been realized, however, owing primarily to two phenomena: electrochemistry and electrical discharges. These life-limiting mechanisms are the focus of this thesis. Other non-trivial challenges include repeatable and cost-effective nano- and micro-scale manufacturing, passive propellant feeding, and efficiency optimization, among others.

Lozano and Martínez-Sánchez [33] identified adverse effects arising from the extraction of ions of one polarity from the ionic liquid while the counterions remained behind. The counterions form a layer of charge over the apex of an ILIS, that, together with charges in the conductive electrode, produces an electrochemical double layer. Upon double layer saturation, chemical reactions that are driven by the externally-applied voltage result in the decomposition of the IL and the corrosion of the electrode. In batteries and fuel cells, electrochemistry is intentionally exploited to produce electricity from chemical reactions; in ILIS, electrochemistry shortens the source lifetime to under 100 h and can lead to other issues such as gas generation and product precipitate.

Observations of dark, carbonaceous deposits on early generations of thrusters were thought to be the result of electrochemistry, but through this work the cause was identified as electrical discharges occurring between the grounded and high voltage electrodes. Adverse effects of discharges included blockage of the pores; shorting of

power supplies, other electronics, and between the electrodes; and, in particularly dramatic events, the complete ablation of the emitter substrate. Discharges are complex phenomena that can cause source failure within seconds.

Other adverse phenomena that affect the lifetime of iEPS in particular are grid erosion due to ion impingement on extractor surfaces, and environmental factors such as radiation and impact from micrometeorites.

1.4 Thesis contributions

The preceding sections expounded on both the promise of small satellites and the need for a solution to critical challenges to the implementation of ionic liquid ion sources as a method for small satellite propulsion. Primary contributions through this work include:

1. **Clear identification and description of electrochemistry as a life-limiting mechanism of ILIS (Section 2.3.2).** Previously, electrochemistry was indicted as the most critical life-limiting mechanism of ILIS, though its effects or onset were not well understood. Long duration tests correlated electrochemistry to source failure, and showed that although limiting, electrochemistry is a gradual failure mechanism, and also was not responsible for the dark residue that had previously been attributed to it.

    (a) **Application and experimental verification of a double layer charging model at the apex of an ILIS (Section 2.2.2).** A model for double layer charging within a pore, developed by de Levie [55], was invoked to describe the onset of electrochemistry at the apex of an ILIS. The results were corroborated experimentally, and provided the impetus

for the introduction of the distal electrode configuration and new emitter substrate materials.

2. **Introduction of the distal electrode configuration for ion electrospray to preserve the integrity of the emitter tips (Section 2.4).** A novel electrical connection configuration was introduced, motivated by the results of the double layer charging model. Methods for implementation and extended studies relating to implementation are offered.

   (a) **Extension of candidate ILIS substrate materials to include dielectrics (Section 2.3.1).** The new distal electrode technique permitted the transition away from difficult-to-manufacture porous metal substrates to dielectrics. Dielectric emitters are less prone to pure chemical degradation, and some formulations offer much better pore size and uniformity control versus metals which are usually sintered, resulting in limited pore sizes, especially considering ultra fine metal powder is very hard to work with and oftentimes explosive.

3. **Identification of discharges as the main life-limiting mechanism of ILIS (Section 3.1.5).** The welcome discovery that electrochemistry was not responsible for the sudden source failures and dark residue observed during many tests meant also that the cause was still unknown. More robust diagnostic tools introduced into ILIS tests demonstrated for the first time that sparking and arcing were occurring, and that dramatic source failures, dark residue, and in some cases total material ablation were attributable to these events.

   (a) **The first investigation into the causes and effects of electrical discharges on ILIS operating in vacuum (Section 3.3),** Discharges

in electrospray are hardly addressed qualitatively in literature, and, more often, are dismissed with the introduction of a scavenger gas that suppresses their occurrence which is not practical for vacuum applications. Various plausible causes of discharges are investigated here with first-order models for predicting discharges in practical applications of ILIS.

(b) **Identification of liquid expulsion and flooding as the leading cause of electrical discharges in ILIS in vacuum (Section 3.3.3).** An early hypothesis that implicated gas contamination as the leading cause of discharges led to an extensive experimental investigation. Results showed that gas contamination was just one factor in a broader cause: liquid flooding and expulsion from the porous substrate, which can occur even when gas is absent from the system.

(c) **Suggestions for operation and design of ILIS and iEPS to avoid electrical discharges (Section 3.4.4).** Generalized guidelines for operating conditions and design parameters were provided that derived from the preceding analyses and experimentation. Notably, filling in vacuum or soluble gas environments is recommended, and care should be taken to maintain adequate liquid containment within the porous substrate.

4. **Simplification of handling requirements in practical implementations (Section 3.4.4).** Compared to other electrospray devices, it was demonstrated here that even significant water absorption or filling in soluble gas environments should not be problematic given typical pore sizes of iEPS and ILIS discussed here. Noting that in industry, many devices may need to be prepared at once, significant simplifications may mean the difference between adoption or not.

Chapter 2

Electrochemistry in ILIS

One of the most critical challenges to achieving stable, long-life operation of ILIS is maintaining chemical neutrality to avoid decomposition of the liquid and corrosion of the electrode. At the electrode-liquid interface, an electrochemical double layer (EDL) exists in a state of equilibrium. As net current is applied to the electrode, the potential difference across the EDL changes, eventually exceeding the electrochemical window limit of the ionic liquid. At this point, electronic charge transfer across the interface occurs (Faradaic current) with potentially damaging electrochemical reactions.

In this chapter,

- the physics and history of electrochemistry are described,
- previous mitigation and modeling efforts are presented,
- the onset of electrochemistry in porous conductors is analytically determined and experimentally verified for the configurations of interest,
- alternative electrode configurations are suggested for both single emitter ionic

liquid ion sources and higher throughput implementations, and

- practical design considerations are discussed.

2.1 Theoretical background and previous work

2.1.1 History of the field

In nature, electrochemical reactions are more prevalent than purely chemical reactions: the conversion of biological energy into muscle power, collection and storage of solar energy in green plants, and breakdown of materials like metals are all examples of naturally-occurring electrochemistry [56]. Early electrochemical research began with the development of the Voltaic pile—the first battery—in 1800. Seminal works by Faraday [57] and Daniell [58] in the 19th century provide the foundation for the contemporary field.

Electrochemical systems are key enablers of renewable energy and other promising technologies. Porous electrodes promise even greater energy storage due to increased ion adsorption through nanopores compared to solid electrodes. De Levie [55] developed a model for electrochemical activation in porous electrodes in 1963 that laid the groundwork for Merlet's work [59] on their supercapacitance. Bai and Bazant [60] extended the analysis to account for already-activated areas within porous electrodes using a three-state Markov chain of untransformed, transforming, and transformed particles.

In electrospray, the electron-transfer reactions of electrochemistry were first observed by Blades [61] during tests of electrospray from zinc capillaries. Van Berkel [62] first described and exploited the current-controlled electrochemical cell behavior of electrospray to study the extent of redox reactions that occurred in a metal capillary

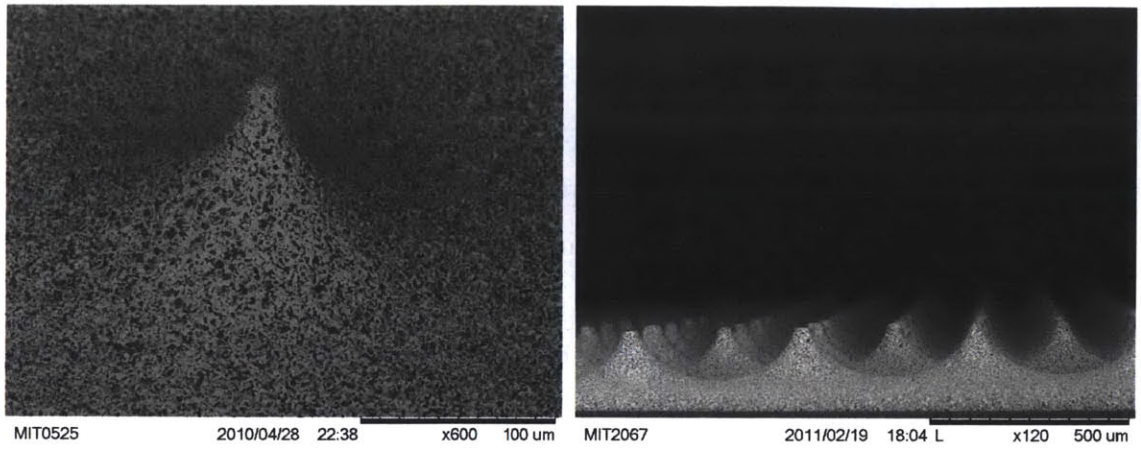

(a) A close-up of a single emitter (b) A cross-section of an array of emitter tips

Figure 2-1: A polymer-based photoresist was selectively applied to porous nickel and material from exposed areas was electrochemically removed to produce emitter tips from which ions are emitted [3].

using UV/visibile spectroscopy.

Electrical energy can be used to remove material for manufacturing in electrochemical etching—a fabrication technique that invokes electrochemistry to remove metal atoms from the anode to produce a desired surface finish or shape. This technique was used to manufacture emitter substrates in previous iterations of iEPS designs [3] (Figure 2-1). A similar process was used to fabricate many of the single emitters used for testing in this work (see Section 3.3.1 for a description of the etching procedure). If the target is the cathode, metals can be deposited to produce additively-manufactured features, as in electroplating and electroforming [63].

2.1.2 Basic notions of electrochemistry

Electrochemistry refers to chemical reactions between an electrolyte and electrode driven by an externally applied voltage. Charge carriers in conductive liquids in

contact with an object will form a layer of net charge over the surface of the object. Mobile charges within the object respond with an equal and opposite surface charge, and, together with the liquid charge layer, establish an electrical structure referred to as an electrochemical double layer (EDL) (Figure 2-2) [56]. Without any additional power input, some EDLs in this equilibrium state generate electric fields due to the separation of the two charge layers that are strong enough to induce electron transfer across the interface (10^9 V/m), causing the oxidation of the cathode and reduction of the anode as in the case of iron and water forming rust.

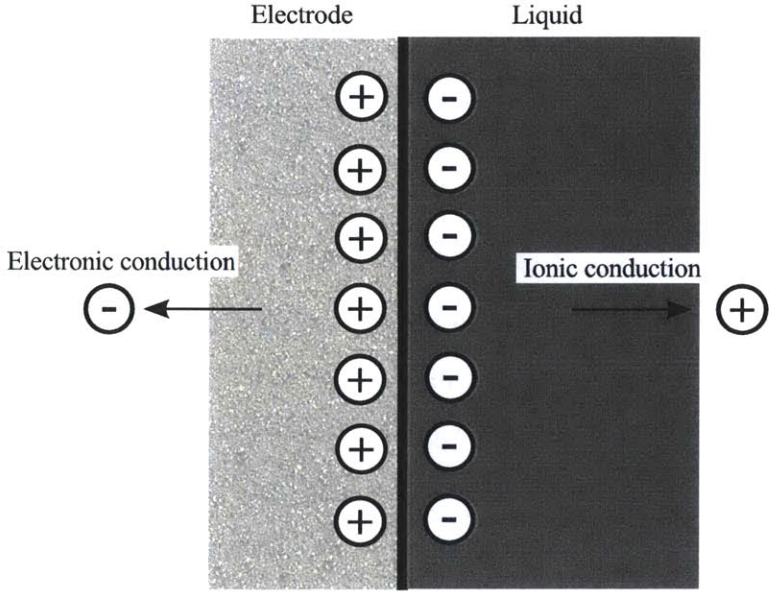

Figure 2-2: The formation of an EDL for ILIS operation in positive mode. Positive ions are drawn from the liquid while negative ions remain behind and form a layer of charge over the electrode surface. The electrode responds with an equal and opposite charge, and the two layers together form the EDL structure. As the layer charges, the field between the oppositely charged layers can become strong enough to induce electron transfer across the interface.

In instances where current is supplied to or drawn from the electrode, its (surface) charge level is further increased, prompting the counter-response in the liquid.

Consequently, the strength of the electric field in the EDL is enhanced, forcing redox reactions once the EDL is saturated to a critical level. This critical level is called the electrochemical window limit (window limit for short) and depends on the energy required to bring electrons out of their equilibrium states, or the work function of the materials. In literature, the window limit is given as the potential difference between the charge layers, V_w, that causes the electronic current between them to increase sharply. Potentials corresponding to the elbows in the current curves of Figure 2-3 indicate V_w for EMI-BF4 for water concentrations increasing in the direction of the arrow [4].

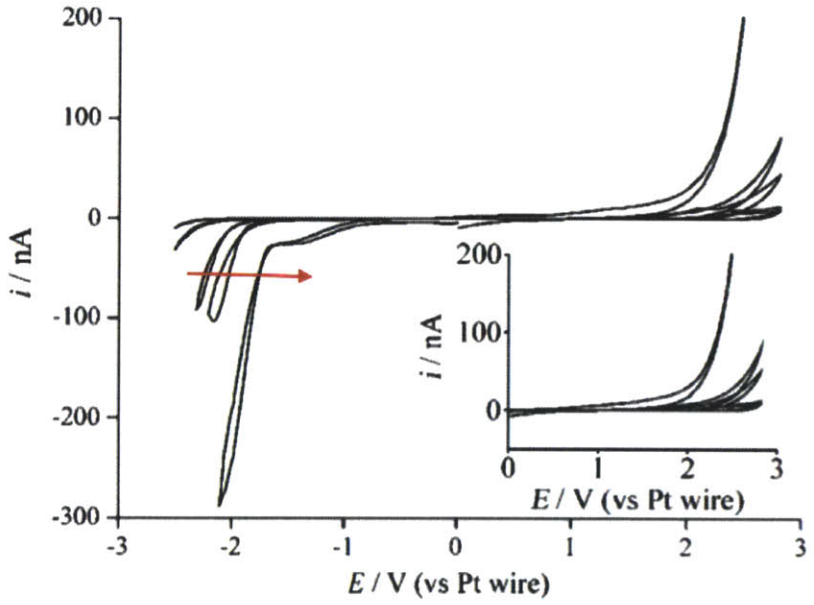

Figure 2-3: Voltammogram for EMI-BF4 for varying water concentrations. Water content increases in the direction of the red arrow, and in the opposite direction on the anodic side, indicating that the electrochemical window is reached at lower potentials for higher water content [4].

Depending on the application, electrochemistry is either avoided or encouraged.

Traditional electrolytic capacitors are examples of devices that are designed to operate below the window limit; redox reactions in these devices would likely short them, shorten their lifetimes, alter their capacitive properties, or otherwise skew their function. An even more ordinary example is coatings used to avoid rust on iron. On the other hand, many other processes and devices are designed to operate at the electrochemical window limit with reactions ongoing. Examples include batteries and fuel cells, and processes like electrochemical coating and blood glucose measurements.

2.1.3 Electrochemistry as a life-limiting mechanism of ILIS

Consequences for the lifetime of ILIS due to electrochemistry include diminished integrity of the emitter tips and ionic liquid, the production of gas that may be released between the electrodes, and the displacement of liquid from the device, all of which can lead to shorting and electrical discharges that may cause irreversible damage. Lozano and Martínez-Sánchez [33] operated a single tungsten emitter (254 μm diameter) wetted with BF4 under vacuum in positive DC polarity. Emission deteriorated noticeably over 3–4 h, and inspection of the emitter showed discoloration of the remaining liquid as well as a weak precipitate that formed over its surface (see Figure 2-4(a)). During tests of iEPS arrays, black deposits were observed and often coincided with device failure (see Figure 2-5).

Frequent recurrences of similar outcomes, together with the adverse effects of electrochemistry observed in [33], implicated electrochemistry as the primary life-limiting mechanism and prompted the analytic and empirical investigation into electrochemistry in ILIS presented in the remainder of this chapter.

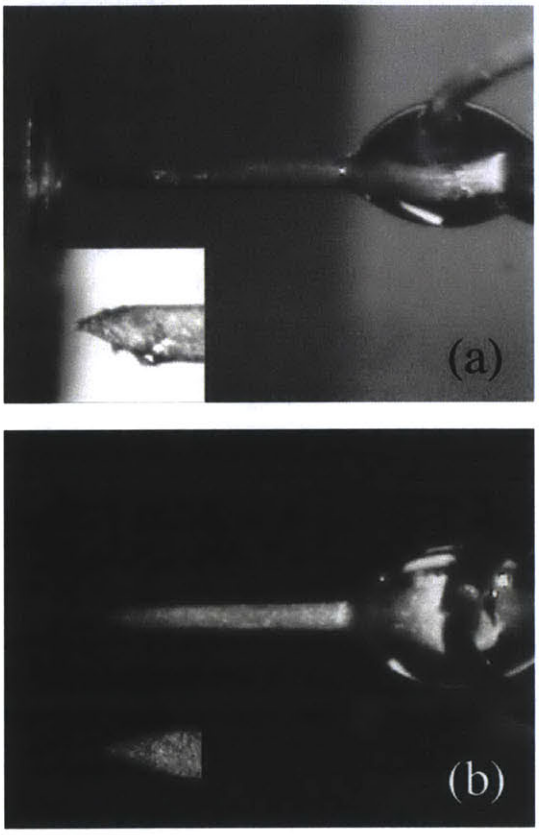

Figure 2-4: EMI-BF4 ionic liquid ion source working with: (a) positive DC polarity and (b) 1 Hz voltage alternation. The insets show the tip under greater magnification. Note precipitate and discoloration of liquid in (a), while the needle and liquid remain clear in (b).

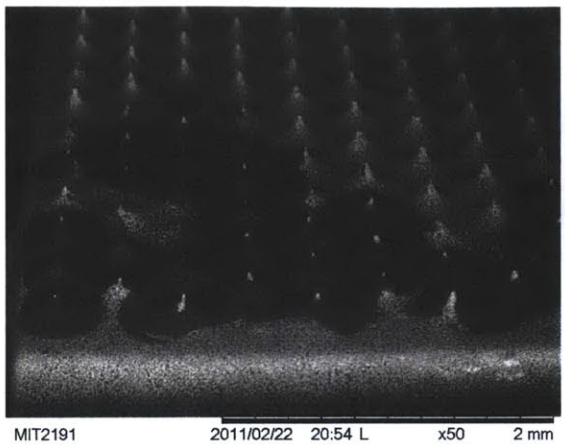

Figure 2-5: SEM image of an iEPS emitter array after firing. Black deposits were thought to be caused by electrochemistry and coincided with device failure in many instances.

2.2 The onset of electrochemistry in ILIS

As ions of one polarity are extracted from the liquid at the apex of an ILIS during emission, ions of the opposite polarity remain behind, forming an EDL at the electrode-liquid interface. As more current is drawn from the electrode, the potential difference across the EDL will eventually reach the electrochemical window limit of the liquid (since the electrode-liquid contact area is finite and its diffusion speed may not be as fast as the local EDL growth), resulting in its decomposition as well as corrosion of the emitter [33]. The electrochemical window limits of several ionic liquids are given in Table 2.1. Accurately predicting the onset of electrochemistry under particular conditions is essential to its prevention. As we will show, the time to onset is particularly sensitive to the source current and the active electrode surface area.

Table 2.1: Electrochemical window limits of several ionic liquids [15].

Ionic liquid	Window limit (V)
EMI-N(CN)2	3.3
EMI-2.3HF	3
EMI-BF4	4.5
EMI-C(CN)3	2.9
EMI-Im	4.1

2.2.1 In low-throughput cases

In a case with a large surface area-to-current ratio or fast EDL diffusion along the surface area versus local layer growth rate, the onset of electrochemistry can be estimated by idealizing the double layer as a parallel plate capacitor and calculating its charging time:

$$t(V = V_w) = \tau = \epsilon\epsilon_o \frac{V_w}{I} \frac{A}{\delta} \tag{2.1}$$

where τ is the time to saturation or the window limit, ϵ is the relative permittivity and ϵ_o that of vacuum; V_w is the electrochemical window limit; I is the source current; A is the active surface area, which is equal to the surface area for fast propagation in low-throughput cases; and δ is the molecular-sized EDL thickness. This approach implies that electrochemistry occurs simultaneously over the entire wetted surface area within a matter of seconds (11.2 s for EMI-BF4, 10.9 s for EMI-Im, and 8.4 s for EMI-F2.3HF according to Equation 2.1 with $I = 50$ nA, $A = 2.4\text{E}{-6}$ m^2), and has been used throughout literature to estimate charging times and as a basis for mitigation strategies.

One such method for preventing electrochemistry in ILIS applications—voltage alternation—was developed by Lozano and Martínez-Sánchez [33]. In this approach, the polarity of the power supply is alternated at a relatively low frequency (≈ 1 Hz).

With each cycle, a double layer forms and begins charging; before reaching saturation ($t < \tau$), the polarity of the power supply is inverted, discharging the previous double layer and forming one of opposite polarity (Figure 2-6).

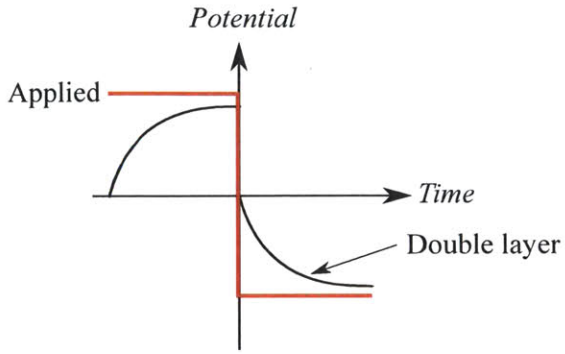

Figure 2-6: Applied and EDL potentials as a function of time using voltage alternation electrochemistry prevention method.

Single externally wetted ILIS emitters were used to investigate this approach. Compared to porous emitter arrays envisioned for implementation in high-throughput applications, single emitters are characterized by low emission currents and relatively large surface areas. A model for EDL formation suggested that its saturation time τ would be on the order of a few seconds, as it diffuses in a similar time scale to cover most of the emitter area. It was then anticipated that conveniently low polarity reversal frequencies would be sufficient to mitigate electrochemical effects. To demonstrate this point, an ILIS source wetted with the ionic liquid EMI-BF4 (1-ethyl-3-methylimidazolium tetrafluoroborate) was fired with the voltage source alternating at 1 Hz for about 220 h without signs of deterioration (Figure 2-4(b)) [33]. Operation proceeds essentially uninterrupted during the polarity reversals because both positive and negative ions are emitted at similar current levels.

Following this work, techniques for microfabricating arrays of conical emitters from porous nickel for space thrusters were developed [64] and similar tests were

conducted. Unlike the previous results with single emitters, microfabricated porous nickel emitter arrays experienced drastic current decay after firing for just minutes even when voltage alternation was used. In addition, scanning electron micrographs confirmed the presence of deposits clearly concentrated around the porous metal tips [65]. The cause was thought to be linked to electrochemistry that persisted in spite of voltage alternation as the EDL does not seem to be capable of diffusing fast enough into the porous bulk, aggravated by the much smaller emitter dimensions and currents up to an order of magnitude higher than in the single emitter case. The deterioration of the emitter electrode and contamination of the liquid pose a severe limitation to the lifetime of ILIS devices operating in the pure ionic regime [34, 66, 51]. Based on these results and the comparatively large currents emitted from highly localized sources in the array configuration, a more detailed investigation of double layer charging and alternative techniques for its prevention is required and undertaken in this thesis.

2.2.2 In porous media

For the analysis of EDL charge diffusion into porous or roughened materials such as those envisaged for micropropulsion applications, it is convenient to make use of the classical results by de Levie [55] in which the liquid-solid interface is modeled as a capacitor-resistor network representing a perfectly conducting pore of fixed diameter D along which the EDL diffuses (see Figure 2-7). The model is obviously oversimplified as it ignores the intricate geometry of emitter tips and their pore structure. Nevertheless, such analysis has proven to be adequate in capturing the temporal and spatial scales of interest in similar problems, like charging of ultra-capacitors [59].

According to de Levie's model, the EDL potential and current can be set as

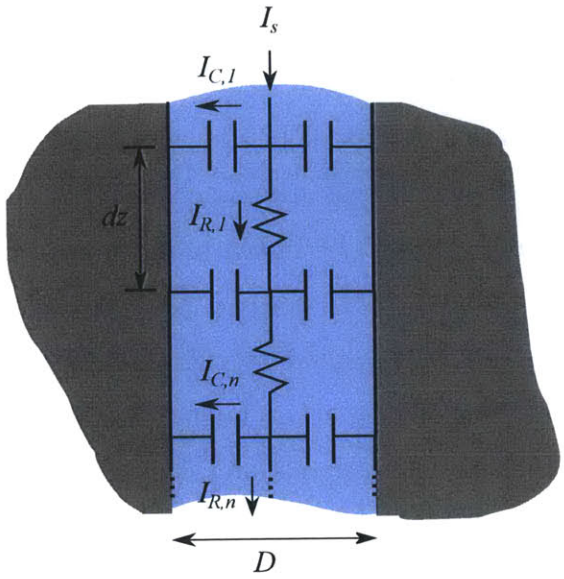

Figure 2-7: Capacitor-resistor network first implemented by de Levie.

regular diffusion-like equations:

$$\frac{\partial V}{\partial z} + IR' = 0 \tag{2.2}$$

$$\frac{\partial I}{\partial z} + C'\frac{dV}{dt} = 0 \tag{2.3}$$

with the solution

$$V(z,t) = I_o R' \left[-z \operatorname{erfc}\left(\sqrt{\frac{R'C'}{4t}} z^2\right) + \frac{e^{-\frac{R'C'}{4t} z^2}}{\sqrt{\frac{\pi R'C'}{4t}}} \right] \tag{2.4}$$

and

$$I(z,t) = I_o \operatorname{erfc}\left(\sqrt{\frac{R'C'}{4t}} z^2\right) \tag{2.5}$$

for $I(0,t) = I_o$ and $z(\infty,t) = 0$ where $R' = (K\pi D^2/4)^{-1}$ and $C' = \epsilon\epsilon_o \pi D/\delta$ are,

respectively, the liquid resistance and EDL capacitance per unit length of emitter material in contact with the liquid.

In here we are interested in estimating the potential evolution at the pore entrance. Assuming it lies in the closest proximity to the Taylor cone, this is tantamount to estimating the potential at the apex of an ion emitting micro-tip. In the context of this problem, D could be considered a characteristic dimension of the apex in contact with the ionic liquid. Since the ILIS behaves as a source of constant current I, we can approximate the situation as nearly-galvanostatic for which the tip potential becomes,

$$V_{tip}(t) = I_o R' \sqrt{\frac{4t}{\pi R' C'}} \tag{2.6}$$

The ionic liquid is characterized by an electrical conductivity K and dielectric constant ϵ. After normalizing (2.6) to the electrochemical window limit $u = V_{tip}/V_w$, we write, more conveniently, $u(t) = \sqrt{t/\tau}$, where

$$\tau = \frac{\pi^3 D^3 K \epsilon \epsilon_o V_w^2}{16 I^2 \delta} \tag{2.7}$$

The penetration depth of the EDL into the wettable porous or roughened material is given by,

$$z_{DL}(t) = \sqrt{\frac{KDt}{\epsilon \epsilon_o / \delta}} \tag{2.8}$$

It is then seen that, similar to the model presented in [33], the EDL diffuses one-dimensionally with a diffusivity given by $KD\delta/2\epsilon\epsilon_o$.

Presented in this manner, it is possible to make order of magnitude estimates about the EDL saturation time τ for a given set of dimensional and operational parameters when $u(\tau) = 1$. From (2.7), τ is very sensitive to D and I, so we can expect fast saturation times for small emitters producing relatively high currents.

For instance, taking $D \approx 1$ μm and $I \approx 2$ nA, and the properties of EMI-BF4 [40]: conductivity of $K = 1.3$ Si/m, specific capacitance $\epsilon\epsilon_o/\delta = 0.106$ F/m^2 and an electrochemical window limit of $V_w = 2.25$ V, we obtain $\tau \approx 5$ ms. More generally, τ versus z for several ILs is given in Figure 2-8. EDL saturation times along z

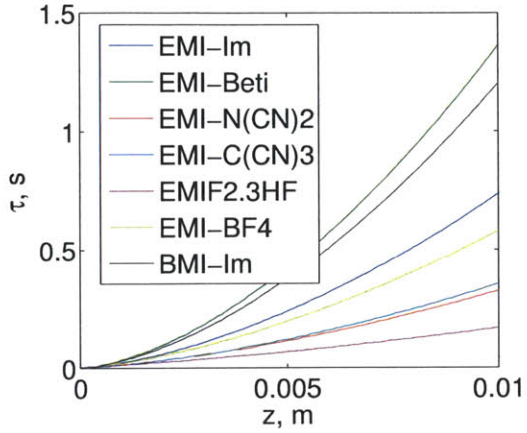

Figure 2-8: Saturation time τ along emitter length for candidate ILs using diffusion approximation.

of a porous emitter for EMI-BF4 is compared against the parallel plate capacitor approximation in Figure 2-9, illustrating the significant difference between the two methods.

These estimates reinforce the hypothesis that prompt electrochemical degradation in microfabricated porous metal arrays, as reported in [65], is very likely to occur as the alternation frequency in those experiments was always much lower than $1/\tau$. More importantly, these reactions will occur first at the apex of the emitter microtips and in adjacent regions as the EDL penetration depth increases into the material bulk. Eventually, for a given alternation frequency, reactions will be avoided at a distance given by (2.8). As the tips are very small in comparison with the substrate, most of the porous material volume would not experience noticeable degradation.

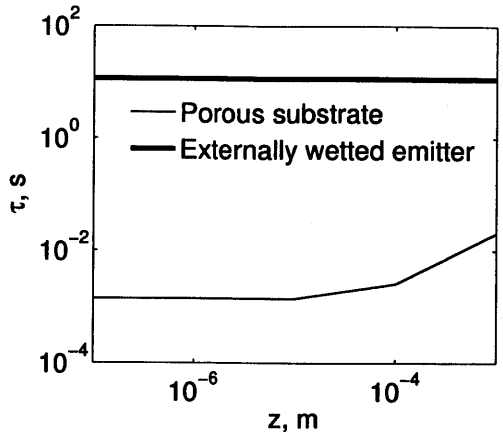

Figure 2-9: EDL charging time along z for EMI-BF4 for porous diffusion model compared to that predicted by the low-throughput capacitor model.

However, electrochemical effects will still be confined to the comparatively small volume of the tips, whose shape, pore structure and surface quality need to be preserved to avoid source failure. In principle, voltage alternation at higher frequencies (>1 kHz in the example above) would prevent the double layer from saturating at the emitter tips; however, those time scales have implications for electrical efficiency and possibly Taylor cone formation [67]. Because of this, alternative approaches to voltage alternation were considered.

2.3 Distal electrode configuration

2.3.1 Hypothesis

We postulate that an upstream *distal electrode* making electrical contact exclusively with the conductive liquid would mitigate electrochemical degradation of ILIS microtips under most conditions. Distal contact in traditional, droplet-emitting electro-

sprays is a practice adopted, for instance, in mass spectrometry as a flexible platform to perform a number of electrochemical experiments in which reactions are not avoided, but encouraged and studied in detail [62]. By moving the contact from the metal emitters to a distal electrode with a relatively large surface area, it should be possible to avoid electrochemical reactions from happening at ILIS micro-tips, both in single emitters and dense arrays.

Two such configurations are envisaged: one in which the emitters are fabricated from an insulating material and another that uses metallic emitters similar to those described before, but separated from the distal electrode by the liquid itself. In the former configuration, there would be no electrochemistry at the emitter surface as long as the electrochemical window is always lower than the equilibrium DL potential, which would not change as the local surface potential would simply follow the potential of the liquid (Figure 2-10a). However, in the latter case the electric potential of the metallic emitter substrate would be constant, while the potential difference across the DL would change as a result of the ohmic drop along the effective liquid path ℓ separating the distal electrode from the emission site near the micro-tips $\Delta V \approx I\ell/KA$ (Figure 2-10b). A is the effective cross sectional area through which the current I is transported. As long as $\Delta V << V_w$, electrochemical reactions will not occur at significant rates along the liquid path in contact with the metallic emitter substrate.

The DL over the distal electrode will still saturate, but only after a comparatively long time, and the distal electrode could be as large as practical. In both metallic and insulating substrate configurations, voltage alternation at modest frequencies would become again a reasonable technique for preventing electrochemistry at the distal electrode.

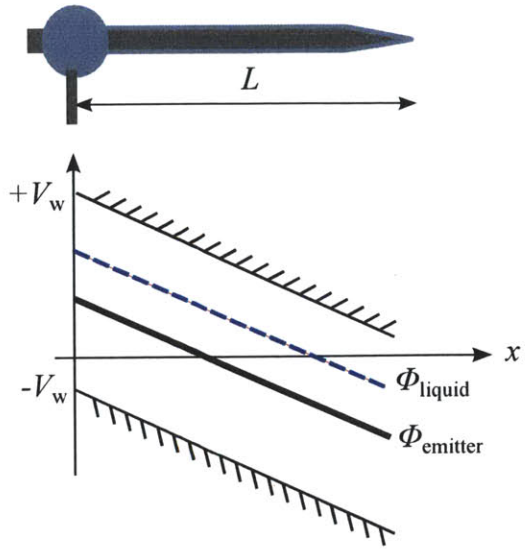

(a) Dielectric emitter

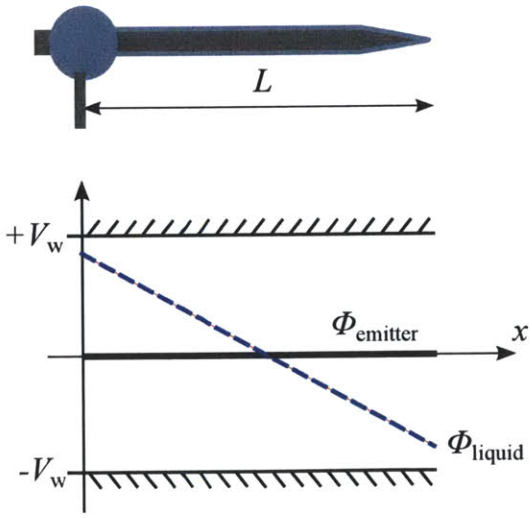

(b) Metallic emitter

Figure 2-10: Possible distal electrode configurations: in (a) the potential of the insulating emitter follows that of the liquid; the potential of the conductive emitter in (b) remains constant while the liquid undergoes an ohmic potential drop.

2.3.2 Experimental validation

Until now, every investigation in this field has been based on emitters made in metal or other conductive materials (like silicon), hence making it relevant to investigate the application of distal electrodes on such emitters. In order to achieve this, the ohmic potential drop ΔV is experimentally measured to confirm whether its value is as small as expected to avoid electrochemical reactions, and then two ILIS are tested simultaneously to compare the merit of the approach under the same operating conditions.

An externally wetted tungsten emitter 0.5 mm in diameter and sharpened to a radius of curvature of about 10 μm similar to that used in [66] is wetted with EMI-BF4 and passed through a stainless steel cylindrical reservoir serving as distal electrode, such that its contact area with the liquid is 18 mm^2. A square-wave voltage ($\pm$1285 V) is applied to the extractor at a frequency of 0.1 Hz. The emitter voltage with respect to ground is monitored using a high impedance ($>$ 200 TΩ) electrometer. The exposed emitter length, L, is varied *in-situ*. The effective liquid path is then $\ell \sim L$. The current to the cylinder (equal to the ion beam current) is monitored by a second electrometer and varied from 60–70 nA for $L \approx 2$ mm and 4 mm, respectively. Experiments are carried out in vacuum at pressures about 10^{-6} Torr.

The relative variation of the emitter voltage immediately after polarity reversal (at $t = 0$) is plotted in Figure 2-11 for these two exposed lengths. Eventually, the charging rates of the emitter in both cases become very similar and are consistent with ideal capacitive charging of the cylinder inner surface ($\sim$0.04 V/s). Removing the capacitive charging helps to estimate the ohmic potential drop along the liquid conductive path. The ratios of ohmic drop and exposed length are similar

(2mm/4mm $\approx$ 0.013V/0.024V $\approx$ 0.5), thus verifying the linear dependence on ℓ. More importantly, ohmic drop magnitudes ($\sim$ 0.01–0.025 V) are in agreement with anticipated values from operational conditions and liquid properties. Given the low value of the ohmic drop compared to the electrochemical window limit, it is unlikely that reactions will happen on the surface of the emitter.

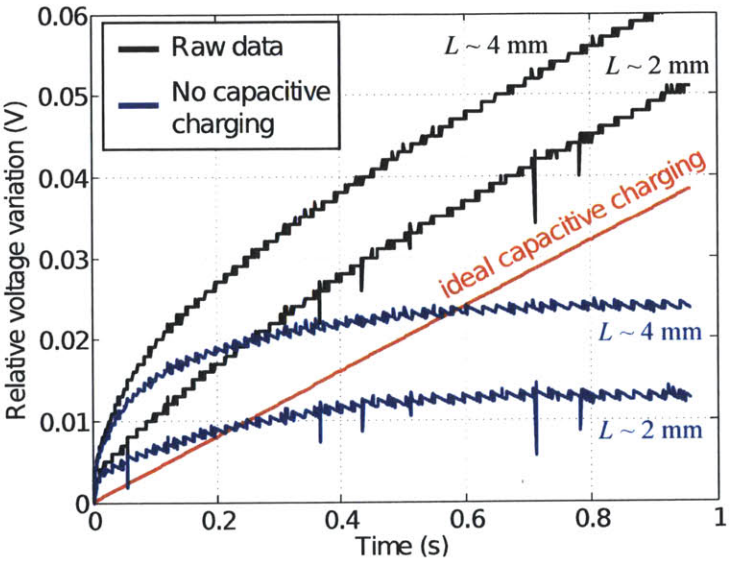

Figure 2-11: Monitoring the change in emitter potential. Ideal capacitive charging is removed to show ohmic drop at two different values of L.

To corroborate these findings, two tungsten emitters wetted with EMI-BF4 are fired simultaneously, one with a Pt(92%)-W(8%) wire in distal contact with the liquid and the other with the traditional direct contact to the emitter. Both emitters are operated in the positive DC mode for a total of 76 h, each with an average emitted current of 300 nA. The initial applied voltages are 1040 V and 1800 V for the direct and distal electrode contacts, respectively. This difference is mostly due to their distinct radii of curvature (the direct contact tip was sharper). The pressure in these experiments is below 5×10^{-7} Torr.

Current traces of both emitters over 16 h of the test are given in Figure 2-12. The direct contact emitter is significantly noisier and less stable, likely owing to the electrochemistry ongoing right at the emission site. The amount of liquid consumed

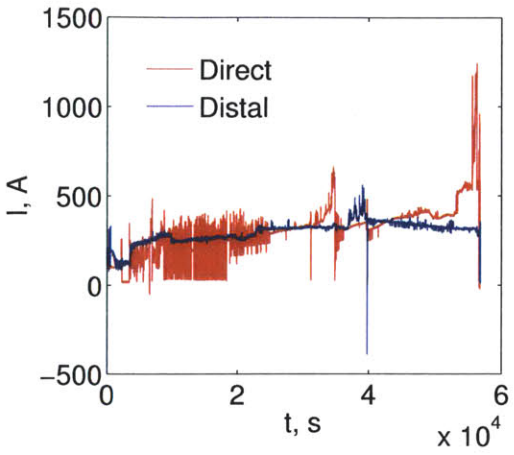

Figure 2-12: Current traces of both the direct and distally contacted emitters over 16 h of the 76 h test.

during this time by each source (~ 0.1 mm^3) is consistent with operation in the pure ionic regime. The emitters are visually inspected at the end of the experimental run. As expected, the remaining liquid of both emitters appears discolored from electrochemical reactions in which $BF4^{-1}$ ions are faradaically discharged to the contact electrode. Scanning electron microscope images of the emitters pre- and post-test are shown in Figure 2-13. In the distal contact configuration, the emitter appears intact after 76 h of operation, whereas the directly contacted emitter shows clear signs of degradation; in particular it is seen that tungsten at the apex was electrochemically etched away with noticeable material loss. Etching continued upstream as evidenced by a significant change in surface texture. The amount of material removed is found to be within a few percent of what would be expected through faradaic processes at

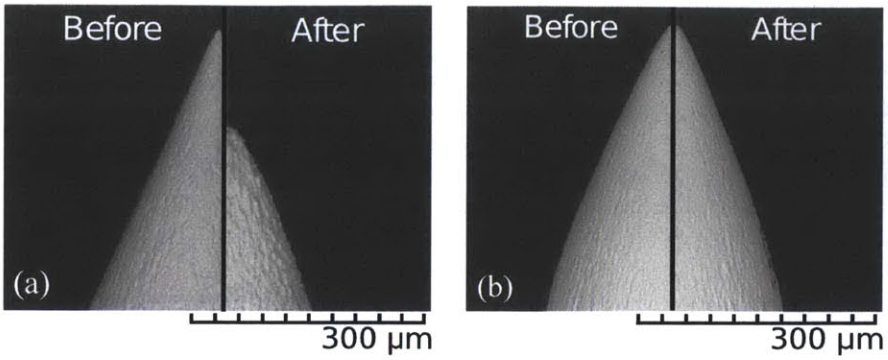

Figure 2-13: Tungsten emitters before and after firing. Tip etching and surface roughening is evident on the direct contact emitter (a); the distal contact emitter (b) appears undamaged.

the observed current levels by Faraday's law: $m = QM/Fz$, where m is the mass of substance liberated from the electrode, Q is the total charge, M is the molecular mass of the substance, F is Faraday's constant, and z is the valency number of ions. Hints of this process were evident during testing, as the voltage to the directly contacted emitter needed to be increased periodically as the tip became blunter. Correspondingly, the emitted current also increased with time. Lower tip curvatures in ILIS have been linked to higher currents by Castro and F. de la Mora [68].

2.4 Reduction to practice

Confirmation that the distal electrode configuration offers a viable electrical contact method while preserving the integrity of the emitter tips led to the development of distally-contacted configurations for both emitter array and single emitter sources (Figure 2-14). Furthermore, the combination of distal electrodes with roughened or porous ILIS emitters fabricated in electrically insulating and wettable materials is significantly advantageous over direct metallic contacts in practically all applications

of these ion sources.

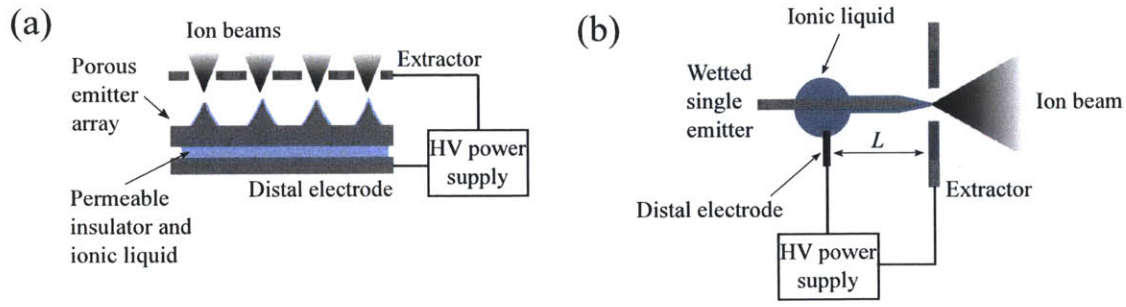

Figure 2-14: Proposed distal configurations: (a) porous metal array separated from the distal electrode with a permeable, electrically-insulating barrier, and (b) externally wetted single emitter with a liquid bridge to the distal electrode.

The latest version of iEPS under development at the SPL at the time of this writing includes a porous electrode that is distally-located within the propellant tank, separated from the dielectric emitter array by a layer of porous insulating material that wicks propellant between the tank and the emission sites as shown in Figure 2-15. Single emitters envisaged for FIB applications could implement a

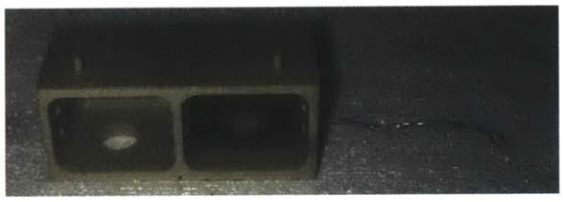

Figure 2-15: Two propellant tanks machined from a single piece of PEEK. In the right tank, the distal electrode is seen mounted near the port that connects to the thruster. The electrode's lead it seen protruding to the right.

cylindrical distal electrode reservoir that provides the electrical contact point, as in Figure 2-16. Ongoing work that concerns the implementation of the distal contact method for iEPS designs includes materials selection and fabrication, and attention to the implications of electrochemistry that will persist at the distal electrode for

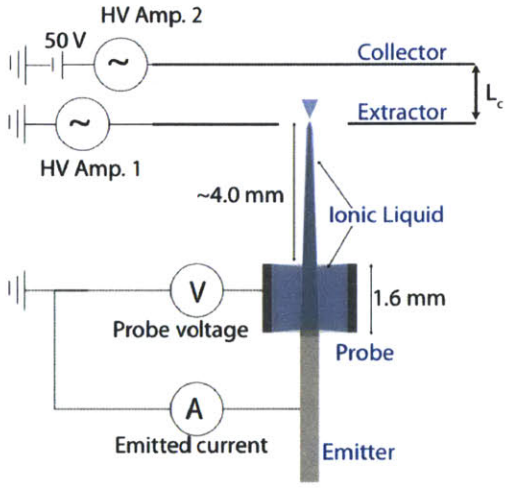

Figure 2-16: Illustration of implementation of distal electrode in single emitter applications. FIB emitters are commonly metal and compared to porous arrays of metal emitters are easy to manufacture. A cylindrical distal electrode filled with IL (that remains in place due to capillarity) surrounds the conductive emitter in this configuration, providing the electrical contact.

$t > \tau$ in cases where it is advantageous to alternate the polarity at a frequency below $1/\tau$.

2.4.1 Considerations for distal electrode design

During operation in one polarity, a double layer at the distal electrode will form and saturate in a manner that can be idealized as the capacitor described in Section 2.2.1, as current is drawn fairly evenly over the entire area compared to that drawn from the tip of an ILIS. Equation 2.1 clearly shows the inverse proportionality of the required alternation frequency $1/\tau$ to avoid electrochemistry with the surface area. Optimizing for design and operational simplicity, and possibly also power electronics efficiency, drives distal electrode material selection toward those materials with larger per-unit volume surface areas to minimize $1/\tau$. Figure 2-17 generalizes across liquids' specific capacitance and provides a guideline for the alternation frequency across a range of surface areas with $I = 200$ μA.

2.4.2 Gas evolution at distal electrode

Every electron that contributes to the current from the device while $t > \tau$ is transferred through electrochemistry, and in turn liberates material at the electrode during positive mode, or in negative mode which is of interest here, decomposes and evolves gas from the liquid. Gas evolution at the electrode can lead to liquid displacement from passive containment systems, electrical shorts, and higher-than-predicted pressures between the emitter and extractor electrodes that increase the likelihood of electrical discharges. Because polarity alternation may not be practical in all implementations of iEPS, it is worthwhile to investigate the consequences.

Faraday's law of electrolysis (for I constant in t) can be invoked to determine the

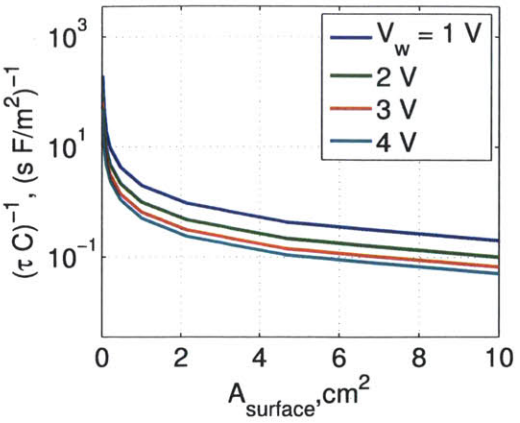

Figure 2-17: Guideline for selecting alternation frequency to avoid electrochemistry at the distal electrode across a range of surface areas. The alternation frequency is generalized across liquids by the specific capacitance, and different window limits are displayed.

rate of gas generation due to electrochemistry:

$$\dot{n}_{gas} = \frac{I}{Fz}\phi \tag{2.9}$$

where F is Faraday's constant, z is the valency number of ions, and ϕ is the fraction of moles of volatiles produced to total moles of decomposition products. Masuyama [69] provides the relative abundances of gas species evolved during electrochemistry for EMI-BF4 and EMI-Im. Taking the upper limit of gas evolution where every mole of electrons transferred corresponds to a mole of evolved gas ($\phi = 1$) gives $\dot{n}_{gas} =$ 2.07E$-$9 mol/s at $I = 200$ μA. The fate of the evolved gas depends on its solubility in the bulk IL, its propensity for ionization, and operational parameters such as ambient pressure and pore size. In reality, many of the products of decomposition during this process will not be volatiles but hydrocarbons. Nonetheless, it is interesting to examine this limit as it pertains both to liquid displacement and electrical discharges.

2.5 Conclusions and future work

This section described electrochemistry as a life-limiting mechanism of ILIS. Specifically, the de Levie model for double layer charging at a pore entrance was invoked to illustrate how rapidly the electrochemical window can be breached at the emitter apex, even if the double layer diffuses along the substrate at an appreciable rate. Methods other than kilohertz polarity alternation for preventing this albeit localized electrochemistry at the critical emitter apex were sought. The product of the exploration is a new electrical contact method that preserves the emitter integrity and mitigates the life-limiting effects of electrochemistry, and which has since been implemented in the latest generation of iEPS. Distal contact methods for ILIS permit prolonged operation as long as no other life-limiting mechanisms are at play, removing the need for source replacement in under 100 h which is important in any practical embodiment of the technique. Subsequent tests highlighted another persistent life-limiting mechanism in ILIS and iEPS, and the focus shifted to electrical discharges, described in Chapter 3.

Three extensions of the work discussed here are recommended. First, a more accurate representation of electrochemistry along a porous network could be developed by incorporating the three-state Markov chain introduced by Bai and Bazant [60]. It is not expected that the results for time to onset of electrochemistry, particularly at the emitter tip, will vary dramatically from this work, but the problem could be particularly interesting for applications like the bimodal system described by Masuyama [69] that employs the gas buildup from electrochemistry to produce thrust. Another area for exploration is a more in-depth study of electrochemistry at the distal electrode. Here, we assumed the charging more closely followed the parallel plate capacitor model versus the diffusion model; this assumption could be empiri-

cally tested to better align the model with actuality. Another recommendation is to study the effects of current asymmetry in residual reactions. These could produce gases or other products that might be relevant to the operation of thrusters. Lastly, distal electrode materials that are conductive, lightweight, have high surface-area-to-volume ratios, and are straightforward to manufacture will likely always be an interesting topic of study.

Chapter 3

Electrical Discharges in Porous ILIS

A second critical challenge to long-life operation of porous ILIS emitters is avoiding electrical discharges in the gap or through a liquid filament between the emitter and extractor electrodes during startup and normal operation. Non-negligible particle densities and strong electric fields between electrodes in either the gas or liquid phase can lead to conditions that support electrical discharges. Discharges are characterized by a sharp increase in current above a threshold voltage. They are typically preceded by electron avalanches—fronts of electrons generated by either impact ionization or field and secondary emission—that leave a conductive trail. If the advancing front reaches the downstream electrode, current can pass through the conductive column left by the avalanche, the magnitude of which depends on the power supply, among other factors. The precursory breakdown of fluid and the discharge itself reduce efficiency and can severely limit the lifetime of ILIS.

The discharge phenomenon manifests in ILIS under certain conditions relating to

geometry, background pressure, species present, the externally applied voltage, and ionic liquid contamination. In this chapter,

- the background of self-sustaining, steady-state discharges is reviewed,
- the conditions under which an applied voltage will induce breakdown in the inter-electrode gap of ILIS are analytically and experimentally explored, and
- design and operating conditions that promote long-life operation are qualitatively discussed.

3.1 Theoretical background and previous work

3.1.1 History of the field

In 1785, Charles Augustin de Coulomb observed that charge could leak through air, describing for the first time the non-self-sustaining discharge. Once batteries were capable of providing sufficient power by the early 19th century, the arc discharge was discovered and studied. Investigation into the physics of gas discharges, being inseparable from that of atomic physics, began in the late 19th century and subsequent concepts developed during the early 20th century by Townsend and Langmuir shape the contemporary field.

Electrical discharges in electrospray have been observed since the phenomenon was first studied. Zeleny [26] provides one of the first qualitative investigations of discharges associated with instabilities of the liquid jets of electrosprays, and Shmelev [70] investigated the propagation modes of such discharges along the jet. Yamashita and Fenn [71] observed noisier collected current signals and a discrepancy between emitted and collected currents at higher voltages compared to low voltages

that were discovered to be caused by a corona discharge that formed at the tip of the Taylor cone. The pair also observed that scavenger gases—those with strong electron affinities—could be introduced into the inter-electrode space to suppress discharges by increasing electron losses at a rate that exceeded electron production. Sulfur hexafluoride and carbon dioxide are now commonly used for this purpose [72, 26, 73].

In combustor applications that use electrospray to atomize the fuel, discharges are employed as a mean to igniting the fuel jet [74]. Discharges through liquid are widely studied as a method for water treatment [75, 76].

In spite of practical applications such as lasers and water treatment that have spurred contemporary research into discharges and plasmas, the bulk of the work on electrical discharges remains largely empirical and difficult to generalize across scenarios. While a body of work aimed at describing discharges in electrospray at high (atmospheric) pressures exists, at least qualitatively, the mechanisms by which discharges are formed *in vacuo* differ significantly in that the breakdown of air at atmospheric pressure between the electrodes is no longer the dominant process[1].

Furthermore, in applications of electrospray of the sort with which this thesis is concerned, such as colloid or ion propulsion which are operated in vacuum, the scavenger gas solution cannot be employed in a straightforward way and discharges must be understood and avoided through different techniques.

3.1.2 The physics of electrical discharges

Electrical breakdown is defined as the transformation of a nonconducting material into a conducting material as a result of the application of a sufficiently strong electric field [77]. Any flow of current through the resultant ionized media is referred

[1]In most vacuum breakdown scenarios, field and/or secondary emission from the cathode can provide a particle population sufficient for a discharge without a background atmosphere

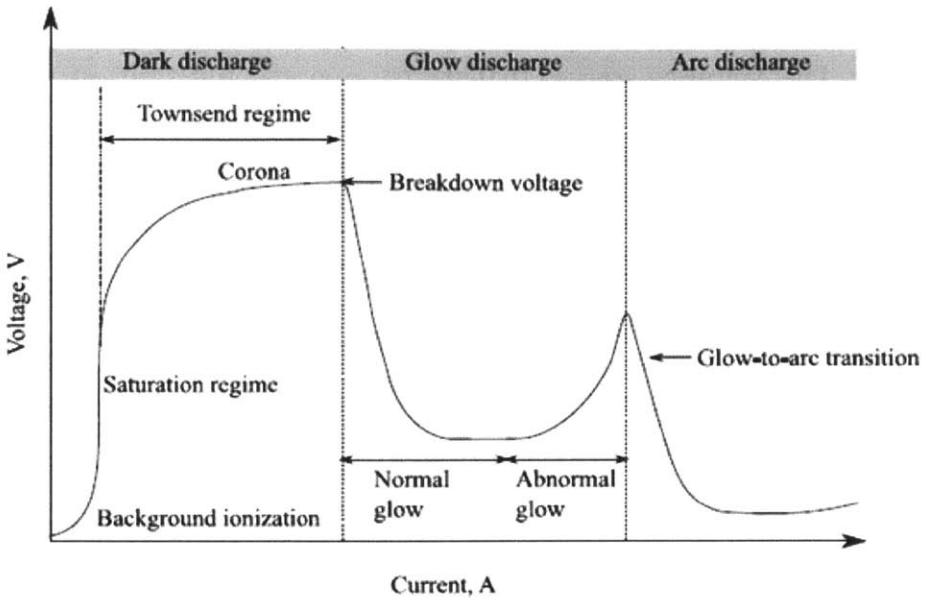

Figure 3-1: Discharge regimes. In practical embodiments of discharges, the realized regime is most often limited by the power supply [5].

to as a discharge, with the combination of the discharge current and applied voltage characterizing different types of discharges as shown in Figure 3-1. Commonly, the realized regime is determined by the maximum available current.

The primary element of breakdown is the electron avalanche (Figure 3-2). An initial electron, produced by cosmic rays, photoexcitation, or some other spurious mechanism is accelerated in the field between two electrodes. Upon gaining energy greater than the ionization potential of another particle in the region, the electron ionizes the particle and produces two electrons and an ion; under sufficient conditions, the process is repeated, and the region between the electrodes becomes macroscopically conductive. If the process persists even in the absence of any external source of electrons aside from the initial spurious population, the discharge is said to be self-sustaining. The situation can produce an arc discharge between the electrodes if

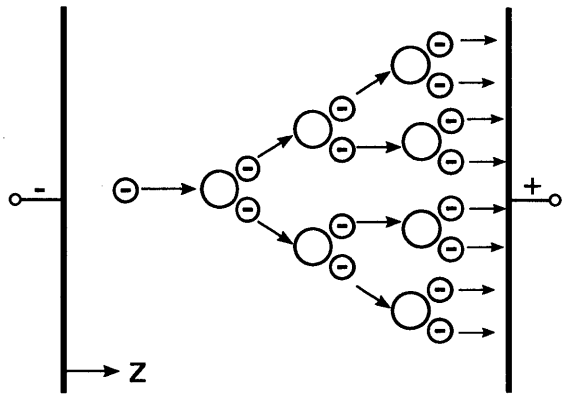

Figure 3-2: A schematic of an electron avalanche, showing an initial spurious electron leading to an eventual conductive pathway to the anode.

the current is not limited by the external circuit or the gap pressure and the cathode contributes to the electronic current via thermionic or field electron emission [78].

Streamers, weakly ionized thin channels formed from the primary avalanche that can lead to spark discharges, occur in gaps of greater separation than in Townsend discharges [79, 80]. The precursory avalanche becomes amplified along z, modifying the space charge to a level on the order of the externally-applied field [77].

In non-conductive liquids, discharges occur through vaporized gas pockets or along the liquid-gas interface [81, 82] and behave similar to dielectric barrier discharges where the liquid acts as a lossy dielectric electrode [83]. Channels of gas through or along which the discharge propagates can be produced by enthalpy changes from the discharge itself or can be otherwise injected.

Breakdown is a threshold process, meaning it only sets in if the field exceeds the value characterizing a specific set of conditions. The existence of a threshold is a consequence of the dependence of the rate of ionization on field strength, and by the fact that ionization is accompanied by mechanisms that create obstacles to the development of an avalanche [77].

Fluid breakdown and the subsequent discharge can be described by the Boltzmann collisional operator, which is a statistical model for describing particle interactions:

$$\frac{\partial f_s}{\partial t} + \vec{w} \cdot \nabla f_s + \frac{\vec{F}_s}{m_s} \cdot \nabla_w f_s = \sum_r \int_{w_1} \int_{\Omega} \left(f'_s f'_{r_1} - f_s f_{r_1} \right) g \sigma_{rs} d\Omega d^3 w_1 \tag{3.1}$$

that is constrained by the following limitations: only binary collisions are considered, molecular motions are assumed to be uncorrelated, and inelastic effects are neglected. f is the particle distribution function in the element of phase space volume $(\vec{x}, d^3x)$,$(\vec{w}, d^3w)$; w is the velocity; F are forces acting on the particle in external E and B fields; m is the particle mass and x its position; g is the relative velocity after the collision; and σ is the differential cross section.

Statements for conservation of mass, momentum, and energy can be obtained by multiplying the Boltzmann operator by a general function $\phi = \phi(\vec{x}, \vec{w}, t)$ and then integrating over all $\vec{w}$. A common simplification of the system is the steady-state drift-diffusion model for slow ions with the Einstein relation, governed by

$$\nabla \cdot \vec{\Gamma}_e = S_e \tag{3.2}$$

$$\nabla \cdot \vec{\Gamma}_i = S_i \tag{3.3}$$

$$\nabla \cdot (\epsilon \vec{E}) = e(n_i - n_e) \tag{3.4}$$

$$\vec{\Gamma}_e = -n_e \mu_e \vec{E} - D_e \nabla n_e \tag{3.5}$$

$$\vec{\Gamma}_i = n_i \mu_i \vec{E} - D_i \nabla n_i \tag{3.6}$$

where S_e and S_i represent sources of electrons and ions, respectively; μ_e and μ_i are the electron and ion mobilities; and D_e and D_i their diffusion coefficients [84, 77]. Further

simplifications to the system can be made to identify the breakdown threshold for given conditions, and in extreme simplifications an analytic solution is possible, as we will see.

3.1.3 Townsend discharge criterion for plane electrodes

Solving the full set of governing equations self-consistently to accurately predict discharges is numerically expensive and can still include some uncertainty due to the use of approximate empirical values for variables such as the collision cross-sections. J.S. Townsend developed an eponymous criterion that predicts steady-state discharges between plane electrode gaps with $PD < 200$ Torr·cm [85]. At these conditions, breakdown of the gap is achieved via successive electron avalanches (recall Figure 3-2) and when Townsend's criterion is met the discharge is said to be *self-sustaining*, meaning that the current can be maintained even without an external source of electrons. Beyond this point, the dark Townsend discharge can exist if the current of the circuit is limited, or otherwise the discharge may transition to a glow discharge. Townsend's is one of several theories that are able to predict, with adequate accuracy for many applications, the onset of self-sustained electrical discharges for certain conditions without invoking the full system of equations, and a summary follows here.

An electron that acquires enough energy will ionize αn particles per unit length, where α is the first Townsend ionization coefficient:

$$\alpha = \frac{\nu_i}{v_e} = \frac{1}{\mu_e} \frac{k_i\,(E/n_o)}{E/n_o} \tag{3.7}$$

μ_e is the electron mobility; v_e is the electron drift velocity; ν_i is the ionization frequency and k_i the ionization rate coefficient, which is a function of the reduced field,

E/n_o. Commonly, an empirical correlation for α is used that depends on the electric and pressure fields and, through the constants A and B, the ionization potential of the particles being considered [77]:

$$\alpha = APe^{-BP/E} \tag{3.8}$$

Values of A and B for several gases are given in Table 3.1.

Table 3.1: Empirical constants A and B in Townsend's first ionization coefficient for several gases [16, 17].

Gas	A $(\text{Torr}\cdot\text{cm})^{-1}$	B V/(Torr·cm)
Air	15	365
CO2	20	466
H2	5	130
N2	10	310
H2O	13	290
He	3	34
Ar	12	180

Steady-state electron continuity is

$$\frac{d}{dz}(n_e v_e) = n_e \nu_i \tag{3.9}$$

If $z = 0$ is the anode location and $z = D$ the cathode, electrons move with their drift velocity in $-\hat{k}$ so that substituting $\nu_i = \alpha v_e$ from Equation 3.7 gives

$$\frac{dn_e}{dz} = -\alpha n_e \tag{3.10}$$

for constant v_e. Integrating,

$$n_e(z) = \Psi e^{-\alpha z} \tag{3.11}$$

Ψ can be evaluated at $z = D$, giving the electron density in z:

$$n_e(z) = n_e(D)e^{\alpha(D-z)} \tag{3.12}$$

Similarly, steady-state continuity for ions is

$$\frac{d}{dz}(n_i v_i) = n_e \nu_i = -n_e v_e \alpha \tag{3.13}$$

Substituting n_e from Equation 3.12,

$$\frac{dn_i}{dz} = -\frac{v_e}{v_i}\alpha n_e(D)e^{\alpha(D-z)} \tag{3.14}$$

for constant v_i. Since $|v_e/v_i| \propto \mu_e/\mu_i$,

$$\frac{dn_i}{dz} = \frac{\mu_e}{\mu_i}\alpha n_e(D)e^{\alpha(D-z)} \tag{3.15}$$

which integrates to

$$n_i = X - \frac{\mu_e}{\mu_i}n_e(D)e^{\alpha(D-z)} \tag{3.16}$$

The ion density can be evaluated at $z = D$:

$$n_i(D) = X - \frac{\mu_e}{\mu_i}n_e(D) \tag{3.17}$$

and at $z = 0$

$$n_i(0) = X - \frac{\mu_e}{\mu_i}n_e(D)e^{\alpha D} \tag{3.18}$$

At the cathode, the electron flux is due to secondary electron emission from the cathode by ion bombardment:

$$n_e(D)v_e = -n_i(D)v_i\nu \tag{3.19}$$

where ν is the secondary emission coefficient which is the number of electrons emitted per incident ion and is a function of the cathode material, its surface properties, and the energy of the impinging ions. $n_i(D)$ from Equation 3.17 is substituted into the flux balance, giving

$$n_e(D) = \frac{\nu}{1+\nu}\frac{\mu_i}{\mu_e}X \tag{3.20}$$

Now we can obtain an expression for X in terms of $n_i(0)$ by substituting Equation 3.20 into Equation 3.18:

$$X = \frac{n_i(0)}{1 - e^{\alpha D\frac{\nu}{1+\nu}}} \tag{3.21}$$

Finally, substituting X into Equation 3.20 gives the following relations for $n_e(z)$ and $n_i(z)$:

$$n_e(z) = \frac{n_i(0)}{1 - e^{\alpha D\frac{\nu}{1+\nu}}}\frac{\mu_i}{\mu_e}\frac{\nu}{1+\nu}e^{\alpha(D-z)} \tag{3.22}$$

$$n_i(z) = \frac{n_i(0)}{1 - e^{\alpha D\frac{\nu}{1+\nu}}}\left[1 - e^{\alpha(D-z)}\frac{\nu}{1+\nu}\right] \tag{3.23}$$

Notice that $n_i(0)$ is still unknown. Regardless, it is possible to identify the conditions for a self-sustaining discharge as those which force the denominators of Equations 3.22 and 3.23 to zero, or, equivalently, $n_e(z)$ and $n_i(z)$ to grow unbounded, which is the Townsend discharge criterion:

$$\alpha D \geq \ln(1 + 1/\nu) \tag{3.24}$$

The Townsend criterion can be evaluated for particular uniform electric and pressure fields. By substituting Equation 3.8 and recognizing that for plane electrodes $E = V/D$, Equation 3.24 can be recast in terms of the breakdown voltage V_B:

$$V_B = \frac{B\,PD}{\ln\left[\frac{A}{\ln(1+1/\nu)}\right] + \ln PD} \tag{3.25}$$

Equation 3.25 gives the familiar Paschen curves shown in Figure 3-3, which can be read as the voltage at which a self-sustaining discharge occurs for a given value of PD. $\nu = 2$ is used which corresponds to secondary emission from stainless steel electrodes [86]. The minimum breakdown voltage occurs at

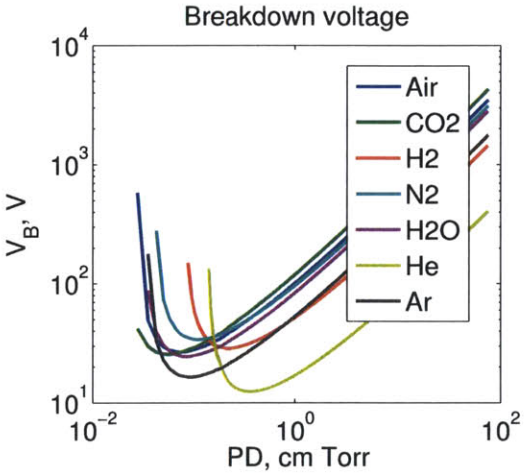

Figure 3-3: Paschen curves for several gases, indicating the voltage that will cause sparking in a plane electrode gap for a range of PD with $\nu = 2$.

$$PD_{V_{B,min}} = e^{1-k} \tag{3.26}$$

where

$$k = \ln\left[\frac{A}{\ln(1+1/\nu)}\right] \tag{3.27}$$

$V_{B,min}$ and $PD_{V_{B,min}}$ are given in Table 3.2. Immediately we see that for our nominal

Table 3.2: Minimum breakdown voltage and corresponding value of PD for several gases, corresponding to the troughs in Figure 3-3 for $\nu = 2$ and A given in Table 3.1.

Gas	$V_{B,min}$ V	$PD_{V_{B,min}}$ Torr·cm
Air	26.8	0.074
CO2	25.7	0.055
H2	28.7	0.220
N2	34.2	0.110
H2O	24.6	0.085
He	12.5	0.367
Ar	16.5	0.092

conditions ($P \approx 10^{-5}$ Torr, $D = 75$ μm, $\phi_o = 1200$ V), we would fall to the far left of the breakdown curves. Section 3.2 reformulates this criterion to more accurately represent ILIS conditions.

3.1.4 Transition to arc discharge

Beyond the Townsend discharge and the luminous glow discharge that are established by the avalanche mechanism above, the cathode can participate to a greater extent in the supply of electrons such that an arc discharge is supported. In this regime, the cathode can supply current densities up to 10^7 A/cm^2 via thermionic or field electron emission to an arc discharge with characteristic currents from $1 - 10^5$ A [77]. For stationary electrodes, initiation of an arc can occur by a transition from a glow discharge as the current is increased under constant pressure, or vice versa [78]. Arcs

can also be initiated by the transient sparks produced by streamers that form cathode spots which supply the necessary electrons.

Arc discharges can create plasmas at equilibrium with the surrounding gas, meaning the gas can reach temperatures up to 10,000 K. Their formation may be precluded by the resistance of the external circuit, or unsustainable particle populations; in these cases, the discharge may remain as a glow or sparks (transient arcs) may occur and quench the discharge. As complex structures that involve the cathode and the surrounding gas, arc discharges difficult to analyze but may be relevant given evidence of high-temperature processes presented in Section 3.1.5.

3.1.5 The identification of electrical discharges as a life-limiting mechanism of ILIS

Though we have in the preceding sections laid the groundwork for evaluating electrical discharges, prior to this work they had not been identified as a life-limiting mechanism in porous ILIS and iEPS particularly because of the low vacuum pressures maintained during tests and the low-to-moderate applied voltages. Solid black carbonaceous structures were observed on and around single porous emitters and emitter arrays after testing, and were asserted as consequences of electrochemistry or ablation (Figures 3-4, 3-5, 3-6).

Subsequent to the discovery of the distal electrode method for mitigating electrochemistry at the source apex in Section 2, the technique was implemented in an iEPS device in which electrical contact was made via a platinum wire in contact with a saturated porous dielectric barrier upstream of the emitter tips. Surprisingly, the problem persisted; the device failed within minutes and the familiar residue was observed. Recognizing that the polycondensation temperature of ILs is in the range

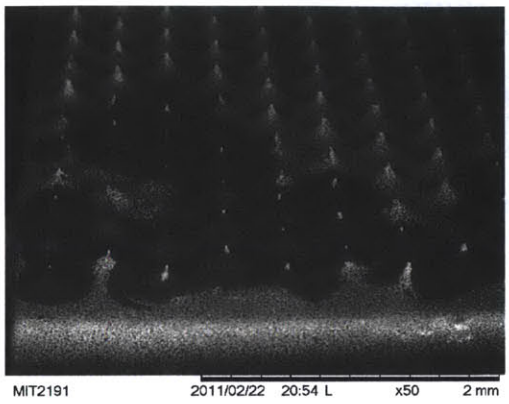

Figure 3-4: Porous nickel emitter array after firing, showing carbonized IL [3].

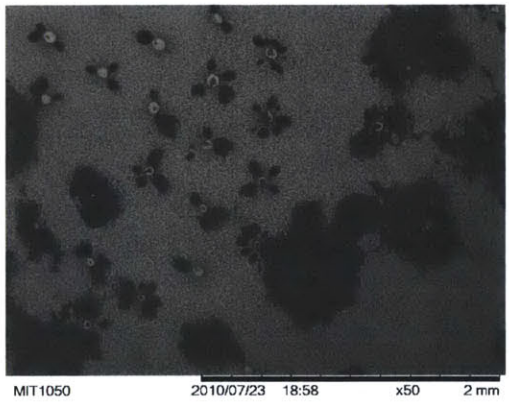

Figure 3-5: Top view of a porous nickel emitter array after firing, showing carbonized IL [3].

Figure 3-6: Close up of a porous nickel emitter after firing, showing carbonized IL [3].

of 400–500 K [6] implying that temperatures of this order were realized during testing, high-temperature phenomena such as electrical discharges were postulated as possible causes of degradation and failure. Carbonization, or more generally polycondensation, of ionic liquids has been employed by researchers for forming nitrogen doped porous carbon composite materials with tunable electrical conductivity or increased chemical stability [6, 87]. Figure 3-7 shows monolithic silica gels imbued with BMI-Im before heating and carbonization (A) and (B), and after (C). ILs with nitrile or other cross-linkable functional groups heated above their decomposition temperature will yield carbon structures, whereas those without such groups form volatiles [6]. Low vapor pressures and liquid states make ILs well-suited as precursors for this process, which can also be forced by the high temperatures associated with discharges.

A test was performed to evaluate the postulate that electrical discharges were responsible for source degradation and failure. A single porous nickel emitter was filled in atmospheric conditions with IL with roughly 20% water content by volume[2]

[2]Water content can be determined from the relative humidity, see Appendix C

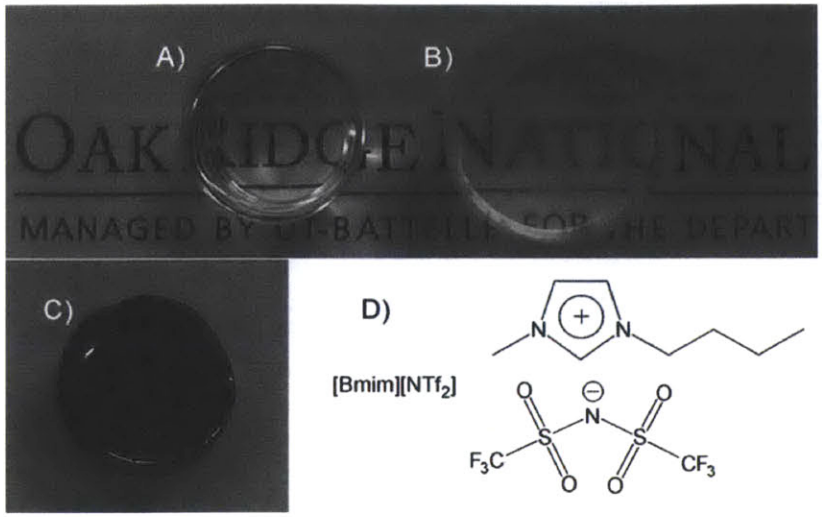

Figure 3-7: Silica gel monoliths imbued with BMI-Im: A) and B) are before the heating step; C) is after, showing a black carbon structure resulting from the decomposition and carbonization of the IL [6].

and fired for 1 h. During firing, a video camera connected to a microscope recording at 30 frames per second (fps) camera captured liquid bubbles forming on the surface of the emitter and spark discharges (Figures 3-8, 3-9). After the test, the emitter was cleaned in acetone and examined using a scanning electron microscope (SEM), which showed clear signs of discharges in the form of carbonized IL covering the tip (Figure 3-10).

The observed sparks and the post-test inspection confirmed that electrical discharges do occur during ILIS operation under certain conditions, and that their presence can have severe consequences for the lifetime of ILIS. Gas surrounding an arc discharge can reach temperatures on the order of 10^4 K [77], which can quickly heat the device and/or IL to well above allowable operating temperatures and cause source failure within seconds. Even if the material is intact after a discharge event, the carbon residue can obstruct the pores and stop the flow of IL to the emission

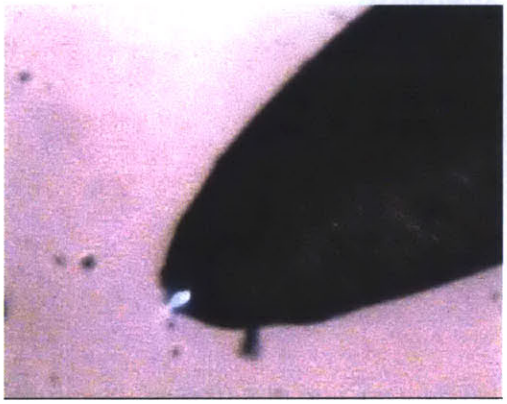

Figure 3-8: A spark discharge captured by a 30 fps camera during operation of a porous nickel emitter filled in atmosphere with IL with roughly 20% H2O.

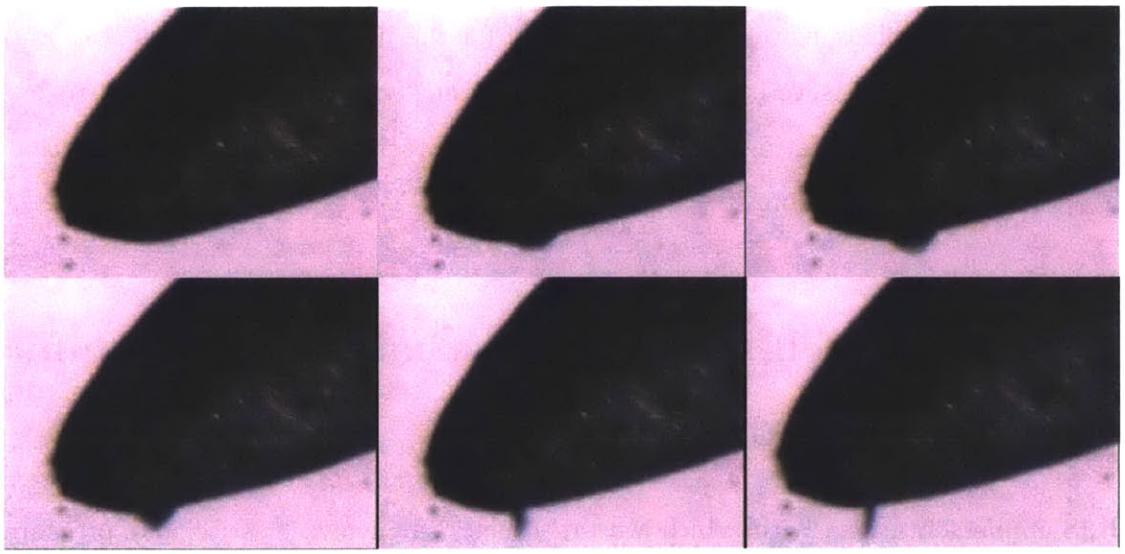

Figure 3-9: Frames selected from 3 s of video footage during test of emitter filled in atmosphere. The frames show a liquid instability caused by a bubble on the lower surface of the emitter; the bubble then bursts and carbonizes, forming a solid filament.

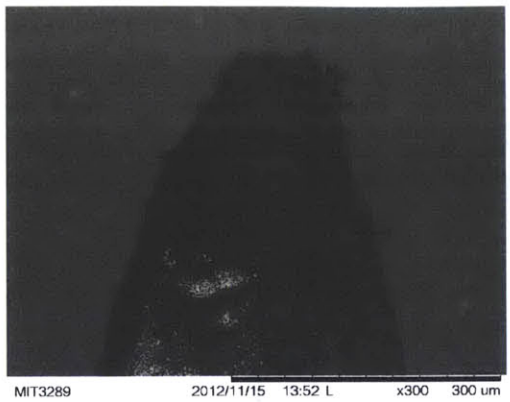

Figure 3-10: Porous nickel emitter filled in atmosphere after firing. Carbonization of the IL is evident as a result of discharges.

sites. Less dramatic discharges, such as a glow discharge, can draw μA of current, resulting in a significant loss of efficiency, as well as an increase in local temperature.

Electrical discharges were herein identified for the first time in porous ILIS and were shown to be a severe life-limiting mechanism, which motivated work to explore methods for predicting their onset and to qualitatively identify conditions that support long-life operation.

3.2 Steady self-sustaining discharges in non-uniform electric and pressure fields

ILIS implementations with which we are concerned involve electric and pressure fields that deviate from the plane-electrode, uniform-pressure conditions for which the conventional Townsend criterion was derived. It is useful to reformulate the criterion by modifying the first ionization coefficient, α, to determine if conditions specific to porous ILIS support self-sustaining discharges produced by this same

breakdown mechanism.

In these cases, a non-uniformity results from the emitter tip-to-extractor plane electrode geometry, producing an electric field strongest at the emitter tip and falling off away from the centerline and along z as we will show below. The pressure may also deviate locally from a uniform background pressure of roughly 10^{-5} Torr or lower due to the introduction of gases via several mechanisms such as contamination from the environment or gas evolution during electrochemistry.

Townsend's criterion is then

$$\int_0^D \alpha dz \geq \ln(1 + 1/\nu) \tag{3.28}$$

where the integral has been retained to account for the spatial dependence of E and P. Formulations for $E(\mathbf{r})$ and $P(\mathbf{r})$ specific to ILIS follow.

3.2.1 Non-uniform electric field

$E(\mathbf{r})$ lends itself to an analytical description by an orthogonal prolate spheroidal coordinate system [88], illustrated in Figure 3-11. In cylindrical coordinates, the hyperboloids are described by

$$\eta = \frac{1}{a}\left[\sqrt{R^2 + \left(z + \frac{a}{2}\right)^2} + \sqrt{R^2 + \left(z - \frac{a}{2}\right)^2}\right] \tag{3.29}$$

and the spheroids by

$$\zeta = \frac{1}{a}\left[\sqrt{R^2 + \left(z + \frac{a}{2}\right)^2} - \sqrt{R^2 + \left(z - \frac{a}{2}\right)^2}\right] \tag{3.30}$$

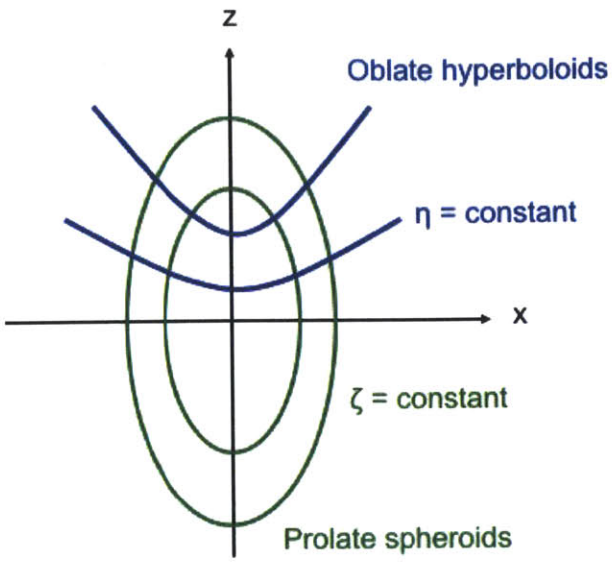

Figure 3-11: Prolate spheroidal coordinate system with prolate spheroids described by lines of constant ζ and oblate hyperboloids of constant η.

where

$$a = 2D\sqrt{1 + \frac{R_c}{D}} \tag{3.31}$$

If the potential is assumed to be constant (ϕ_o) on $\eta = \eta_o$ (the emitter tip) and 0 on $\eta = 0$ (the grounded extractor electrode) as in Figure 3-12, then each $\eta = b$ (with b = constant) confocal hyperboloid corresponds to an equipotential line and ϕ depends on η alone. From solving Laplace's equation,

$$\phi(\eta) = \phi_o \frac{\text{atanh}(\eta)}{\text{atanh}(\eta_o)} \tag{3.32}$$

where η_o is known from the radius of curvature and distance from the extractor to

the emitter tip (see Figure 3-12):

$$\eta_o = \left(1 + \frac{R_c}{D}\right)^{-1/2} \tag{3.33}$$

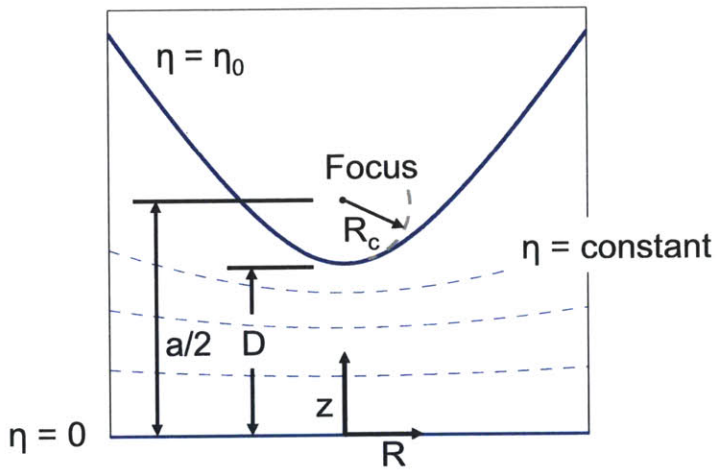

Figure 3-12: Prolate spheroidal coordinate system describing emitter and extractor geometry.

Since $\mathbf{E} = -\nabla\phi$, it follows from Equation (3.32) that

$$\mathbf{E} = -\frac{\partial\phi}{\partial\eta}\hat{\eta} = \frac{\phi_o}{\text{atanh}(\eta_o)}\frac{1}{1-\eta^2}\hat{\eta} \tag{3.34}$$

In cartesian coordinates,

$$\mathbf{E} = \frac{\phi_o}{\text{atanh}(\eta_o)}\frac{1}{1-\eta^2}\left(\frac{\partial\eta}{\partial x}\hat{i} + \frac{\partial\eta}{\partial y}\hat{j} + \frac{\partial\eta}{\partial z}\hat{k}\right) \tag{3.35}$$

where

$$\frac{\partial \eta}{\partial x} = \frac{x}{a}\left[\left(x^2+y^2+(z+a/2)^2\right)^{-1/2} + \left(x^2+y^2+(z-a/2)^2\right)^{-1/2}\right] \tag{3.36}$$

$$\frac{\partial \eta}{\partial y} = \frac{x}{a}\left[\left(x^2+y^2+(z+a/2)^2\right)^{-1/2} + \left(x^2+y^2+(z-a/2)^2\right)^{-1/2}\right] \tag{3.37}$$

$$\frac{\partial \eta}{\partial z} = \frac{1}{a}\left(\frac{z+\frac{a}{2}}{\sqrt{x^2+y^2+(z+\frac{a}{2})^2}} + \frac{z-\frac{a}{2}}{\sqrt{x^2+y^2+(z-\frac{a}{2})^2}}\right) \tag{3.38}$$

The norm of the electric field for ILIS represented by the prolate spheroidal geometry with $D = 75$ μm, $R_c = 15$ μm, $\phi_o = 1200$ V is shown in Figure 3-13.

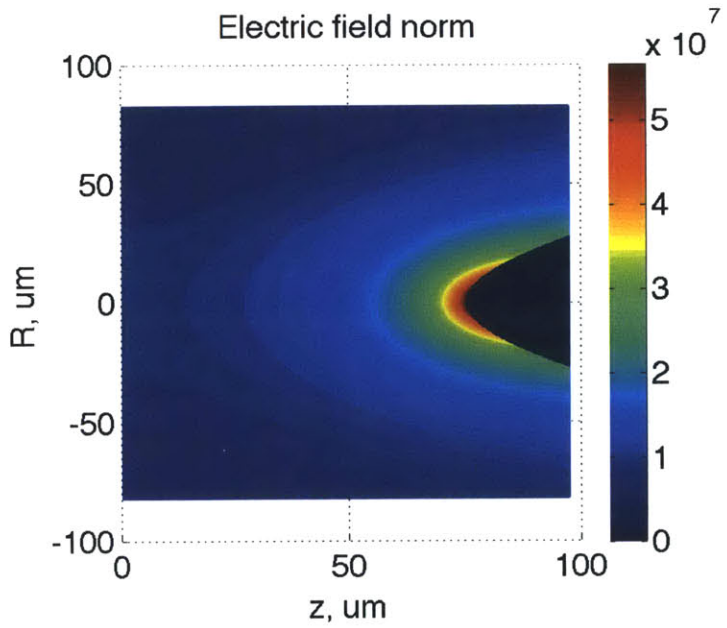

Figure 3-13: Electric field described by prolate spheroidal coordinate system for $D = 75$ μm, $R_c = 15$ μm, $\phi_o = 1200$ V.

3.2.2 Non-uniform pressure field

Non-uniformities in the pressure field $P(\mathbf{r})$ that should be included in α could arise from the steady evaporation of water vapor or other species from the ionic liquid, for example, or the bursting of an air—or insoluble but otherwise trapped gas—bubble. To first order, the former evaporation case is approximated by varying the magnitude of the uniform background pressure over a range of pressures, such that $P = P_{bg}$ which is uniform and constant; the latter is incorporated by superimposing a burst gas bubble [a spherical volume of comparatively higher-pressure gas whose volume is a function of time and whose center is located at $(0, 0, D)$] on the uniform background pressure, such that $P(t) = P_{bg} + P_{gas}(t)$.

At $t = 0$, the bubble has $P_{bubble,o}$ and $r_{bubble,o}$. Assuming the bubble bursts after vacuum has been reached, the gas will expand sonically so that the radius of the sphere grows as $r_{gas}(t) = r_{bubble,o} + \sqrt{\gamma RT}\, t$. $P_{gas}(t)$ can be determined from the initial conditions for an isentropic expansion where $P_{bubble,o}V_{bubble,o} = P_{gas}(t)V_{gas}(t)$:

$$P_{gas}(t) = P_{bubble,o}\frac{r_{bubble,o}^3}{\left(r_{bubble,o} + \sqrt{\gamma RT}\, t\right)^3} \tag{3.39}$$

Within the sphere, $P_{gas}(t)$ is assumed to be uniform.

Figure 3-14 illustrates $P(t)$ for $P_{bg} = 1\text{E}{-5}$, $P_{bubble,o} = 1$ atm, $r_{bubble,o} = 1$ μm, $\gamma = 1.4$, $R = 277$ J/kg K, $T = 300$ K. At $t = 1\text{E}{-9}$ s, the pressure is nearly 1 atm near the emitter tip ($z \approx D$) while everywhere else it remains at $P_{bg} = 1\text{E}{-5}$; by the time 1 μs has passed, the bubble has expanded past the extractor electrode, and the pressure within is nearly equal to the background pressure. Several values of P_{bg} and t will be assumed during the evaluation of the Townsend criterion.

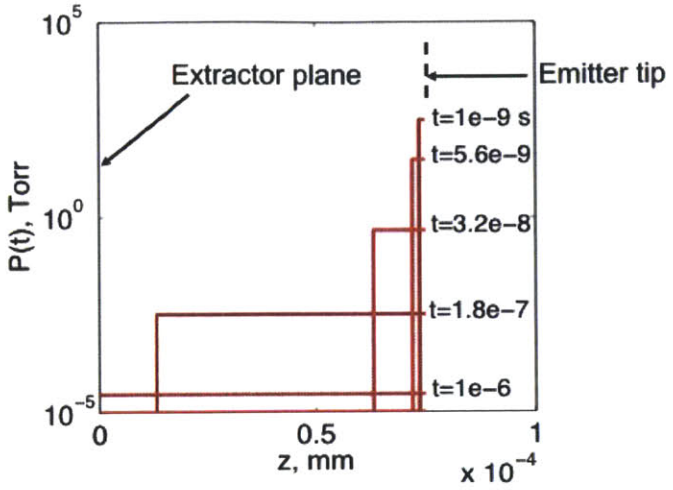

Figure 3-14: Plot of $P(t) = P_{bg} + P_{gas}(t)$ for $P_{bg} = 1\text{E}{-5}$ Torr at different values of t.

3.2.3 Analytical results and conclusions

Evaluating the Townsend criterion together with the non-uniform electric and pressure fields of the previous sections provides an analytic model for predicting self-sustaining discharges in ILIS, subject to specific conditions for which the criterion was developed. For completeness:

$$\int_0^{2a\eta_o} \frac{2}{a} A(P_{bg} + P_{gas}) e^{-B(P_{bg}+P_{gas})\left(\frac{2/a\phi_o}{\text{atanh}(\eta_o)} \frac{1}{1-\eta^2}\right)^{-1}} dz \geq \ln(1 + 1/\nu) \tag{3.40}$$

Figure 3-15 shows the results of the evaluation of the Townsend criterion for $D = 75$ μm, $R_c = 15$ μm, $\phi_o = 1200$ V, $\nu = 2$. The left hand side of the inequality in Equation 3.40 is plotted and compared with the Townsend criterion, the red dashed line. The integral was solved numerically using recursive adaptive Simpson

quadrature in MATLAB. Both non-uniform pressure field scenarios discussed in Sec-

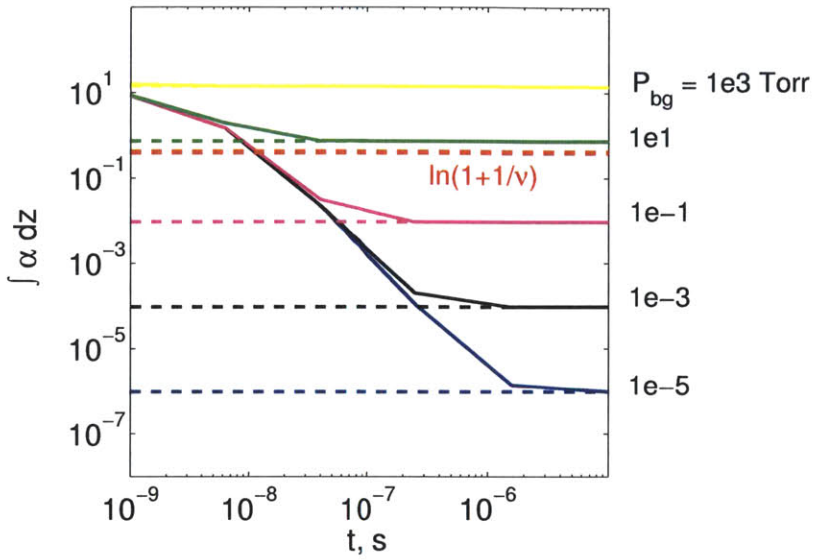

Figure 3-15: Townsend discharge criterion for $D = 75$ μm, $R_c = 15$ μm, $\phi_o = 1200$ V, $\nu = 2$ for a range of $P(t) = P_{bg} + P_{gas}(t)$. Conditions for a discharge are met at background pressures much higher than those maintained for testing (1 Torr versus 1E−5 to 1E−6 Torr), or immediately after an atmospheric-pressure bubble bursts.

tion 3.2.2 are represented in the figure: the dashed lines correspond to the criterion evaluated for constant P_{bg}, while the solid lines include, in addition to P_{bg}, a pressure contribution from a burst bubble as a function of time.

At face value, the results suggest that without a contribution from P_{gas}, background pressures on the order of 1 Torr or greater are required to support a self-sustaining discharge. For very small t ($< 10^{-9}$ s), an atmospheric-pressure bubble will induce a discharge for all P_{bg} considered. Shortly thereafter (after 1.4E−8 s for these conditions though this number should be regarded as a rough order of magnitude), discharges are not supported for P_{bg} below $\sim$ 1 Torr. At even longer times,

the discharge criterion tracks closely with the matching P_{bg} case without a bubble.

These results combined with observed discharges prompted the large experimental study in Section 3.3. However, beyond a general direction for subsequent studies, definitive conclusions we can draw from this analysis are limited because the criterion was developed for a specific breakdown mechanism under prescribed conditions. In other words, negative results would not imply discharges are impossible via other mechanisms. Similarly, false positives may be generated by neglecting transient effects, for instance. As one example, the inference that immediately after the atmospheric-pressure bubble bursts conditions are such (right at the emitter tip and assuming the external circuit does not limit the current) that a self-sustaining discharge can be produced is complicated by two factors not captured in the analysis. First, $P(t)$ decreases below the value necessary to support a discharge quickly—in fact on the same timescale as the formation of discharges themselves ($\sim 10^{-9}$ s [77]) but this effect is neglected in the steady-state analysis. And second, we showed in Figure 3-9 that a discharge took place away from the tip where the field is weaker. One interpretation not captured here for the scenario where the field is too weak to engender the straightforward Townsend mechanism is ohmic heating through a liquid filament that forces its decomposition which in turn increases the local gas pressure to a level that supports an arc. Along the same vein, a filament could create a strong electric field at the fine tip, leading to a glow discharge that transitioned to an arc.

Though the Townsend criterion can provide accurate results for predicting the onset of discharges in many applications, the situation in porous ILIS involves complex interactions between thermal, fluid, and plasma processes that are not captured in this analysis. Certainly more detailed models could be developed and the author encourages that undertaking to aid in the mitigation of discharges, but for now, motivated by this first-order analytical result and the results of the test of the emit-

ter filled with IL in an atmosphere, we experimentally examine the relationship of trapped gas to electrical discharges.

3.2.4 Relation between trapped gas and electrical discharges

Given the analytical results of Figure 3-15 which suggest that atmospheric-pressure gas released in the strong electric field can instantiate a self-sustaining electrical discharge, a test was performed to validate the result by positing that the absence of trapped gas should preclude such events.

Another porous nickel emitter similar to that described in Section 3.1.5 was fabricated, cleaned, and filled with ionic liquid *in vacuo*, according to the procedure outlined in Section 3.3.1. The emitter operated for nearly an hour with the same microscope recording setup at roughly 2 kV and between $2 - 10$ μA. Emission from the emitter proceeded smoothly, with no gas bubbles or discharges. After testing, the emitter was cleaned in acetone and examined using an SEM. The surface was unchanged [Figure 3-16; the difference in color between the before and after of b) is due to a change in the SEM 'brightness' setting], pointing to the conclusion that the formation of electrical discharges in porous emitters can be precluded by filling in vacuum, which ensures the absence of trapped gas from filling.

This result together with those of Section 3.1.5 demonstrates that, in spite of the nominal low pressures maintained during testing and operation of porous emitters, discharges can indeed play an important role in premature source failure under certain conditions. Furthermore, porous ILIS filling conditions that were previously regarded as trivial are shown to be highly consequential to the lifetime of the devices. Note that we have not eliminated water vapor or other sources of gas contamination as precursors, as their presence would have been precluded by the vacuum filling

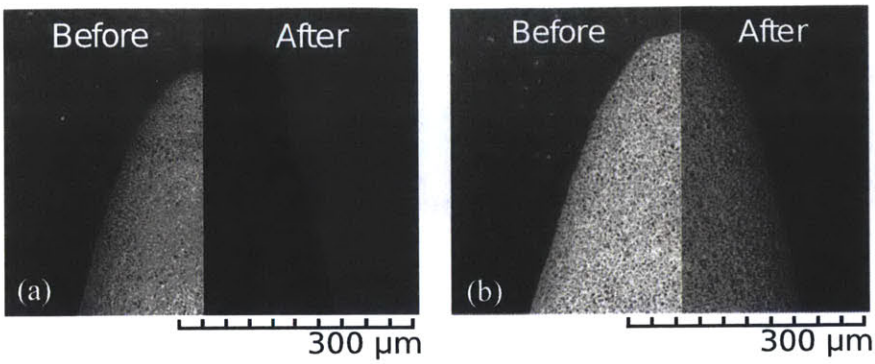

Figure 3-16: Before and after images of the emitter filled in atmospheric conditions (a) whose test was described in Section 3.1.5, compared to the emitter filled in vacuum (b). The difference in color between the before and after of (b) is due to a microscope setting.

process as well.

3.3 Experimental investigation of discharges in ILIS and iEPS

In Section 3.2, we showed how certain instances of premature source failure could be attributed to electrical discharges, provided an analytical method for predicting discharges under certain conditions, and empirically verified at least one precursor to electrical discharges in porous ILIS emitters: gas contamination. Thus far, our hypothesis is as follows:

> Electrical discharges that present in porous ILIS are due to the release of gas and/or the subsequent expulsion of liquid that result from the filling of porous substrates in gaseous atmospheres or the evaporation of water vapor or other contaminants from the environment.

In order to prevent electrical discharges and promote long-life operation of porous ILIS, a more detailed understanding is necessary. Through the following experimental investigation, we seek to test our hypothesis and answer the following questions:

1. How does the filling gas affect the likelihood of electrical discharges?
2. Given the dual polarity operation modes where the anode and cathode are exchanged, does one configuration support discharges more than the other?
3. Do emitter materials influence the occurrence of discharges, whether by secondary emission properties, hydraulic effects, or so on?

3.3.1 Experimental configuration

A series of tests using porous single emitters operated in vacuum and monitored by a suite of diagnostic instruments is performed to identify the primary causes of discharges. The tests performed, equipment and instrumentation used, and methods for emitter fabrication follow.

Test matrix

Several tests are prescribed that force some conditions while inhibiting others to eliminate incorrect hypotheses and to highlight the primary contributors to discharges. Test variables, the reasoning for their variance throughout tests, and values the variables could assume are given in the following list and Figure 3-17.

Filling condition Emitters filled in vacuum are assumed to be free of residual gas and water vapor contamination from the environment. Those filled in a gas atmosphere at 1 atm (the type of which is also varied) contain residual gas and oftentimes significant amounts of water.

Filling gas Gas species vary in their solubility in IL and their ionization potentials, cross-sections, electron affinities, and other properties. Gas species are varied for emitters that are filled in gas atmospheres.

Emitter polarity Alternating the anode and cathode provides insight into the effects of charged particle dynamics and material properties such as secondary emission coefficients on the presence of discharges.

Emitter material The material is varied during tests, though largely out of necessity due to manufacturability. Different materials are characterized by different pore sizes, wettability, conductivities, and secondary emission coefficients.

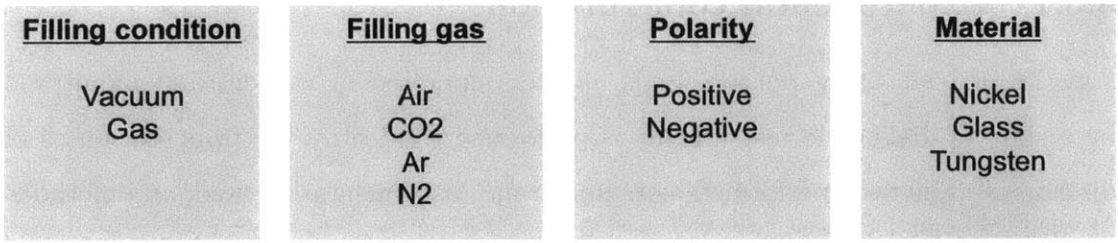

Figure 3-17: Single emitter test variables and their possible values.

Vacuum chamber setup

Experiments are performed in a vacuum chamber held at roughly 5×10^{-6} Torr. A single emitter is held in a copper mount that can be positioned in x-y-z using a Newport MT-XYZ linear optomechanics stage. The extractor is connected to a stationary mount relative to which the emitter can be moved. A rotational drive is mounted to the side of the vacuum chamber and facilitates vacuum filling of emitters. The stage and mount assembly are secured to the front flange of the vacuum chamber via a custom aluminum plate. Figure 3-18 shows the mounting setup.

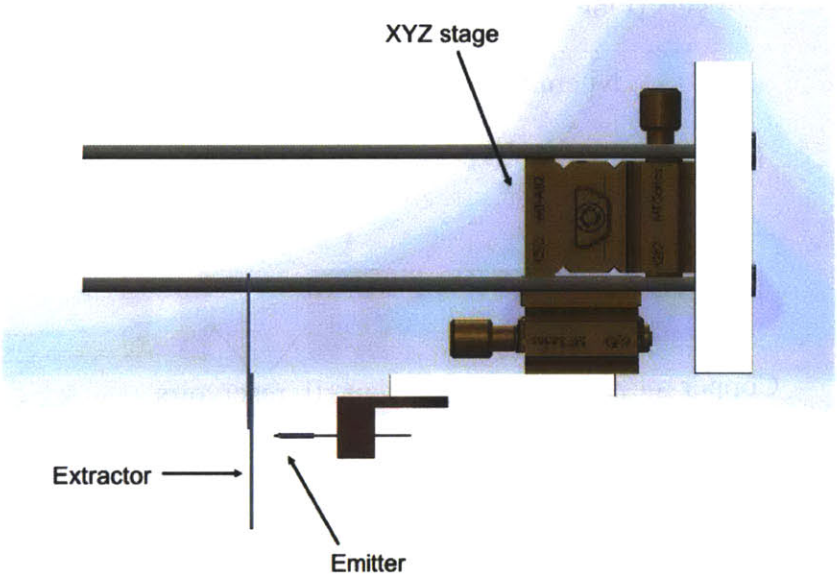

Figure 3-18: Illustration of emitter mounting setup used to position emitter relative to extractor and provide electrical contact. The entire assembly is mounted to the door flange of the vacuum chamber.

The copper mount was originally designed for the nickel emitters welded to a stiff tungsten wire (Figure 3-19a). Tungsten and glass emitters were also used for some tests. Tungsten emitters are planar and brittle, and required a mounting configuration in which the emitters themselves were secured in the mount, and in some tests a reservoir was used (Figure 3-19b). Glass emitters are non-conductive and required a saturated dielectric layer (that also acts as a reservoir) that is in contact with the mount (Figure 3-19c).

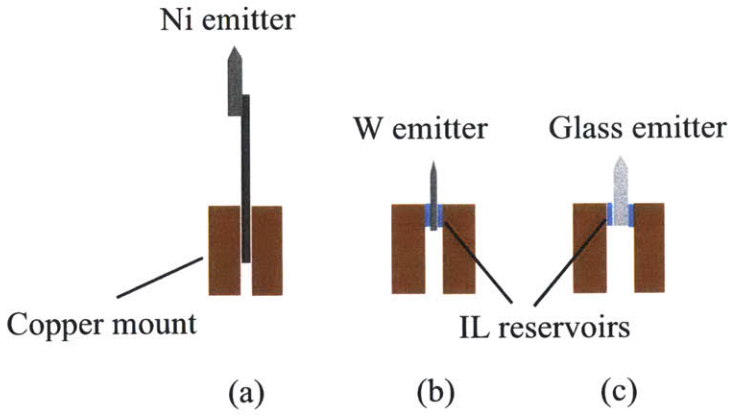

Figure 3-19: Different mounting techniques used for (a) nickel, (b) tungsten, and (c) glass emitters that inadvertently introduced an additional variable.

Power is supplied to the setup through a Matsusada AMS-5B6 high voltage amplifier, triggered by an Agilent 33220 A signal generator. Current, voltage, and discharge frequency signals are amplified if necessary and acquired by a National Instruments data acquisition module (NI USB-6229 BNC). Post-processing is done in MATLAB. A residual gas analyzer (RGA) is used to monitor partial pressures of gas species and is connected to the chamber via a CF flange. A high-speed camera is attached to a microscope and is positioned flush with a six-inch viewport on the chamber with the end of the lens 4.5 inches from the emitter. The electrical and

data acquisition connections are illustrated in Figure 3-20.

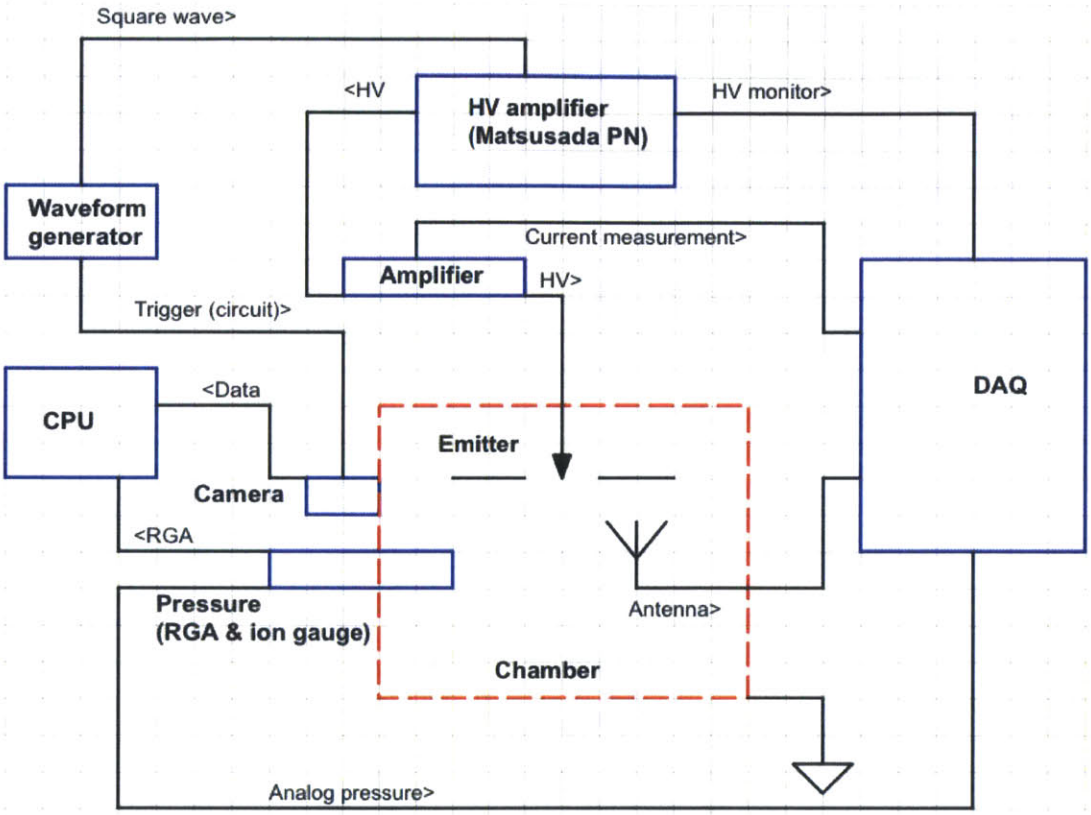

Figure 3-20: Data and electrical connections during tests. Signals directly monitored by the DAQ include: discharge frequency from the antenna, chamber pressure, emitted current (after amplification), and high voltage. Other data/commands are the waveform generator that triggered the HV amplifier and high-speed camera, and the camera and RGA data that were directly collected by a separate computer.

Diagnostic instruments

The following diagnostics and measurement techniques are used.

Residual gas analysis The partial pressures of gases in the vacuum chamber are measured and recorded using an Extorr XT200(M) residual gas analyzer (RGA).

Charge-to-mass ratios of gas particles present in the chamber and ionized by the RGA's ionizing filament are measured by a quadrupole mass spectrometer to produce the spectra output indicating relative amounts of species present. A superimposed RF-DC hyperbolic electric field is produced such that only ions with the particular q/m being scanned are passed through the quadrupole and collected at the Faraday cup detector. Acceptable operating pressures for the device are monitored by a Pirani gauge and a dual thoria-coated iridium filament hot cathode ion gauge.

RGA data can be sampled in two modes:

- In trend mode, masses of interest are sampled five times per scan, with each sampling occurring at the set dwell time and the average being reported. The total run time per trend is then $N_{scans} \times 5 \times t_{dwell} \times N_{masses}$. A typical configuration in these tests was $N_{scans} = 5000, t_{dwell} = 10$ ms, $N_{masses} = 9$, giving a run time of 37.5 min and a sample rate of 20 samples/s. The program used in these tests observed 9 masses: H_2, N_2, H_2O, O_2, Ar, N, OH, O, and CO_2.
- In sweep mode, the number of samples per amu is set as $N_{samples,amu}$, and the number of scans per second as $N_{samples,s}$. The typical program used for these tests was across 0–200 amu, with $N_{samples,amu} = 10$ and $N_{samples,s} = 10$, giving a total run time of 200 s per scan.

Examples of output from both modes are shown in Figure 3-21 for the empty chamber after 23 hours of pumping. RGA outputs during firing can indicate patterns between discharges and variations in gas amount and species.

Electromagnetic pulse detection An antenna is mounted near the emitter that

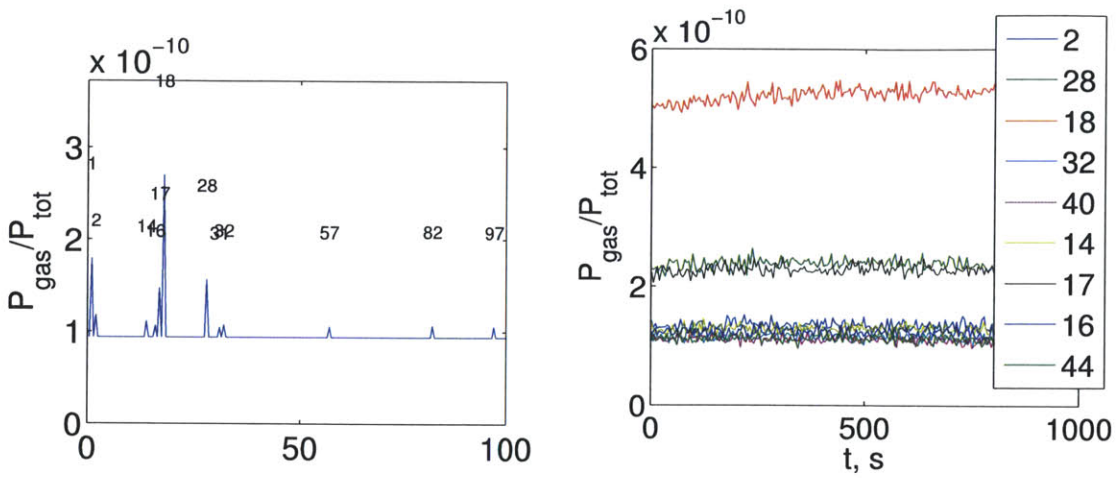

(a) Sweep mode

(b) Trend mode

Figure 3-21: Example sweep (a) and trend (b) mode RGA data. Scans were performed after the chamber had been under vacuum for 23 hours and was free of any setups or experiments.

records instances of discharges. This measurement serves two purposes. First, it provides a method for corroborating anomalies in the rest of the data with the occurrence of a discharge. Second, it provides information about the frequency of discharges under different conditions, such as the extractor distance. The detector circuit is shown in Figure A-1.

Emitted current and applied voltage Emitted current and applied voltage measurements provide an indication of the health of the emitter. Single emitter current levels on the order of μA's require amplification using the circuit in Figure A-2. The Matsusada amplifier provides a monitor channel that is connected to the DAQ for voltage measurements.

Visual inspection of the emitter A Bonito CL-400B/C high speed CCD camera, DALSA xcelera x4 full frame grabber card, and Scienscope ISO 9001 micro-

scope enable correlation between macroscopic phenomena such as bubble bursts and discharges. The camera is triggered using the signal generator that also controls the high voltage amplifier and an Arduino Uno board at ~100 fps, limited by the amount of available light. Image processing is done in MATLAB. Post-test SEM imaging is performed to determine the state of the emitter after firing.

Chamber pressure gauge The total pressure in the chamber is measured using an InstruTech, Inc. Hornet Hot Cathode Ionization Vacuum Gauge IGM401 Module with a log-linear analog output, $P = 10^{V-10}$, where V is the output voltage read by the DAQ and P is in Torr.

Emitter fabrication

Single emitters, which offer a flexible platform for tasks like manipulation within the vacuum chamber to allow filling in vacuum and variation of the extractor distance *in situ*, were used to study the effects of various filling conditions on the occurrence of discharges. Most emitters used in the following tests were fabricated from porous nickel using a procedure modified from Courtney for porous nickel emitter arrays [3]. Bulk sheets of porous nickel were diced into pieces 1 mm × 1 mm × 1 cm and cleaned following this solvent cycle:

- 20 min acetone
- 20 min deionized water
- 20 min methanol
- 20 min deionized water
- 20 min isopropyl alcohol
- 2 h drying in argon

Each piece was individually connected to a power supply and lowered into the center of a stainless steel cylinder that functioned as the cathode; the cylindrical configuration helped to ensure even current draw around the nickel area. Both the cylinder and the nickel in its lowered position were submerged in a 2N HCl electrolyte solution (Figure 3-22). First, the nickel was lowered so that 3 mm was submerged and the power supply was turned on to 7 VDC, 3 A for 30 s. Next, the nickel was raised slightly so that only the last 1 mm was submerged, and the power supply was turned on to the same parameters for 20 s. The last step was to slowly pull the emitter from the solution with the power supply on, having a final sharpening effect on the tip to achieve $\sim$50 μm radius of curvature. Oftentimes adjustments had to be made

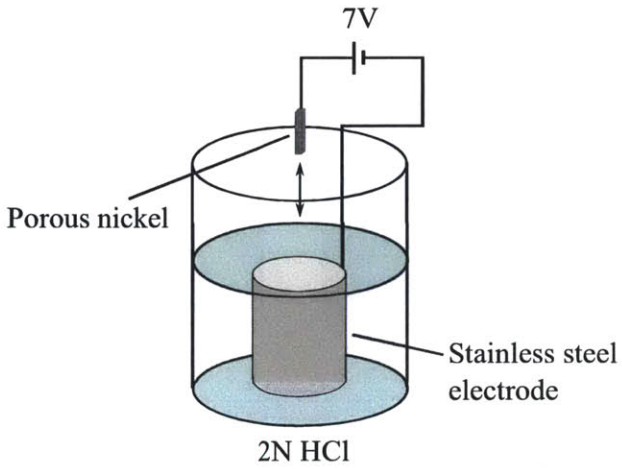

Figure 3-22: Electrochemical etching setup for fabricating emitters from porous nickel. 7 VDC was applied and roughly 3 A was drawn from the power supply; the electrolyte was 2M HCl.

to the above procedure, as it was found to be particularly sensitive to the ambient humidity and the concentration of HCl. A sample of the fabricated emitters are shown in Figure 3-23.

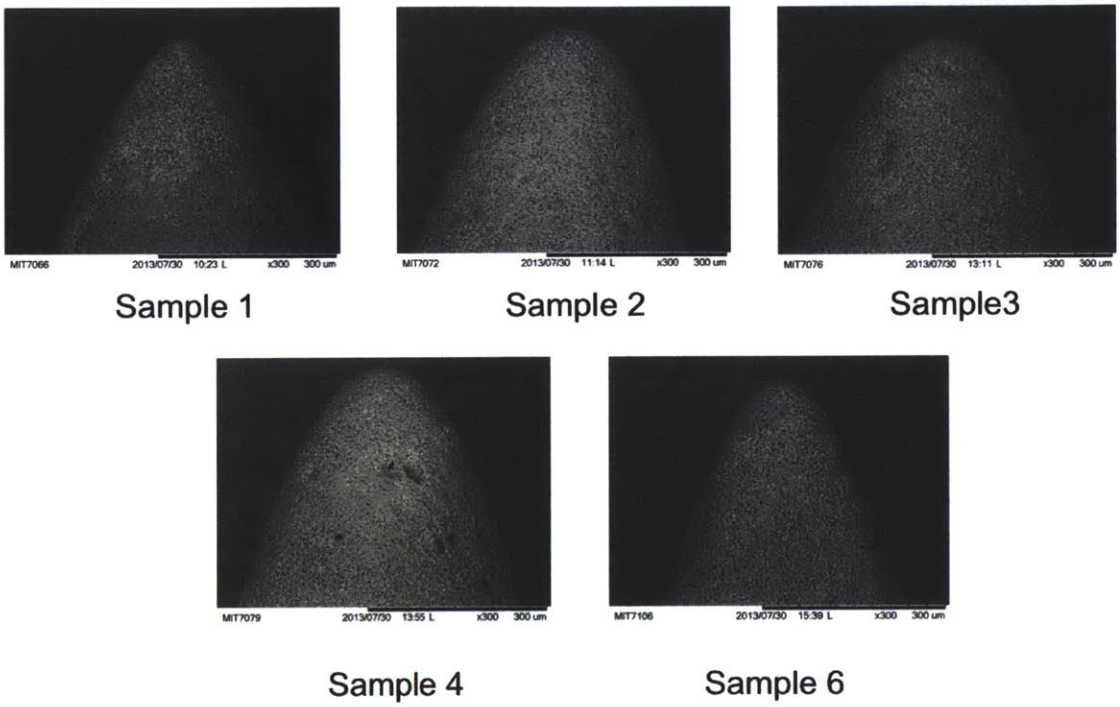

Figure 3-23: Six samples of porous nickel emitters that were electrochemically etched in 2M HCl at 7 VDC for 60 s.

Other emitter materials of interest are tungsten and glass. Single tungsten emitters were fabricated using the method developed by Legge [18]; representative SEM images of tungsten emitters used in tests are shown in Figure 3-24. Lastly, single borosilicate emitters were used in some tests. Bulk borosilicate frits were obtained and filed into emitters similar in shape to the nickel emitters (see Figure 3-25).

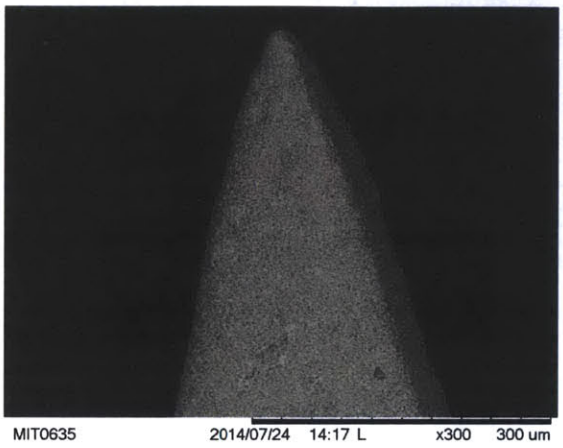

Figure 3-24: An example of a tungsten emitter used in tests.

3.3.2 Test procedure

Tests proceed as follows:

1. Ionic liquid filling. Filling with ionic liquid occurs immediately prior to testing to minimize the potential for contamination from the environment. Emitters to be filled in vacuum are mounted in a rotational arm on the side of the vacuum chamber above an open container of ionic liquid. Care is taken to avoid high-surface roughness materials and container geometries that promote copious IL loss during outgassing due to splashing. After the pressure in the vacuum chamber reaches roughly 1×10^{-5} Torr, the top ~ 1 mm of the emitter

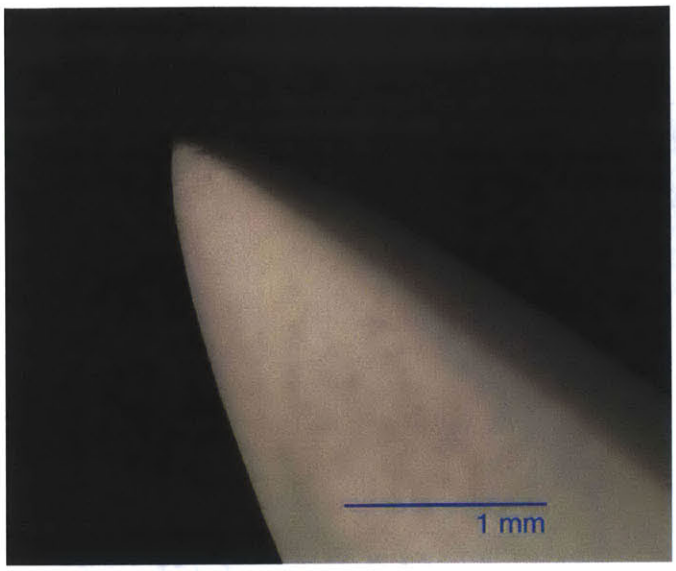

Figure 3-25: Example glass emitter used in tests with $R_c = 47.5 \pm 15.5$ μm.

is rotated into the IL and held for 20–30 minutes. The chamber is vented and the emitter is removed from the rotational arm.

Emitters to be filled in gas atmospheres are placed in a vacuum glove bag that is purged and then filled with the filling gas at 1 atm. A pipette is used to place approximately 0.007 mL of IL on the side on each emitter. The volume of liquid was calculated as 80% of the open volume of the emitter to prevent over-saturation. After 20–30 minutes, the emitter is removed from the filling gas environment.

2. Vacuum chamber setup. After filling, each emitter is mounted in the test mount shown in Figure 3-18. The 3-axis translational stage is used to position the emitter tip around 100 μm from the extractor. In these tests, a solid extractor plate was used so that the effects of liquid instabilities or gas bubbles would not be missed. An extractor with a large aperture in front of the emitter tip may

obscure the results by permitting the swift removal of excess pressure or liquid jets that would otherwise be contained. Electrical connections are made to the emitter and extractor, and the pulse detector antenna is installed. The emitter setup is mounted onto the chamber flange, and installed on the chamber. The roughing and turbo pumps are turned on and the chamber is allowed to pump down for 1–3 hours (until the pressure reaches $\sim 1 \times 10^{-6}$ Torr).

3. Operation and data collection. At a sufficiently low pressure, the RGA is turned on and allowed to cycle through 2–3 sweeps and trends to burn off any contaminants collected on the filament between tests. The camera, power supply, and DAQ are turned on, and data collection begins at a sample rate of 10 Hz. A square wave with a 30 s period and $V_{pp} = 2 - 3$ V (see Figure 3-26) is provided to the HV amplifier which outputs 500 times the signal voltage. The voltage is modulated to maintain a current of roughly 500 nA throughout tests. The signal is also acquired by the Arduino board which triggers 100 single frames of the camera after a 3 s delay if the voltage is above abs(400) V (also shown in Figure 3-26). Emitters are operated for 0.5 h and then the chamber is vented.
4. Post-test inspection and data processing. Once the chamber has vented, emitters are removed from the setup, cleaned in the ultrasonic bath in acetone, dried, and imaged in the SEM. Data processing is fairly simple; current, voltage, chamber pressure, and discharge frequency are plotted in time. RGA data involves more synthesis but is again fairly straightforward.

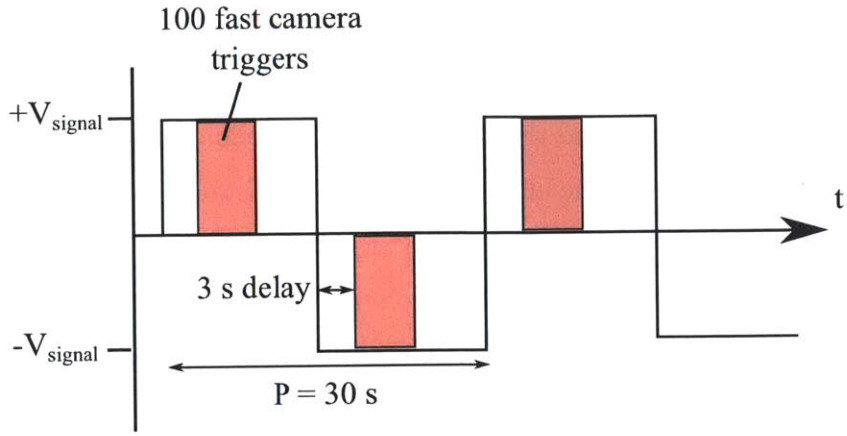

Figure 3-26: Signal output from Agilent to HV amplifier and Arduino. On $\pm V_{signal}$ the emitter begins firing; the Arduino receives the same signal, adds in a 3 s delay, and then sends 100 burst triggers to the camera.

3.3.3 Results and conclusions

In total, 45 experiments were performed; the primary result obtained from tests was whether discharges presented during firing. Figure 3-27 summarizes the results of the tests performed. These data, together with the filling conditions, polarity, and material, elucidate conclusions about the nature of electrical discharges in porous emitters, and offer insight into operating and design conditions that promote long-life operation for future iterations. The additional data collected, which include the emitted current, applied voltage, discharge frequency, high-speed imagery of the emission process, the chamber pressure, and the partial pressure of gas species present, supplement the conclusions.

The polarity, not included in Figure 3-27, did not affect the outcome at all. Emitters filled in gas atmospheres nearly always led to electrical discharges, which is in line with our hypothesis. Discharges that presented during tests in which emitters were filled in vacuum, however, were unexpected according to the hypothesis, which

	N	Y	Grand Total
Gas	**2**	**20**	**22**
Air	**1**	**8**	**9**
Glass		5	5
Ni	1	2	3
W		1	1
Ar		**4**	**4**
Ni		4	4
CO2	**1**	**8**	**9**
Ni	1	8	9
Vacuum	**4**	**5**	**9**
-	**4**	**5**	**9**
Glass		4	4
Ni	1		1
W	3	1	4
Grand Total	**6**	**25**	**31**

Figure 3-27: Binary discharge results for different values of variables tested.

stated that gas contamination that increases the local pressure or field or leads to liquid flooding/expulsion is the primary contributor to discharges. Further exploration revealed that the manufacturing challenges that led to the use of alternative emitter materials and therefore alternative liquid supply configurations described in Section 3.3.1 could lead to the same liquid flooding and expulsion as gas contamination. The test results are reordered against the degree of liquid containment and presented again in Figure 3-28.

	N	Y	Grand Total
Gas	**2**	**20**	**22**
Adequate containment	2	14	16
Inadequate containment		6	6
Vacuum	**4**	**5**	**9**
Adequate containment	4		4
Inadequate containment		5	5
Grand Total	**6**	**25**	**31**

Figure 3-28: Binary discharge results, reordered against containment variable.

A summary of findings from the tests follows:

1. Filling in a gas atmosphere led to discharges in 91% of cases. Tests showed the gas trapped in the substrate is released during operation, forcing liquid from the pores and inducing electrical discharges. Gas contamination can result from filling porous emitters with liquid in a gaseous environment whereby the liquid does not completely displace the gas and some residual volume remains, or from water vapor absorbed by the liquid that evaporates under certain conditions and can similarly force liquid from the pores. Discharges may be instigated by the gas itself which could provide the necessary particle population for ionization or the liquid protuberance or filaments during flooding and expulsion.
2. Filling in vacuum improved the outcome, but did not completely prevent discharges as predicted (56% of cases presented discharges). This technique inhibits both residual gas from filling and water vapor from the environment, and should have thereby precluded discharges. That discharges still occurred indicates that inadequate liquid containment within the pores, in this case referring to a large pool of liquid upstream that effectively increases the back pressure compared to the case where the liquid is fully contained with the pores[3], affects the balance between the applied electric field, the surface tension, and the hydraulic impedance and can lead to flooding and expulsion.
3. Filling in vacuum without a large liquid pool at the upstream pore entrances was the only successful method for preventing discharges. This method ensures the absence of contaminant gas and provides adequate liquid containment within the porous substrate.

[3]Large liquid pools are often successfully employed in electrospray but the hydraulics from the pool to the emission site are such that the balance for stable emission is still achieved, usually by leveraging viscous losses or gravitational effects.

Figures 3-29 through 3-31 provide some empirical context for the relationship between contaminant gas, liquid containment, and electrical discharges. Emitter

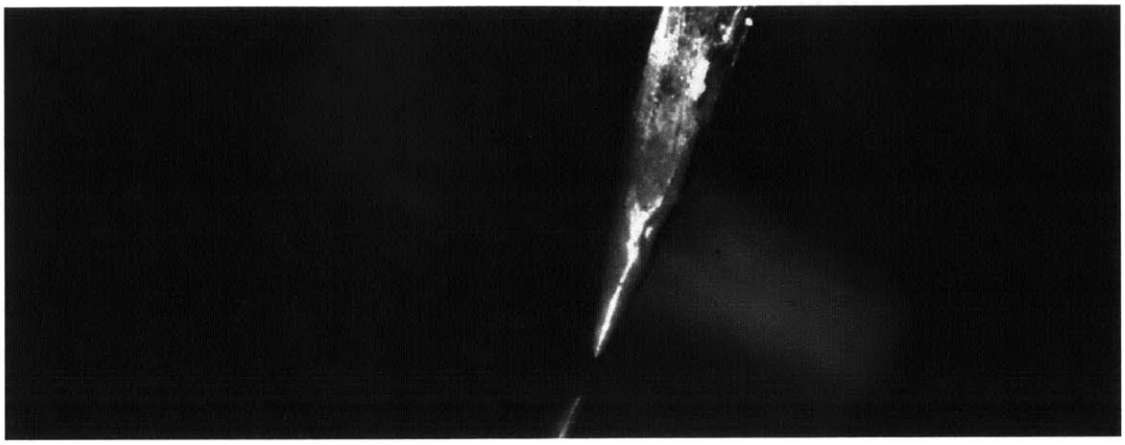

Figure 3-29: Frame from test of emitter A8. A8 is a porous nickel emitter filled with IL in a CO2 environment (a reflection of the emitter is in the lower left of the image). The image shows liquid and/or residue on the extractor that accumulated during firing, likely due to CO2 expansion and liquid displacement.

A8 in Figure 3-29 is a nickel emitter that was filled in CO2. Residue on the extractor is the result of expulsion of liquid from the substrate, likely subsequent to CO2 expansion during operation. Emitter W8 in Figures 3-30 and 3-31 is a tungsten emitter that was filled in vacuum but was mounted with a reservoir, and again residue is present on the extractor. A spark discharge was also captured in a frame. The visual data from tests of emitters filled in gas and those with reservoirs are strikingly similar in that liquid jets were observed and residue accumulated on the extractor, which also corresponded to measured discharges on the antenna. The shared theme in both scenarios that is consistent with the data is liquid perturbation or ejection from a pore. These effects can be generated by the expansion and release of trapped gas or water vapor, or flooding at the pore entrance in the presence of a destabilizing field. Each of these mechanisms is qualitatively discussed in Section 3.4. By contrast,

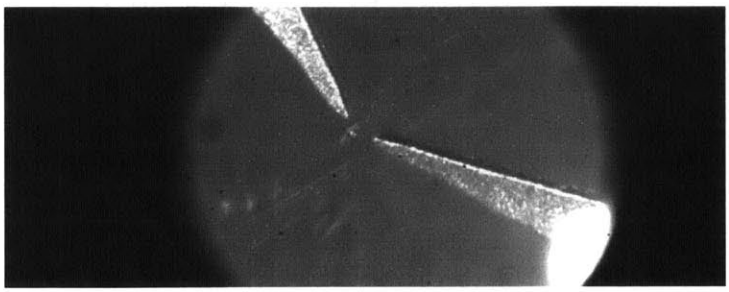

Figure 3-30: Frame from test of emitter W8. W8 is a porous tungsten emitter filled with IL in vacuum with a large upstream liquid pool. The image shows liquid and/or residue on the extractor that accumulated during firing, likely a consequence of the poor liquid containment.

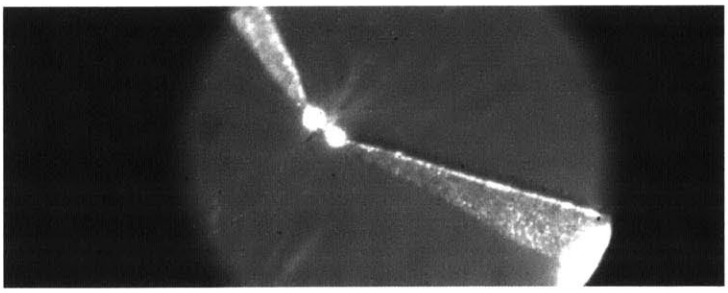

Figure 3-31: Another frame from test of emitter W8. This image captured a discharge between the emitter and extractor.

in operation of emitters filled in vacuum without large liquid pools, emission proceeds smoothly with no measured/observed discharges and no liquid accumulation on the extractor.

A summary of the supplemental data collected

A description of all tests performed and several tests' worth of data acquired are included in Appendix B. Results from redundant tests were omitted. Samples of the data collected from the current, voltage, discharge, and chamber pressure monitors, as well as the RGA are plotted in Figures 3-32–3-37. During the initial experimental design, we endeavored to collect RGA and optical spectrometry spectra to identify the species undergoing ionization in order to infer the causes of discharges. This undertaking proved more difficult than expected, for several reasons. The strongest impediments were related to time resolution and triggering. It should have been possible to trigger both spectrometers using the light released from a spark or arc. Unfortunately, without prior knowledge of the emission spectrum or q/m of the ionized species, it was challenging to scan the proper range. The mechanical grating stage of the optical spectrometer was unable to translate quickly enough to scan any useful range of wavelengths, and the RGA could not sweep through a range of AMUs quickly enough given its programmed averaging scheme. Time is also limiting when considering the time scale of electrical discharges ($\leq 10^{-9}$ s). Even if species signatures were detected, as shown in the RGA scans in Figures 3-33, 3-35, and 3-37, the measured species are likely products of thermal phenomena that persist after a discharge, such as vaporization of the ionic liquid or ablation of the material. Another challenge stemmed from the low levels of light emitted in all but the most severe sparks and arcs.

We can, however, make some observations from the data shown. Emitter W1 is a tungsten emitter filled in vacuum and fired without a reservoir. Figure 3-32 gives the applied voltage and emitted current (top), and the chamber pressure (bottom), over roughly 10 min of firing. Emission is stable and no discharges are observed. The general trend of the chamber pressure is a gradual decrease, as pumping continued throughout the test. Figure 3-33 shows the pressure of the gas species tracked throughout tests over the same time period. Most species show a positive fractional increase due to the decreasing total chamber pressure. H2, N2, H2O, O, and OH appear to have small peaks that correspond to emission in the positive mode. These are likely due to the cation and absorbed water. Emitter D1 is a nickel emitter filled in CO2 that also presented no discharges (Figure 3-34). The peaks in H2, N2, and N in Figure 3-35 are more pronounced, and again would suggest that their signature is a result of the cation being ionized in the quadrupole. Interestingly, there are no peaks in CO2, which is consistent with a later analysis that shows the relatively quick evaporation of CO2 from IL under vacuum. Also, unlike W1, there are no pronounced H2O, O, or OH peaks, suggesting the the longer pump down time (as evidenced by the lower total chamber pressure in Figure 3-34) removed more water vapor from the IL. Emitter Gl2 is a glass emitter, filled in air and mounted with a reservoir. This is an example of a worst-case scenario for electrical discharges, and our intuition is corroborated by noting their prevalence (marked by the red asterisks) in Figure 3-36. The RGA data in Figure 3-37 indicates air is released (from the Ar and CO2 peaks), and that no water was present, or at least was not among the species analyzed by the quadrupole. O and O2 are likely from CO2 from air. H2, H2, and N are likely from air and the cation.

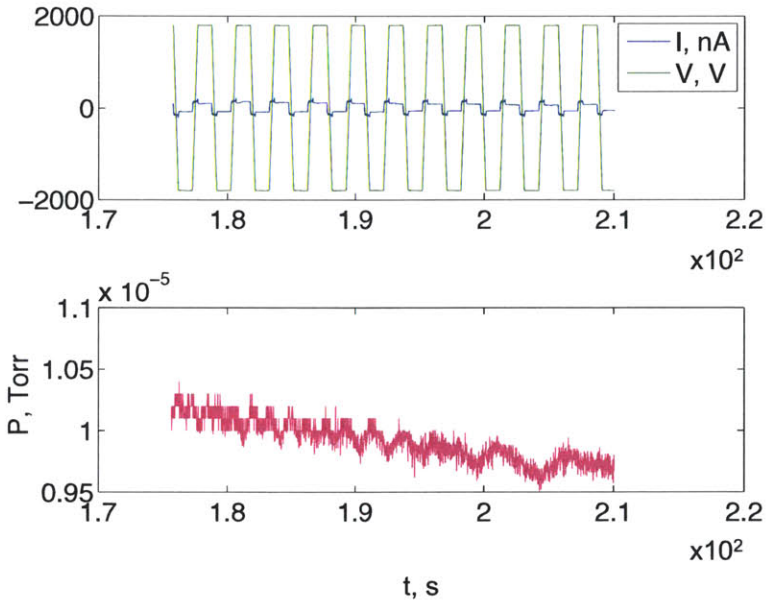

Figure 3-32: Emitted current and applied voltage (top) and total chamber pressure (bottom) over a sample of the test of emitter W1. W1 is a tungsten emitter that was filled in vacuum with no reservoir. No discharges presented; the chamber pressure continued to decrease throughout the plotted timeframe.

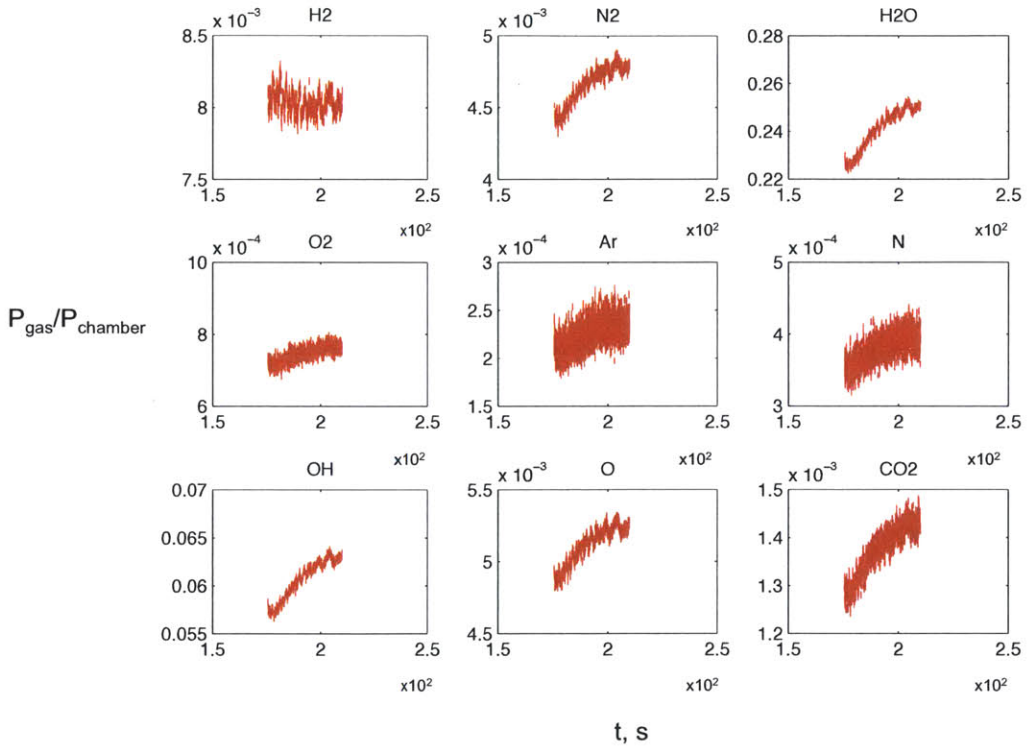

Figure 3-33: Gas pressures of species monitored during the test of emitter W1. Peaks in H2, N2, H2O, O, and OH are likely due to the cation and absorbed water.

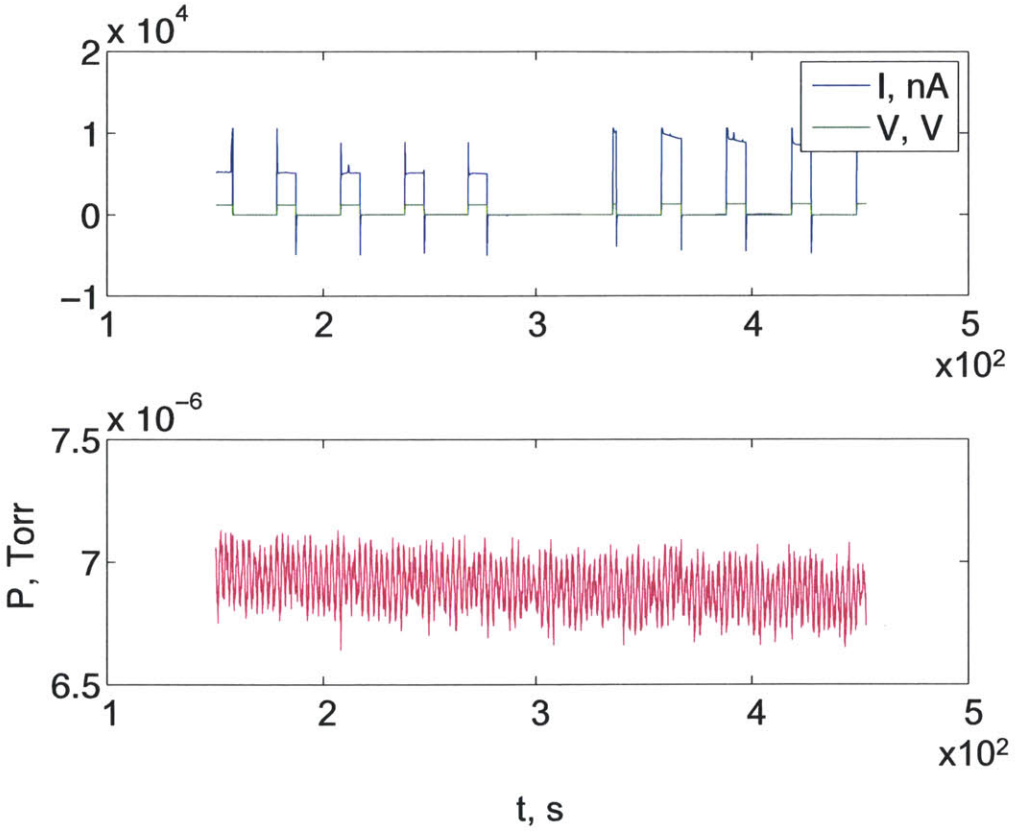

Figure 3-34: Emitted current and applied voltage (top) and total chamber pressure (bottom) over a sample of the test of emitter D1. D1 is a nickel emitter that was filled in CO2 with no reservoir. No discharges presented; the chamber pressure was very low during these tests and remained quite constant.

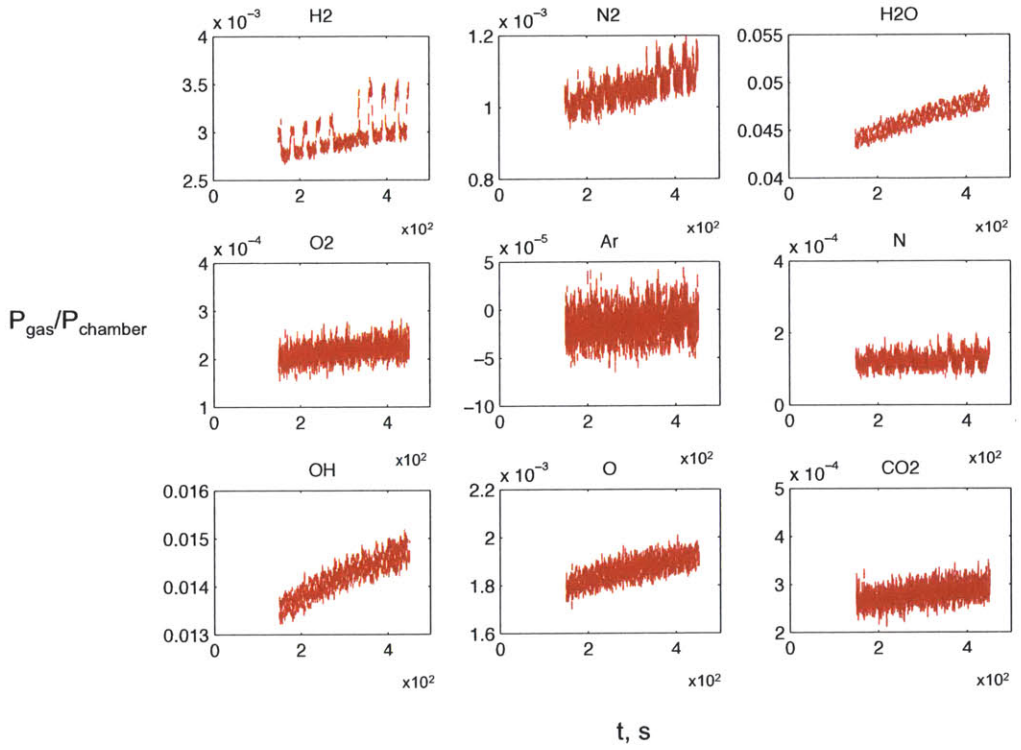

Figure 3-35: Gas pressures of species monitored during the test of emitter D1. Peaks in H2, N2, and N are likely due to the cation. No CO2 is observed, suggesting that the long pump down time removed it from the emitter.

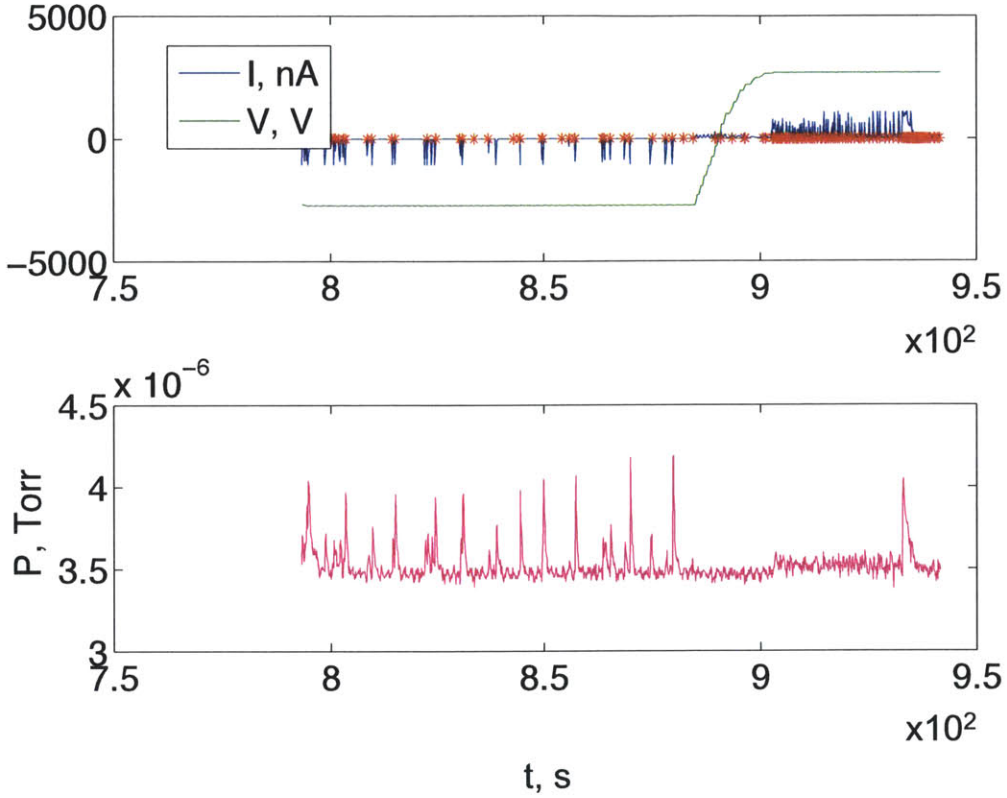

Figure 3-36: Emitted current and applied voltage (top) and total chamber pressure (bottom) over a sample of the test of emitter Gl2. Gl2 is a glass emitter that was filled in air with a reservoir. Discharges were extremely prevalent; peaks in the chamber pressure are very pronounced.

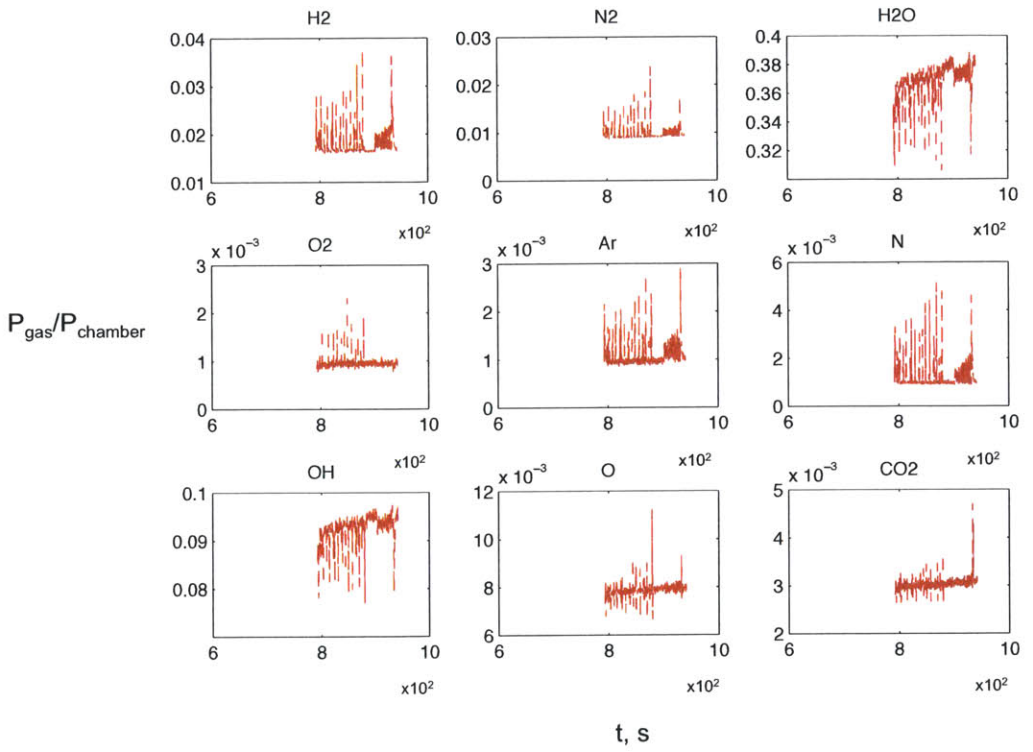

Figure 3-37: Gas pressures of species monitored during the test of emitter Gl2. Peaks in H2, N2, Ar, N, CO2, and O2 indicate air and the cation.

3.4 Qualitative discussion of liquid flooding and expulsion in porous ionic liquid ion sources

The experiments of Section 3.3 elucidated the correlation between the appearance of anomalously large liquid menisci on the surface of porous emitters and the onset of damaging electrical discharges that, in the worst cases, lead to source failure. This situation was shown to be a consequence of gas contamination or poor liquid containment within the porous substrate whereas during stable operation the liquid is drawn gently from the tip of a balanced electrified meniscus (e.g., a Taylor cone) in a jet of charged particles or a purely ionic beam.

The fact that these large menisci are susceptible to destabilization is unsurprising—Taylor cone formation and the charged particle emission that follows are results of liquid destabilization under the balance between surface tension, pressure, and electric traction. This balance occurs under conditions not far from what is required to promote the growth of unstable liquid shape modes. The challenge for long-life operation of ILIS free of electrical discharges then is to design within the boundaries of favorable mechanical balances while avoiding design and operating conditions that promote adverse ones. A discussion of this situation and insight into methods for addressing this challenge follow.

3.4.1 Equilibrium states of IL in a pore

At the exit of a substrate pore the liquid interfaces with the substrate material, the ambient atmosphere, and the applied electric field as well as liquid from nearby pores. As we now know liquid at the pore exit can also be acted upon by upstream disturbances, such as bubble expansion. At equilibrium assuming the liquid is fully

contained within the pore IL that wets the substrate will assume a concave meniscus within a pore; non-wetting IL will form a convex meniscus and needs to be forced in (Figure 3-38). Across the fluid interface of a pore with a circular cross-section,

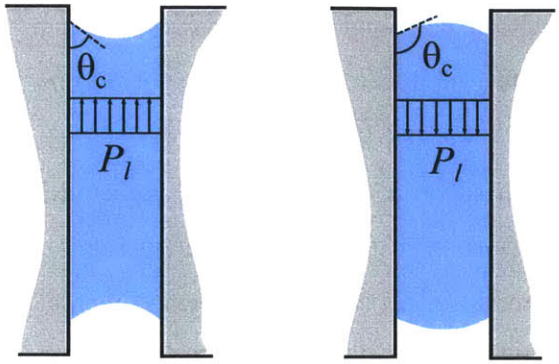

Figure 3-38: Equilibrium states of wetting and non-wetting liquid in a pore. In the wetting case, the contact angle is less than 90 deg., and the liquid is under tension. In the non-wetting case, the angle is greater than 90 deg. and the pressure is positive.

the pressure difference according to the Young-Laplace equation is a function of the interfacial tension, γ and the radius of curvature of the interface, r [89]:

$$\Delta P = \frac{2\gamma \cos\theta_c}{r_{pore}} \tag{3.41}$$

where θ_c is the contact angle and r was related to the pore radius by $r = r_{pore}/\cos\theta_c$. From Equation 3.41 and intuitively from Figure 3-38, it can be seen that the pressure within a wetting liquid will be lower with respect to the ambient pressure (or negative if outside is vacuum); that is, the liquid will be under tension. In a non-wetting liquid the pressure within the liquid will be higher relative to outside.

In the presence of an upstream disturbance such as the application of back pres-

sure or the application of an electric field at the pore exit, the conditions could be such as to cause the IL to meet the spillage conditions and subsequently to spill from the pores, providing the flooding or expulsion that instigates electrical discharges.

3.4.2 Spillage produced by the application a back pressure

A slight back pressure P_B applied to liquid within a pore, generated by the expansion of an upstream gas bubble for instance, will alter the shape of the liquid meniscus from that at equilibrium. If the back pressure is further increased such that it overcomes the surface tension force at the meniscus, the liquid will spill from the pore. The condition where the back pressure exactly equals the surface tension force is called the *spillage condition*: $P_B = P_{\gamma,s}$ where $P_{\gamma,s}$ is the surface tension force when the meniscus radius is a minimum and makes the spillage angle θ_s with the substrate outside of the pore (see Figure 3-39).

$$\text{Spillage condition} \quad P_B = P_{\gamma,s} = \frac{2\gamma \sin\theta_s}{r_{pore}} \tag{3.42}$$

If the liquid is wetting, $\theta_s = \theta_c$; for non-wetting liquid $\theta_s = 90$ deg such that the liquid forms a hemisphere with its center of curvature coplanar with the exit plane and its diameter equal to that of the pore. Any increase in P_B beyond $P_{\gamma,s}$ has the effect of increasing the radius of curvature of the meniscus which in turn lowers $P_{\gamma,s}$ and effectively pumps liquid from the pore (as long as $P_B > P_{\gamma,s}$ holds), a situation referred to as spillage (Figure 3-40).

For back pressure due to gas, if the spillage condition is exceeded and $P_{\gamma,s}$ is reduced the aggravating gas bubble may have a chance to escape from the pore[4]. If we are fortunate, this event does not short the device or provide the particle

[4]Bubble behavior in porous media depends on the surfactant properties among others [90, 91]

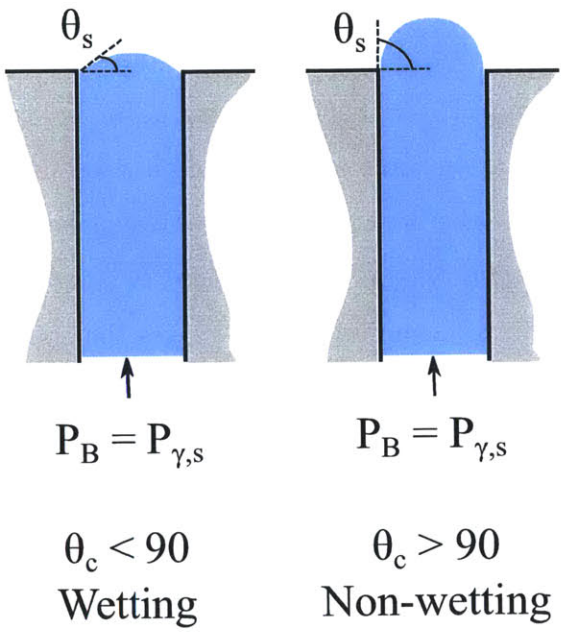

Figure 3-39: The spillage condition for both wetting and non-wetting liquid in a pore, met when a back pressure P_B has been applied such that $P_B = P_{\gamma,s}$ with $\theta_S = \theta_C$ for wetting liquids and $\theta_S = 90$ deg for non-wetting liquids.

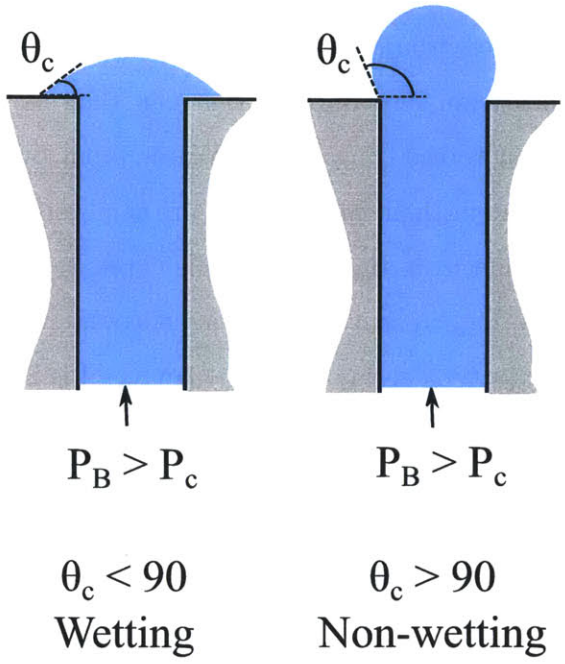

Figure 3-40: Spillage for both wetting and non-wetting liquid in a pore. If P_B is constant and greater than $P_{\gamma,s}$, the wetting liquid will spill from the pore, maintaining a constant contact angle θ_c with the substrate. This spreading increases the radius of curvature of the liquid, thereby reducing the surface tension pressure, and effectively pumping liquid from the pore until the IL is exhausted or P_B is removed or reduced below $P_{\gamma,s}$. With $P_B > P_{\gamma,s}$ in the non-wetting case, the liquid will form a droplet at the pore exit with a radius larger than the hemispherical condition, similarly reducing $P_{\gamma,s}$ and drawing liquid from the pore until it is exhausted, P_B is removed or reduced below $P_{\gamma,s}$, or the droplet detaches/is expelled from the pore exit.

population required for an electrical discharge of Section 3.2.3[5].

Gas contamination that provides this back pressure can occur via the more apparent mechanism (inefficient gas displacement during filling with liquid) but also from the nucleation of water vapor or other absorbed species. Hygroscopic ILs that readily absorb water from humid environments can absorb a quantity such that the concentration permits its nucleation into bubbles that can then expand and force liquid from the substrate similar to the trapped gas. Water vapor bubbles can only subsist within the porous substrate if their internal pressure can overcome the bubble surface tension, the surface tension from the liquid in the capillary, and the ambient atmosphere. Considering the high relative humidities encountered by spacecraft launch vehicles prior to launch (a typical day at Cape Canaveral is 80% relative humidity), it is not unlikely that the IL within an iEPS device will have the opportunity to absorb water vapor. The situation is analyzed in Appendix C. The results indicate that small pores provide sufficient surface tension to overcome the vapor pressure and prevent the nucleation of water vapor bubbles; instead, the soluble vapor will diffuse through the IL and evaporate from its surface in a timescale similar to that by which it was absorbed. Electric traction effectively reduces the surface tension at the pore exits as Section 3.4.3 will show, so as a corollary to this conclusion, adequate time should be allowed in low RH environments prior to application of the electric field (operation). For our pore sizes of interest, 3 h of outgassing is recommended. Furthermore, this result also implies that similarly soluble gases, such as CO2, could be used as filling gases as long as outgassing was permitted before operation began. From a practical perspective, this would likely be a welcome approach as a glove box configuration could be used for filling, compared to vacuum filling where onerous

[5]No electric field was included in the spillage condition in this section, though it is fair to assume that one is present though its destabilizing potential was much less than that of the back pressure.

manipulation within the vacuum chamber via stages and transporters is required.

3.4.3 Spillage generated and aggravated by an electric field

Electric fields can engender the same spillage situations just discussed—flooding or droplet detachment/expulsion (recall Figure 3-40). The field exerts a traction that pulls at the liquid meniscus, perturbing it similar to the application of a back pressure. In one scenario, the applied field continues to draw liquid from the pore until the device fails, perhaps via flooding or expulsion and shorting. In a second scenario, the liquid is further stressed at the pore exit and the field intensifies as the radius of curvature is reduced, achieving a stable solution for the shape of the liquid similar to a Taylor cone (see Section 1.2). Even if liquid has spilled from the pore as described above a stable mode of operation may still be tenable for the realized surface tension, flow rate, and electric field. The field required to destabilize a pool of liquid is presented in Appendix D. And on the other hand a further increase in the electric field could destabilize even a stable cone shape if disturbances can still be generated along its surface.

In Figure 3-41 one possible sequence of this complex electrohydrodynamic process is illustrated. A back pressure is applied to liquid in the capillary, causing the meniscus to protrude from the capillary exit. The applied voltage is increased, and the liquid stresses further. Excess liquid continues to be shed in a violent oscillatory manner under the effects of the unbalance of surface tension and electric stress (electric stress is larger) produced by the field as the voltage is increased in frames 3 and 4, and eventually the liquid assumes a stable conical shape.

We avoid oversimplifying the process to determine whether the application of an electric field will produce adverse affects or the desired Taylor cone under different

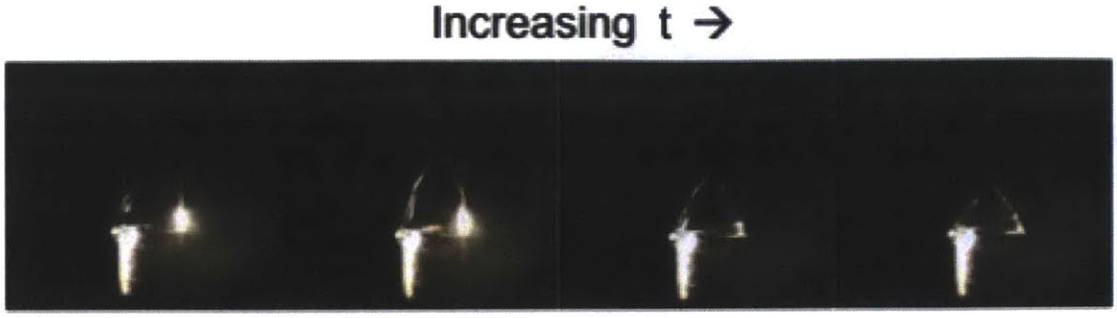

Figure 3-41: Capillary emitter with electrolyte with a back pressure applied. In frame 1, a small field is applied and the meniscus indicates the capillary is pressurized. In frame 2, the liquid becomes unstable. In frame 3, the cone volume has decreased but the cone is still fairly unstable and continues to shed liquid. In frame 4, a stable Taylor cone configuration has been achieved. The cone volume is plainly less than in all previous frames, implying that the larger volume at the initiation of the sequence did not have adequate capillary tension to support a stable configuration for a given potential distribution. Courtesy of MIT SPL.

conditions. Several bodies of work provide a deeper understanding of the propensity for attainment of a stable mode [92, 93, 94, 95]. Instead we address the remaining question that derived from the experimental results of Section 3.3 and explore how this delicate balance is modified when the capillary upstream pressure of the ideal pore is effectively removed (say by adding a liquid reservoir with much larger pores, for instance).

Figure 3-42 illustrates the ideal configuration of liquid contained within a pore compared to a pore with a liquid pool at the entrance. The latter is the situation encountered during tests of tungsten and glass emitters and was shown to contribute to shorting and electrical discharges. A device designed for the situation on the left has a prescribed electric field E_o which may achieve the desired balance between surface tension, electric field traction, and hydraulic impedance permitting smooth charged particle emission from the Taylor cone. The prescribed field incorporated

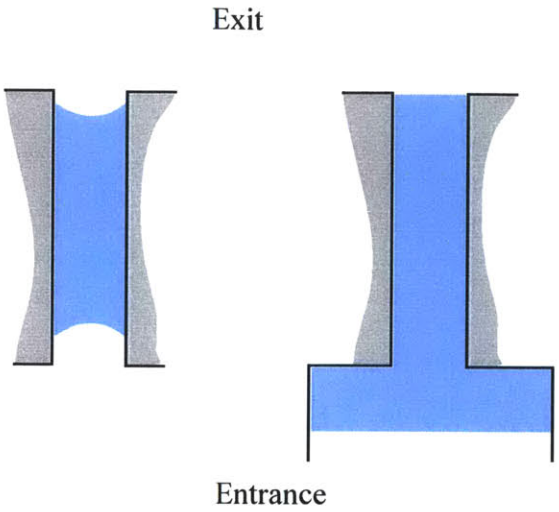

Figure 3-42: A pore of constant or similar diameter along its length, filled with wetting liquid (left); a pore with a large pool at the entrance (right).

the assumption that the liquid was fully contained within the pores. E_o applied to the pore with the large pool with no net curvature and therefore no surface tension at the entrance will likely not achieve the same balance, and based on our experimental results we conjecture that spillage could occur. Neglecting gravitational or viscous effects, the pressure balance for both situations with a field applied is illustrated in Figure 3-43.

The (oversimplified) example shows that for the pore with the liquid pool, the applied field will be too strong to achieve balance given the absence of upstream surface tension. Effectively, a back pressure has been applied in this scenario, and the electric field is more likely to cause spillage as we saw during tests. In the same video sequence of Figure 3-9 pictured here again in Figure 3-44, the electric field traction at the side of the emitter is strong enough to stress the meniscus and prompt spillage of liquid from the pore, likely aided by the expansion of a bubble or a nearby gas burst. The meniscus continues to grow, and eventually a conical meniscus

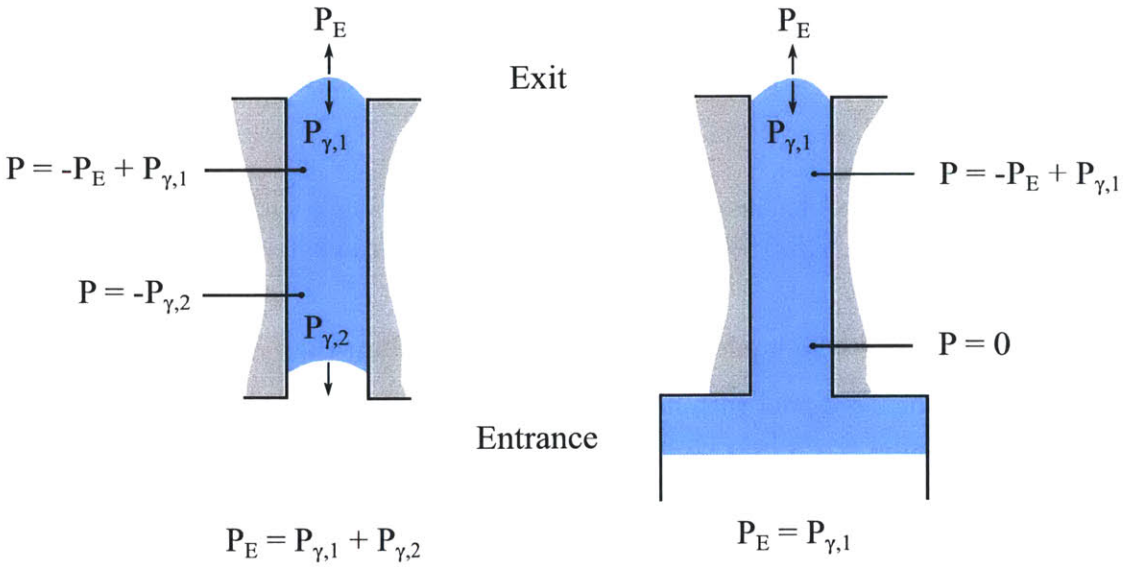

Figure 3-43: Pressure balance under applied field for pore with full liquid containment compared to that with a large pool at the pore entrance. The absence of net curvature at the upstream meniscus in the latter case means the applied field could overcome the surface tension at the exit and promote spillage from the pore.

is achieved that spans multiple pores. At this point, the applied field overcomes the surface tension and the bubble escapes, followed likely by a discharge forcing the carbonization of the liquid.

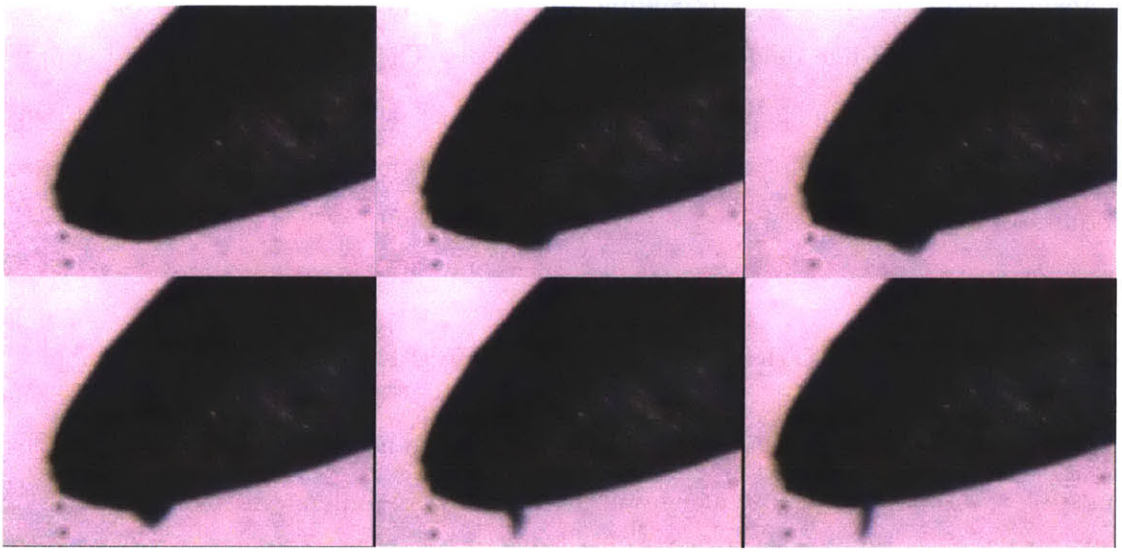

Figure 3-44: The same sequence shown earlier recorded during testing of a single porous nickel emitter filled with IL in atmosphere. The destabilizing effect of the electric field on large liquid menisci is evidenced by the liquid protuberance growing on the bottom of the emitter. The field continues to exert traction on the liquid likely aided by the expansion of a gas bubble, drawing more liquid from the substrate until the flooded area is large enough to form a Taylor cone. Eventually the aggravating gas bubble escapes and a discharge occurs that carbonizes the liquid, leaving behind a solid filament.

3.4.4 Summary of the effects of back pressures and electric fields on spillage

Both back pressure produced by gas expansion and electric traction can force liquid from the porous substrate, leading to flooding or expulsion which were shown to

promote electrical discharges or other failure mechanisms. Avoiding these situations is critical to the successful operation of porous ILIS. Filling emitters with liquid in vacuum or in soluble gases that evaporate from the surface without nucleating, and allowing adequate time for any soluble filling gases or absorbed species is recommended. For iEPS-like devices, 3 h is appropriate. The design of the liquid supply path from any reservoir to the emission site should be carefully managed as to maintain the balance between the electric field, surface tension, and hydraulic impedance required for stable emission.

3.5 Conclusions and future work

Through this work, electrical discharges were identified as a severe life-limiting mechanism for porous ILIS. Consequences of discharges were understood to be shorting of the power electronics, carbonization of the IL, current loss into the grounded extractor, device heating, and material ablation. Discharges that do not cause immediate source failure may decrease overall system efficiency. An analytical method for predicting discharges was discussed, though the complex electrohydrodynamic processes in discharges in electrospray likely render the analysis only partially complete. Tests of emitters of various materials and filling conditions were performed, in which optical and spectroscopic techniques were combined with a measure of discharge occurrences, applied voltage, and emitted current. The tests led to an enhanced understanding of the factors that support discharges: liquid flooding and expulsion from the porous substrate consistently led to discharges and source failure, and could be produced by contaminant gases or strong electric fields. These factors were then qualitatively explored to aid in the successful long-life of porous ILIS emitters. The recommendations for avoiding discharges in practical implementations, particularly in those with

ionic liquid tanks, follow.

1. Fill porous emitters in vacuum to avoid contaminant gas that produces back pressures and can lead to liquid expulsion or flooding.

2. Avoid unintentional large liquid menisci anywhere along liquid flow path unless compensated for by viscous pressure loss or other mechanisms. Along the same vein, propellant supply tanks should be porous, with a pore diameter from the tank to the emission site that monotonically decreases to promote capillary flow.

3. Substrate permeability everywhere should be tailored to achieve an adequate hydraulic impedance for particular design and operating conditions.

4. Address the potential for pressurization of the supply tank by gas-generating electrochemistry at the distal electrode through techniques such as voltage alternation or physical design and containment (eg. include a valve in the tank that allows gas to escape).

5. Manage the wetting state of the substrate surface to prevent flooding.

Though this work has practical significance and has resulted in actionable steps for the near-term toward avoiding discharges in porous ILIS, obtaining a detailed understanding of the discharge process and a model for more accurately predicting its onset will be equally if not more challenging. Several questions remain to be answered through future work, and we offer thoughts and lessons learned where applicable:

1. What species are being ionized during a discharge? This question was challenging to answer during this work, primarily because of the time resolution

of spectroscopic measurement techniques. Possible sources of particles for ionization include the cathode, contaminant gas, or IL. In positive mode, the cathode is the stainless steel extractor, which is likely being sputtered by impinging ions, contributing to the pressure in the gap. It is unlikely that this mechanism alone supports discharges as some tests in positive mode where the full beam was fired into the extractor were performed without discharges. In negative mode, the cathode is the emitter and IL. Depending on the emitter material and the particular liquid, secondary emission may be more prevalent than assumed. Alternatively, current passing through thin channels of IL could force its decomposition into gas, providing the particles for ionization or carbonization without discharges. And contaminant gas could be ionized, though a further challenge once identification is achieved will be to discern whether the observed ionized species instigated the discharge or were merely present.

2. What is the source of heating for carbonization and ablation? The energy for these processes can be determined and related to the energy transferred by arc discharges, elucidating properties about the plasma that would be required to support this kind of heating. Similarly, the possibility of ohmic heating to engender these results can be evaluated.

3. How do liquid protuberances and filaments alter the electric field and the propensity for discharges? Thin, rod-like structures could produce extremely high fields compared to the emitter tip itself. These filaments could also bridge the gap between the electrodes, initiating a current channel that vaporizes and then ignites in an arc. A preliminary study of a thin rod of charge at the emitter apex was performed but did not alter much the results of the Townsend criterion. Coupled to thermal processes, this analysis may prove more con-

structive.

4. How and where are discharges initiated? It remains to be seen how observed sparks are initiated. High-speed recording triggered by current surges could provide insight into the structure of the discharges and their formation processes. During these tests, data transfer and writing rates limited the speed at which footage could be obtained.

5. What is the discharge current during an event? Discharges can be loosely characterized by their current, so a reliable measurement of the current drawn during such an event could provide another hint to the process. The measurement could be obtained via a small inductor placed near an the tip of an emitter.

6. How does the anode–cathode configuration alter the outcome? We mentioned the material difference between the two, but the electrode geometry should influence discharge formation as well. No noticeable difference was discerned through these tests, but all else being equal the onset voltages for discharges should vary between the scenarios.

Chapter 4

Other life-limiting effects

Ion electrospray propulsion systems and ion engines in general face other life-limiting factors that arise from their operational environments and manufacturing or assembly tolerances. Here, three of the most critical factors are discussed.

4.1 Grid erosion

Grid erosion is a life-limiting mechanism in ion engines [96]. At low currents, charge-exchange collisions between ions and neutrals send the newly formed low-speed ions into the grid, resulting in a regime referred to as "barrel erosion". At higher currents, the beam edges are intercepted by the grid, resulting in a destructive mode of operation that designers work to avoid. As erosion proceeds, eventually enough material is sputtered away that the grid can no longer prevent backstreaming electrons, or it fails structurally [7]. Ions from the beam can also return back to the grid, damaging it, distorting the field, and shorting the neutralizer. These processes in ion engines remain the most important wear mechanisms. The NSTAR grid after 30,000 hours

of operation is shown in Figure 4-1. Deep erosion of the grid is evident, with full penetration occurring in some regions. Propellant choice can be used to alleviate grid

Figure 4-1: SEM photograph shows that sputtering in the webbing between the holes had almost destroyed the structural integrity of the NSTAR grids [7].

erosion—relative sputtering yields for Hg, Ar, and Xe are 1, 4, and 2, respectively.

ILIS can interact with the downstream extractor electrode if the emitted ion beam is not perfectly aligned with the aperture similar to grid erosion in ion engines caused by beam-edge impingement. Perez *et al.* [2] determined the sputtering yield, S, of an ILIS with EMI-BF4 on a silicon target to be 6 at an ion energy of 10 keV. As a first-order approximation, assume $S \propto E$ so that the sputtering yield for $E_{ion,iEPS}$ is

$$S_{iEPS} \propto S_{[2]} \frac{E_{ion,iEPS}}{E_{[2]}} \approx 0.48 \tag{4.1}$$

Kieckhafer and King [8] measured the sputter yield of carbon atoms due to ion irradiation from krypton, xenon, and bismuth, plotted in Figure 4-2 over a range of ion energies. Since neither of these data correspond exactly with our conditions ($E_{ion,iEPS} = 1$ keV, EMI-BF4 ions), it is reassuring to see that they are of the

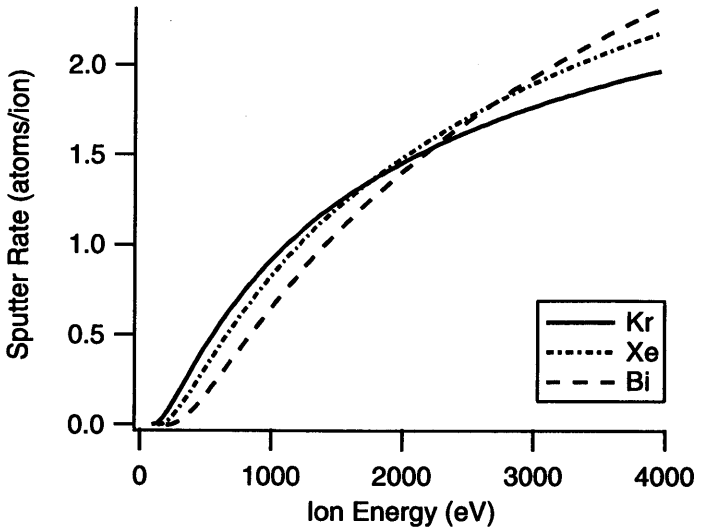

Figure 4-2: Sputter rate from [8].

same order, and we assume the sputter time through the silicon extractor electrode computed as follows is of the right magnitude:

$$t_{grid} = \frac{n_{Si}}{\dot{n}_{sputter}} \tag{4.2}$$

where n_{Si} is moles of silicon corresponding to the beam area times the grid height (see Figure 4-3) and

$$\dot{n}_{sputter} = S_{iEPS}\frac{I}{q} \tag{4.3}$$

Somewhat surprisingly, $t_{sputter}$ for $h = 100$ μm, $D = 100$, $\Theta = 20$ deg is on the order of tens of minutes. However, there are several caveats to consider. First, the analysis assumed the entire beam area impinged on the extractor. In reality, given the size of the apertures in the extractor grid compared to the beam half-angle, misalignment would have to be extreme for this to be the case. Take the above

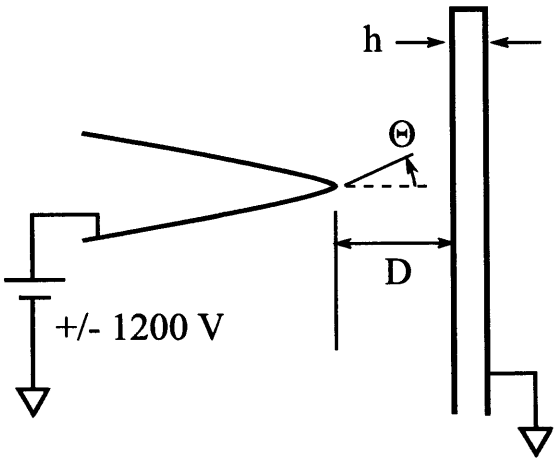

Figure 4-3: Beam sputtering geometry.

Table 4.1: Sputtering time for different yields from the literature.

S	Source	$t_{sputter}$, s
0.48	[2]	1632 s
0.8	[8]	979 s

geometry and $r_{extractor} = 200$ μm. In order for the beam to intersect the extractor for a well-aligned beam, the emitter tip would have to be misaligned by

$$\delta = r_{extractor} - r_{beam} = r_{extractor} - D\tan\Theta \approx 82\ \mu m \tag{4.4}$$

Early versions of iEPS showed $\delta \sim 20$ μm; more recent measurements indicate misalignment has been decreased to less than 10 μ m.

Second, we have not defined grid erosion failure. Penetration through the extractor that is confined to a small area at the edge of an aperture would not cause structural failure, but could cause enough backsputtering of material to clog the pores or alter the electric field affecting ion emission. The former issue is an important one but is outside the scope of this work; the latter is investigated here. COMSOL Multiphysics is used to compute the electric field profile for an emitter positioned below an aperture in an iEPS device. The norm of the electric field for the nominal case of $r_{extractor}$ is shown in Figure 4-4. Next, the electric fields for $r_{extractor} \pm 100$ μm are given for comparison in Figure 4-5. Variations in the maximum of the field are given in Table 4.2.

Table 4.2: Variations in electric field norm for different extractor aperture radii.

$r_{extractor}$, μm	$\|E_{max}\|$, V/m	% variation
100	6.25E7	17
200	5.33E7	–
300	4.56E7	15

We conclude from this discussion that unless the emitter is grossly misaligned to cause a change in aperture radius of > 50 μm, the change in the electric field would not be significant enough to cause device failure. Likely, if the aperture is enlarged due to erosion, the applied voltage could be increased to compensate for the change.

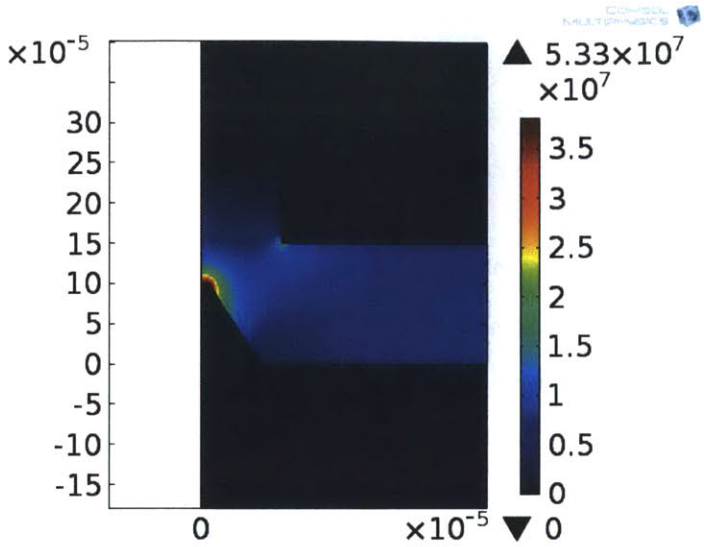

Figure 4-4: COMSOL model of norm of electric field for an emitter in an iEPS device for $r_{extractor} = 200$ μm.

4.2 Environmental effects

Spacecraft are exposed to several threats from their environment, such as radiation from high-energy particles, and bombardment by micrometeorites.

4.2.1 Radiation

Radiation concerns the power electronics, general electrical insulation, and ionic liquid stability in iEPS devices. Researchers at NASA JPL and Busek Co. investigated the effects of gamma radiation on the IL EMI-Im selected for the ST7 mission [97]. Samples of EMI-Im were exposed to 2x and 20x the expected dose of radiation for the one-year mission. The summarized results showed that there was no significant change in the bulk chemistry of the liquid; some breakdown of the parent compound was evident in the production of CF_3 and SO_2, and the fluid was slightly yellowed;

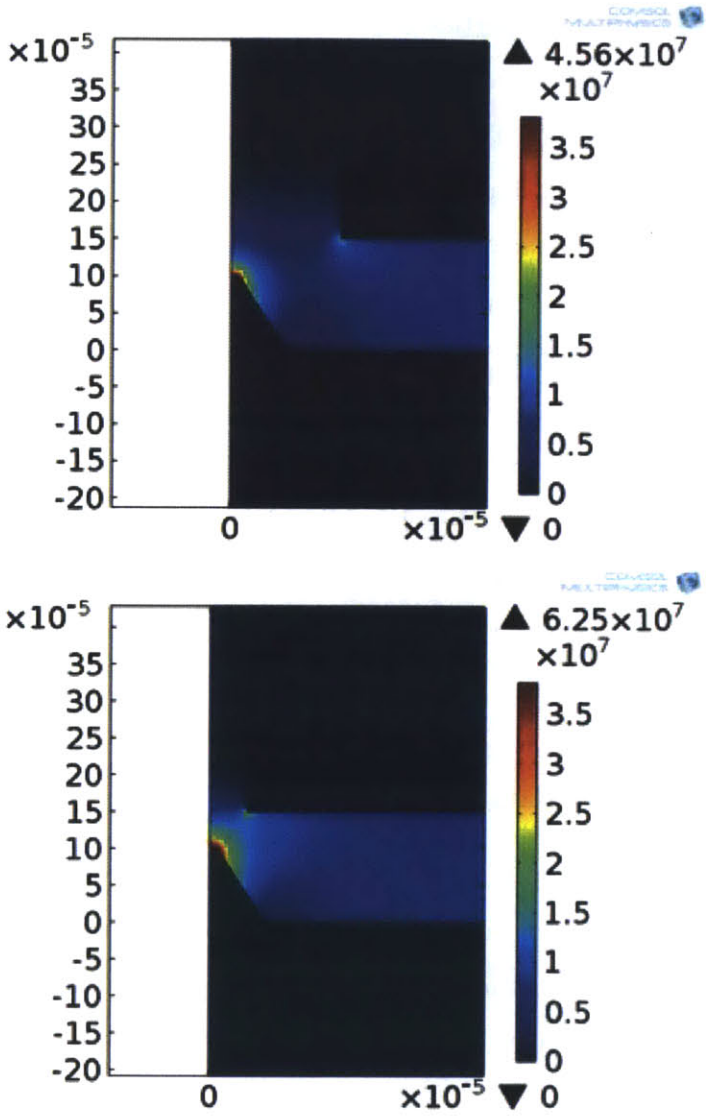

Figure 4-5: COMSOL models of norm of electric field for an emitter in an iEPS device for $r_{extractor} = 100$ μm (top) and 200 μm (bottom).

the refractive index was altered; and the contact angle increased. While interesting, the results are not cause for concern because of the high doses used and the relatively constancy of more critical properties such as the conductivity and current-voltage characteristic.

A study was performed on the power electronics for an iEPS device. The test used the 88-inch cyclotron at Lawrence Berkeley Laboratory to generate a beam of 50 MeV protons. During irradiation, the electronics were run continuously in the normal operating mode. Survival of the electronics up to 1 krad was the objective; a total dose exceeding 10.5 krad was applied and the electronics survived, save for a computer restart.

Allen *et al.* [98] examined the radiation resistance of 1,3-dialkylimidazolium-based ionic liquids, and found that they are relatively resistant and showed no major decomposition of the organic component after irradiation by alpha radiation from a tandem Van der Graaff generator, beta radiation from a linear accelerator and gamma radiation from cobalt 60 sources.

4.2.2 Micrometeorites

At velocities up to 17,500 mph, even micron-sized micrometeorites pose a threat to spacecraft because of the high energy they impart upon impact. The probability of impact with a micrometeorite can be determined from their fluence, F, at LEO (in number per area per year, given in Figure 4-6 from [9]):

$$P = Ne^{-N} \tag{4.5}$$

where $N = FAt$ with A being the impact area and t the mission time. The probability distribution is shown in Figure 4-7. According to this model, a 1U CubeSat in LEO

for two years has a roughly 2% chance of being struck by a micrometeorite 30 μm in diameter.

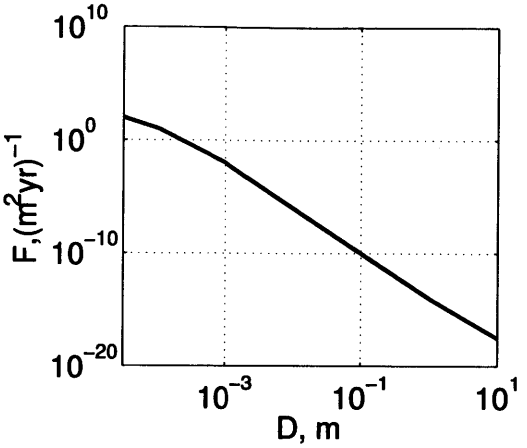

Figure 4-6: Micrometeorite fluence distribution by diameter at LEO, adapted from [9].

A 2% chance of collision is not insignificant, and designers of high-cost small satellites may wish to incorporate shielding.

4.3 Conclusions and future work

It is not expected that iEPS will fair worse due to grid erosion or the space environment than other ion engines or propulsion devices. One important area that should be pursued further is the effect of sputtering of the grid material back onto the emitter substrate. It was shown that $\sim$ kV ions are capable of eroding a grid onto which they are impinging; the fate of the sputtered material could be investigated by analyzing the composition of the surface of any components that may become sputtering targets such as the emitter substrate or nearby spacecraft components. Further studies on the effects of radiation on the thruster head itself and the

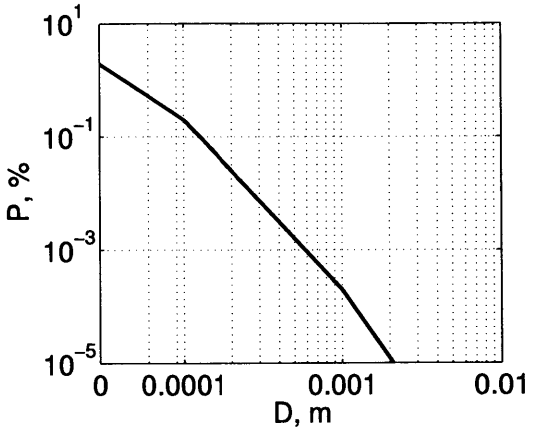

Figure 4-7: Probability of impact at LEO for an impact area of 30 μm and a two year mission.

power electronics are recommended before embarking on any long-duration missions, especially through high radiation environments.

Chapter 5

Conclusions

The contemporary shift in the space industry toward smaller, less expensive, but highly capable spacecraft is spurring research and technology development in several exciting areas. Ion electrospray propulsion development has been ongoing in the SPL at MIT over the past decade, and the technology offers a promising approach to micro spacecraft propulsion. Many attractive small satellite missions require long thrusting times to reach desired orbits from rideshare launches, or to compensate for drag at LEO, as two examples. The objective of this research has been to extend the lifetime of ion electrospray propulsion to help enable micro spacecraft.

Electrochemistry had long since been identified as a life-limiting mechanism, but its onset and consequences for the system were unclear [33, 3]. Early tests and analyses described in Sections 2.2.2 and 2.3.2 showed that the onset of electrochemistry began much sooner than previously thought, and experiments verified the diffusive nature of the EDL from the apex of an emitter along z. Though certainly a welcome discovery, this meant that reasonable frequencies of the power supply (¡ kHz) would not be enough to curb electrochemistry and a new approach had to be devised. In

Section 2.3.1, we introduced the distal electrode method for making contact with the liquid itself, and the potential for dielectric emitter materials. Previously, this technique had been used in electrospray as a means for forcing electrochemistry to study its effects [62]. In this implementation, a comparatively large distal electrode, or at least one with a large surface area, is employed to provide the electrical contact to the liquid, and the integrity of the emitter tips is preserved as they do not participate in the electrical processes. The technique was validated through several tests presented in Section 2.3.2 in which liquid reservoirs were made from conducting materials and the emitter was left floating. Considerations were discussed for sizing the distal electrode, and potential areas for future exploration such as gas generation at the electrode in Section 2.4. Through the distal method, both ILIS and iEPS maintain reasonable frequencies ($\sim 1 - 10$ Hz), avoid complex metal emitter fabrication processes, and achieve successful long-life operation, or at least lifetimes that are not limited by electrochemistry.

Surprisingly, once electrochemistry was satisfactorily understood and mitigated, the dark residues and premature failure persisted during tests. These had been thought to be caused by some interaction with the products of electrochemistry with the liquid, and should have been remedied with the distal electrode solution. The second half of this thesis, starting with Chapter 3, focused on identifying this distinct life-limiting mechanism, its causes, and methods for its prevention. After some ad-hoc experiments with a high-voltage coil and filter paper saturated with ionic liquid, followed by firing an emitter in vacuum with a microscope and camera trained on it, electrical dischargers were visibly confirmed, and their presence was seen to result in the same dark residues observed in the years prior (Section 3.1.5). The polycondensation, or specifically carbonization, of the IL is indicative of high-temperature processes, possibly due to arcing [6]. First-order approaches were unable

to provide a complete picture of the discharge phenomenon due to the complex fluid, thermal, and plasma processes involved, so an experimental approach was undertaken in Section 3.3. Tests were performed under varying conditions to determine which promoted discharges and which did not. At the end of experimentation, the data, presented in Section 3.3.3, showed that liquid flooding and expulsion from the porous substrate are the primary contributors, and can be produced by residual gas in the pores, inadequate surface tension from large menisci, or destabilizing fields. Qualitatively, these mechanisms were explored in Section 3.4 and actionable recommendations for practical implementations are provided based on the results, which include filling porous emitters with IL in vacuum or soluble gas environments and avoiding large liquid menisci such as can be found in pool reservoirs unless adequately balanced by viscous or gravitational losses along the flow path to the emission site. Several suggestions for future work that will expound on the phenomenon are offered 3.5.

As complicated electrohydrodynamic micro scale devices that are exposed to a harsh environment, electrochemistry and electrical discharges are not the only life-limiting mechanisms. Other phenomenon are described in Chapter 4, including erosion of the extractor grid from ion irradiation and environmental effects like radiation and micrometeorite impact.

Ultimately, these efforts uncovered and provided methods for mitigation of severe life-limiting mechanisms of ILIS and iEPS. In the very near term, the contributions will hopefully prove valuable for the Space Propulsion Lab's current development programs with lifetime goals on the order of 500 h, and in the longterm for the promise and viability of small satellites and other ground-based applications.

Appendix A

Circuit drawings for test setup

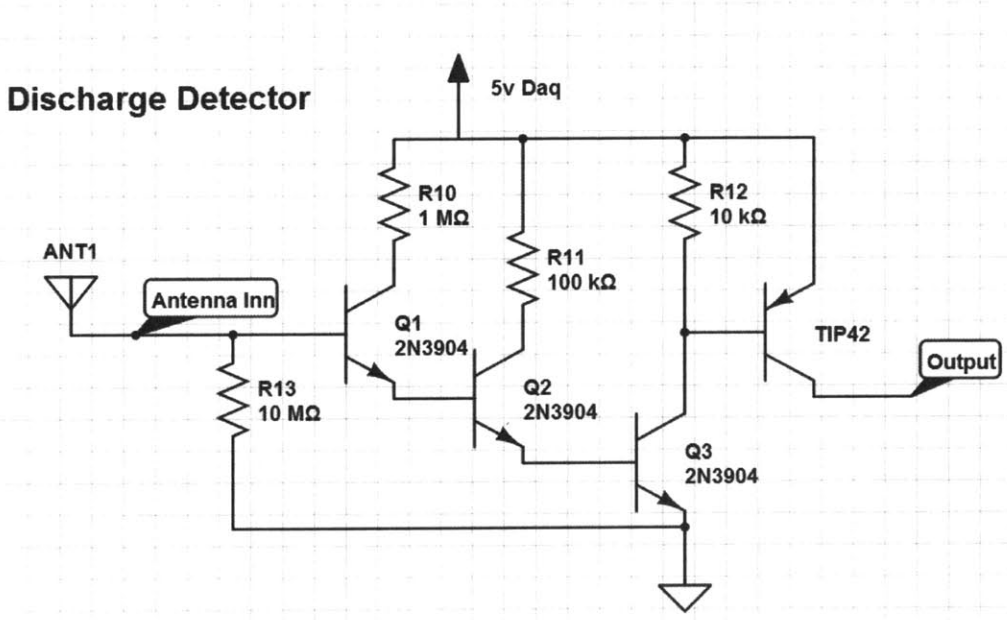

Figure A-1: Electromagnetic pulse detector circuit.

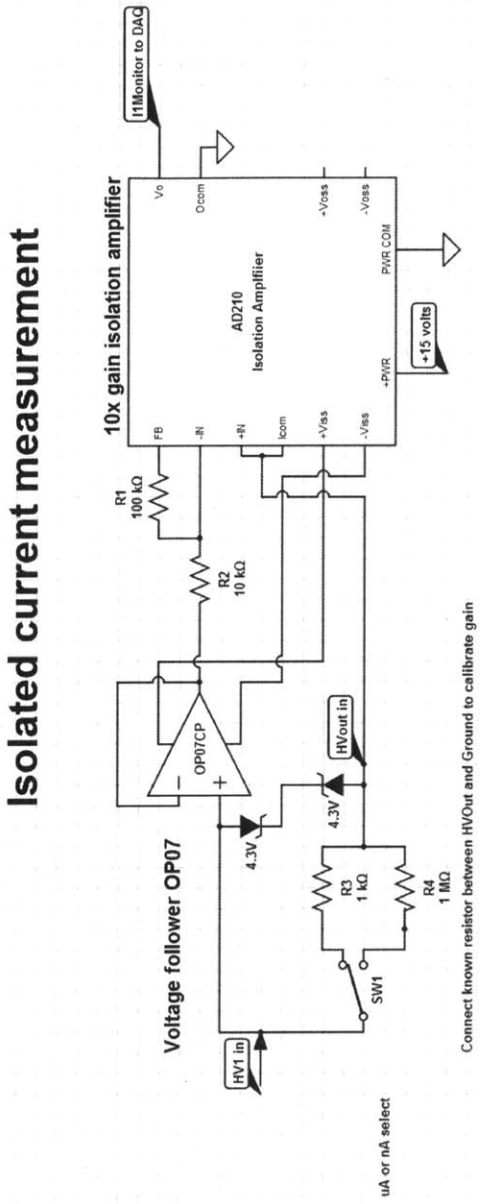

Figure A-2: Current amplifier circuit.

Appendix B

Processed data from discharge tests

Tests 1 and 2 were performed early in this work and laid the groundwork for the bulk of the experimentation but the full set of data was not collected at the time; tests 3–14 had the full set of data; and tests 15–32 were missing one or more data outputs though the binary outcome was still obtained.

Test No.	Emitter name	Filling condition	Filling gas	Material	Discharges	Reservoir?	Pore size
1		Vacuum	-	Ni	N	N	2-5 um
2		Gas	Air	Ni	Y	N	2-5 um
3	A2	Gas	Ar	Ni	Y	N	2-5 um
4	A3	Gas	CO2	Ni	Y	N	2-5 um
5	D1	Gas	CO2	Ni	N	N	2-5 um
6	E9	Gas	Air	Ni	Y	N	2-5 um
7	F1	Gas	Air	Ni	N	N	2-5 um
8	H8	Gas	CO2	Ni	Y	N	2-5 um
9	Gl2	Gas	Air	Glass	Y	Y	2-5 um
10	Gl2	Gas	Air	Glass	Y	Y	2-5 um
11	W3	Gas	Air	W	Y	Y	<1 um
12	Gl6	Gas	Air	Glass	Y	Y	2-5 um
13	W1	Vacuum	-	W	N	N	<1 um
14	W1	Vacuum	-	W	N	N	<1 um
15	A1	Gas	Ar	Ni		N	2-5 um
16	A7	Gas	CO2	Ni	Y	N	2-5 um
17	C2	Gas	Ar	Ni	Y	N	2-5 um
18	E3	Gas	Ar	Ni	Y	N	2-5 um
19	F2	Gas	Ar	Ni	Y	N	2-5 um
20	F5	Gas	CO2	Ni	Y	N	2-5 um
21	G1	Gas	CO2	Ni	Y	N	2-5 um
22	G2	Gas	CO2	Ni	Y	N	2-5 um
23	G7	Gas	CO2	Ni	Y	N	2-5 um
24	G9	Gas	CO2	Ni	Y	N	2-5 um
25	Gl1	Gas	Air	Glass	Y	Y	2-5 um
26	Gl1	Gas	Air	Glass	Y	Y	2-5 um
27	Gl3	Vacuum	-	Glass	Y	Y	2-5 um
28	Gl4	Vacuum	-	Glass	Y	Y	2-5 um
29	Gl5	Vacuum	-	Glass	Y	Y	2-5 um
30	W7	Vacuum	-	W	Y	Y	<1 um
31	Gl7	Vacuum	-	Glass	Y	Y	2-5 um
32	W4	Vacuum	-	W	N	N	<1 um

Figure B-1: Table of test results from Chapter 3, showing values of variables assumed in each test and whether discharges presented.

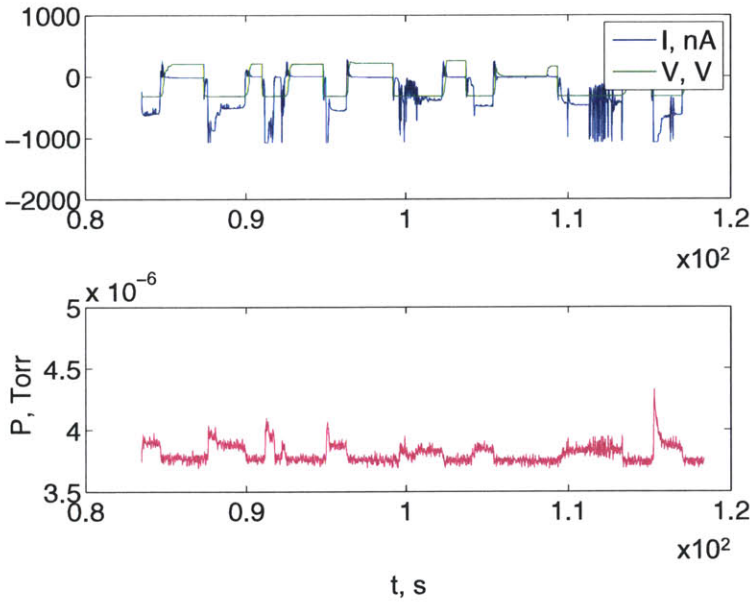

Figure B-2: Emitted current and applied voltage (top) and total chamber pressure (bottom) over a sample of the test of emitter F1. F1 is a nickel emitter that was filled in air with no reservoir. No discharges presented.

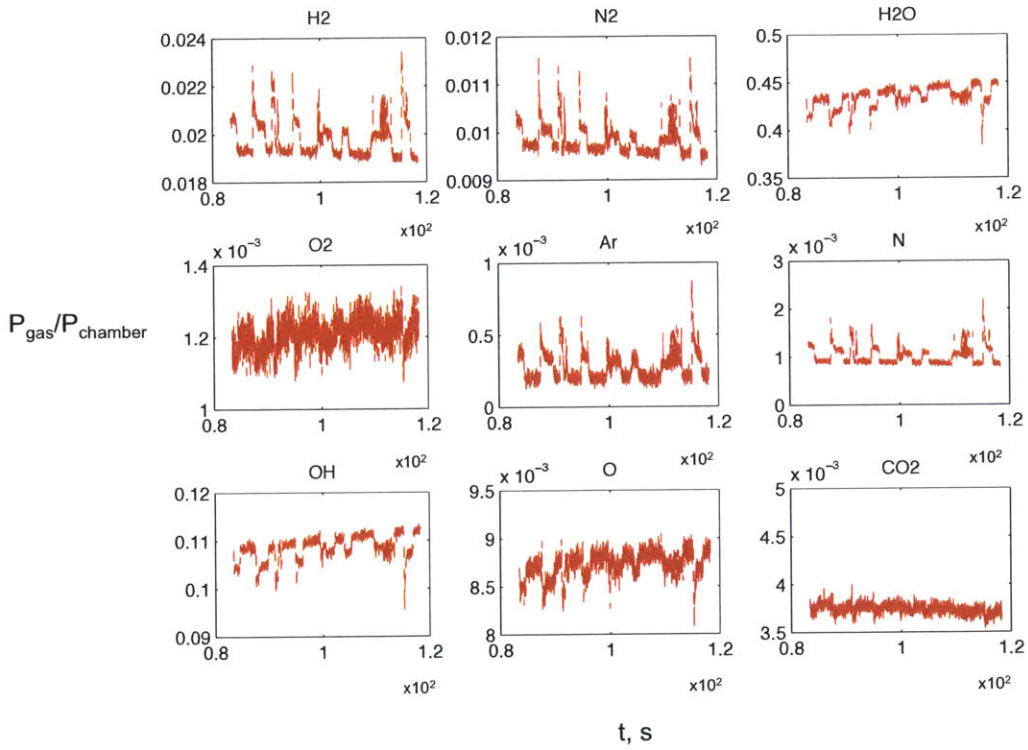

Figure B-3: Gas pressures of species monitored during the test of emitter F1. Peaks in H2, N2, Ar, and N are likely due to the cation and air.

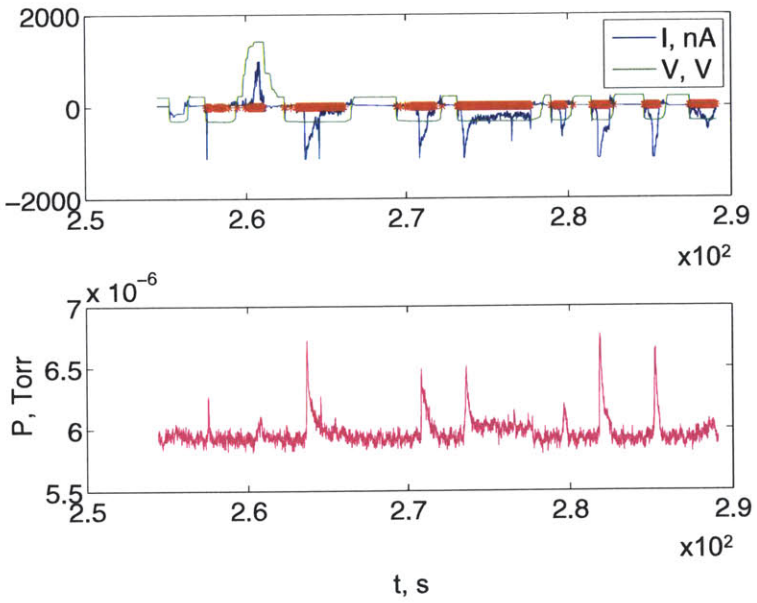

Figure B-4: Emitted current and applied voltage (top) and total chamber pressure (bottom) over a sample of the test of emitter G1. G1 is a nickel emitter that was filled in CO2 with no reservoir. Discharges presented.

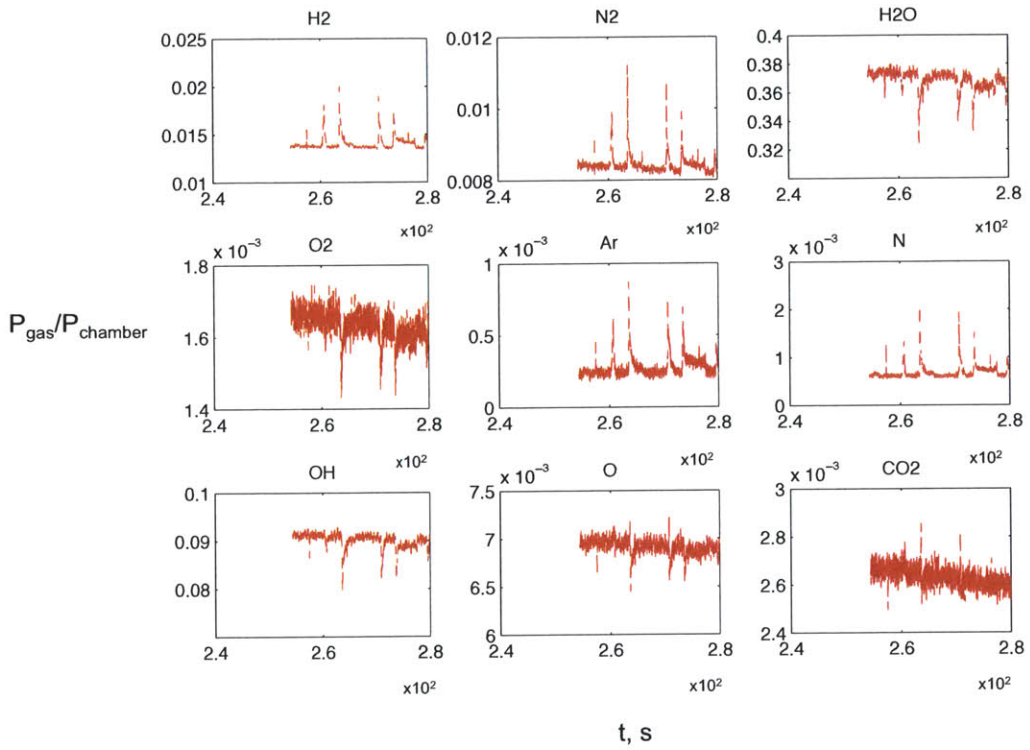

Figure B-5: Gas pressures of species monitored during the test of emitter G1. Peaks in H2, N2, Ar, and N are likely due to the cation and air; slight peaks in CO2 and O are likely from the CO2 filling gas.

Appendix C

Water absorption and nucleation in EMI-BF4

Several ionic liquids of interest are hygroscopic, and as such can absorb significant amounts of water when exposed to humid environments. As the external pressure is decreased (after the satellite is launched into orbit, for instance), the absorption process will reverse and water will begin evaporating from the liquid. As the external pressure is lowered even further and an electric field is applied (during iEPS operation), the water may nucleate and form bubbles within the substrate that could subsequently expand and burst, as discussed in Section 3.4.2. Here, we compute the rate and maximum amount of water absorbed by EMI-BF4 and evaluate conditions under which bubbles could form and burst.

C.1 Water absorption by EMI-BF4

Schenk *et al.* [99] provide an empirical relationship for the molar ratio of absorbed water to ionic liquid in a binary solution, M_w, as a function of time

$$M_w(t) = M_{w,\infty}\left(1 - e^{-kt}\right) \tag{C.1}$$

k is the absorption rate, which is a function of the ionic liquid, the geometry of the container, and the relative humidity. An empirical study by MacMillan *et al.* [10] provides the first results of the interaction of water with aerosolized IL particles. Using tandem nanodifferential mobility analysis and vibrational spectroscopy, MacMillan determined the equilibrium mole fraction, $X_{w,\infty}$, of water absorbed by EMI-BF4 as a function of relative humidity. The reported molecular dynamics simulations showed that the anion had a strong effect on the absorption of water by various ILs.

Taken together, these data permit the calculation of the rate of water absorption in an EMI-BF4–water mixture over a range of relative humidities, and therefore also the maximum expected water content. For EMI-BF4, a reasonable approximation of the maximum mole fraction of water as $t \to \infty$ from MacMillan's results in Figure C-1b is $X_{w,\infty} \approx RH/100$ where RH is the relative humidity. $M_{w,\infty}$ follows from $X_{w,\infty}$ as

$$M_{w,\infty} = \frac{X_{w,\infty}}{1 - X_{w,\infty}} \tag{C.2}$$

Note that k in $M_w(t)$ is proportional to the exposed surface area–to–volume ratio (SV) of the liquid. Schenk studied IL droplets with $SV = 3/r_{drop}$, implying

$$k_{drop} \propto \frac{3}{r_{drop}} \tag{C.3}$$

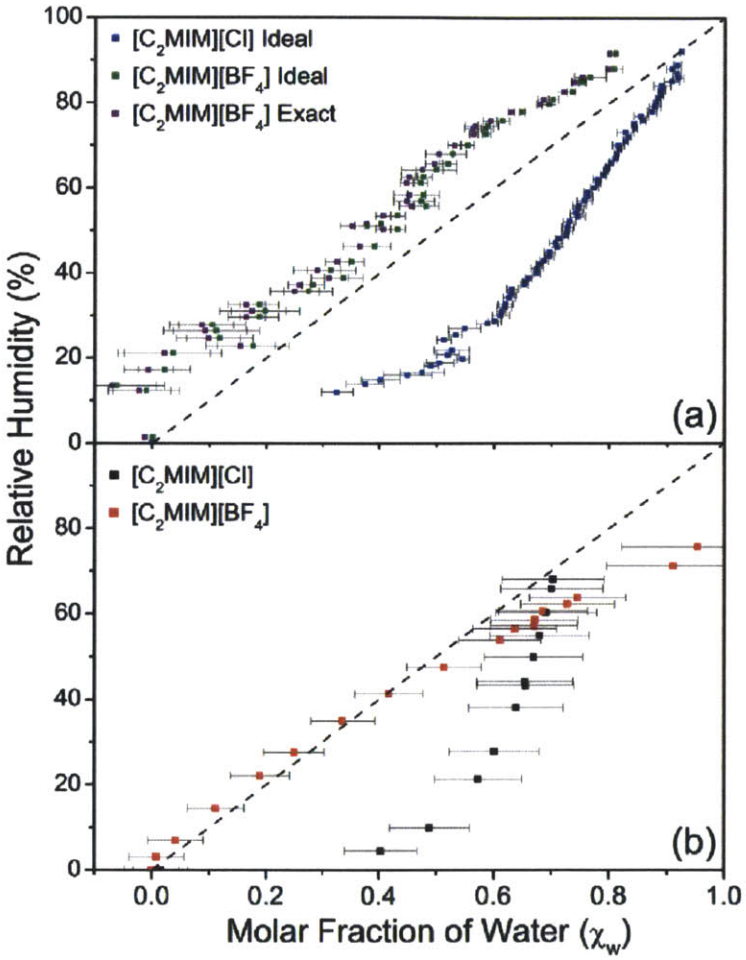

Figure C-1: Equilibrium mole fraction of water in water–EMI-Cl and water–EMI-BF4 solutions as a function of relative humidity [10].

We are interested in absorption by IL contained in porous emitter substrates roughly 1 cm × 1 cm × 2 mm, so $SV_{chip} = 1/x$ where $x = 2$ mm is the chip depth. For this geometry then,

$$k_{chip} \propto \frac{r_{drop}}{3x} k_{drop} \tag{C.4}$$

Taking into account the transient 1-dimensional diffusion of water vapor into the IL, described by Fick's law where the diffusion time is related to the penetration depth as $t \sim x^2$, gives us a third approximation for k:

$$k_{chip,Fick's} \propto \left(\frac{r_{drop}}{3x}\right)^2 k_{drop} \tag{C.5}$$

As part of the work performed in [11], the change in mass of samples of EMI-BF4 under controlled relative humidity environments was measured at regular time intervals until no further change was detected. The data used for comparison to the analytic results was obtained for a porous borosilicate substrate 0.4 mm thick saturated with IL. The diffusivity was computed from fitting the data to a regular diffusion-type equation for the concentration:

$$c(x,t) = C_{sat} e^{-x^2/4Dt} \tag{C.6}$$

with the result $D = 4\text{E}{-12}$ m/s. Both the results from Equation C.1 and The Aerospace Corporation [11] are plotted in Figure C-2 for $RH = 20, 60, 80\%$ and the container geometries described above.

We can make several relevant inferences from these results. First, at 80% RH (a normal day at Cape Canaveral in Florida), from Figure C-2 we see that after equilibrium is reached, $M_w = M_{w,\infty} \approx 4$, which corresponds to an IL-water mixture that is 30% water by volume. Second, the empirical results suggest that absorption

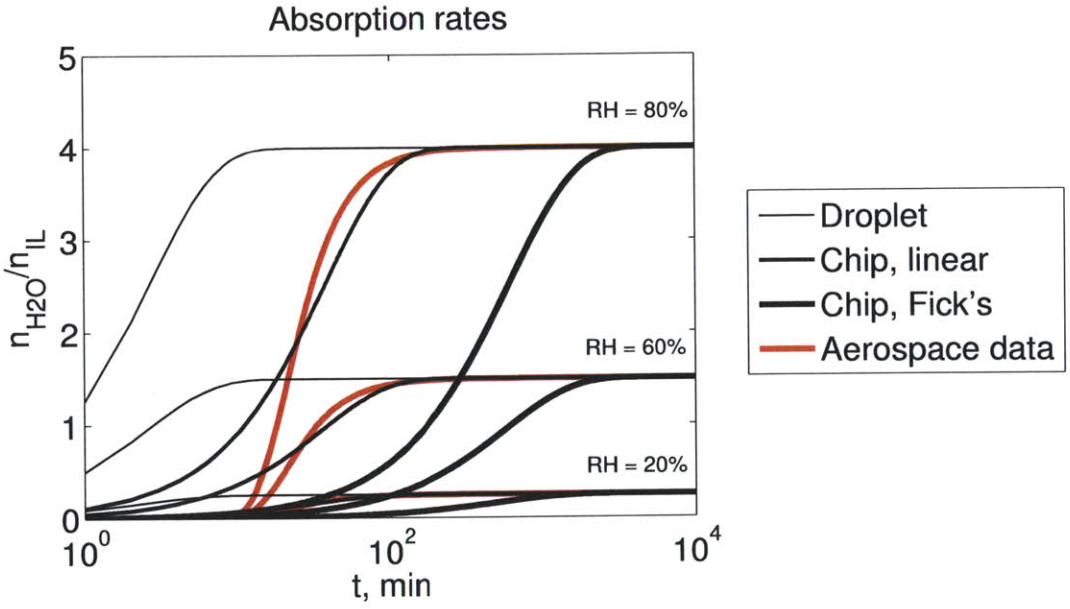

Figure C-2: Ratio of moles of water absorbed to moles of ionic liquid as a function of time and container geometry. The Aerospace Corp. data is from [11].

occurs faster than predicted by regular diffusion. Lastly, neglecting hysteresis in the absorption/desorption rates, the time for the water absorbed from a long wait at the Cape to evaporate once the external pressure is decreased to near-vacuum levels is roughly 3 hours. It would be important then for any iEPS device onboard a spacecraft to have a delay of > 3 h before operation.

C.2 Water vapor nucleation within a pore filled with EMI-BF4

It remains to be seen whether the concentration of water absorbed is such that a decrease in the external pressure will permit the nucleation of a water vapor bubble within the substrate. Bubble formation can be highly problematic in that bubble expansion or bursting can displace liquid from the substrate, leading to discharges through the liquid or liquid bridges that short-circuit the device, and perhaps the vapor released during a bubble burst can raise local pressures to levels that promote electrical discharges.

For a bubble to nucleate and subsist without collapsing, the vapor pressure within must be at least equal to the bubble's own surface tension plus the surface tension exerted by the liquid meniscus at the pore exit and any atmospheric pressure contribution. The balance we seek to solve is then:

$$P_w \geq P_{\gamma,bubble} + P_\gamma + P_a \tag{C.7}$$

and is pictured in Figure C-3. P_w is the vapor pressure, $P_{\gamma,bubble}$ is the surface tension of the bubble, P_γ is the surface tension at the meniscus, and P_a is the atmosphere. Recalling Section 3.4.1, P_γ exerts a tension in wetting liquid, aiding in the formation

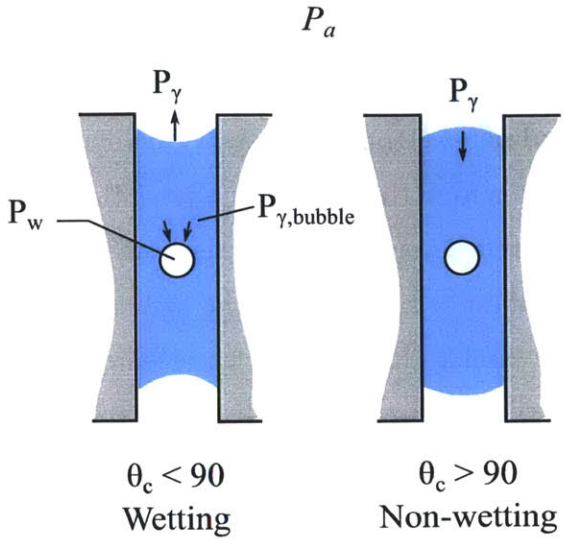

Figure C-3: Pressure balance for bubble within wetting (left) and non-wetting (right) liquids

and expansion of a bubble until the meniscus at the pore exit reaches the spillage condition and the surface tension acts to counter the bubble as in the non-wetting condition. Bubbles that can cause the liquid meniscus to meet the spillage conditions are those with which we are concerned, so now that we understand the pressure balance we will compute P_γ when $\theta_c = \theta_s$. Commonly, $P_{\gamma,bubble}$ is neglected [12], and then we are just seeking the vapor pressure as $P_w = P_w(RH) = P_\gamma$ where P_a was also neglected to give us a worst-case analysis (in reality the bubble's surface tension and any atmospheric pressure would resist the nucleation and expansion).

Henry's law predicts the vapor pressure above an ideal solution: $P_w = X_w k_H P_{w,vap}$ where k_H is the activity coefficient ($k_H = 0.45$ for water in EMI-BF4 [100]) and $P_{w,vap}$ is the vapor pressure of the pure liquid. Figure C-4 shows the vapor pressure of water absorbed by the IL as a function of relative humidity, compared to the surface tension at the pore exit for different pore sizes. For a wetting liquid, $\theta_s = 15$ deg was

assumed; for non-wetting, recall $\theta_s = 90$ deg. The vapor pressure increases with RH, indicating that the water vapor will nucleate more easily at higher concentrations. P_γ for both wetting and non-wetting decreases as the pore radius grows.

The primary conclusion from this analysis is that, although we showed that hygroscopic ILs can absorb significant amounts of water from high-humidity environments, for our pore sizes of interest ($r_{pore} \sim 1$ μm) the high surface tension will overcome the vapor pressure, and bubbles from nucleation of water vapor will not be possible. As a corollary to this last point, provided an ILIS or iEPS device is in a low-humidity

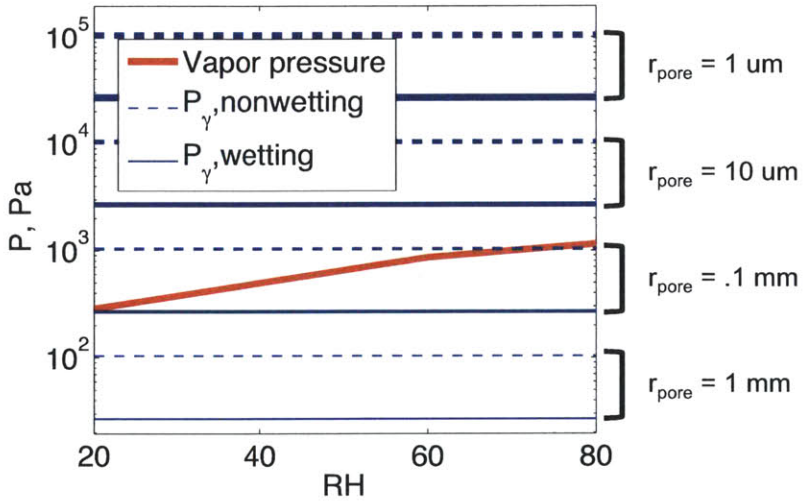

Figure C-4: Vapor pressure of water absorbed by ionic liquid as a function of RH, compared to surface tension for pores of various sizes. Both wetting and non-wetting liquid was considered, where $\theta_{c,wetting} = 15$ deg was assumed.

environment for a time sufficient for the evaporation of the water to occur (> 3 h) before the electric field is applied, it is possible to avoid the formation and subsequent bursting of water vapor bubbles from the substrate, thereby avoiding electrical discharges as water vapor is gently evaporated from the exposed surfaces.

As part of the flight qualification of the colloid thruster selected for use on the

NASA ST-7 LISA Pathfinder mission, a similar analysis was performed by researchers at NASA's Jet Propulsion Laboratory to determine the maximum tolerable level of water contamination [12]. The results, shown in Figure C-5, are consistent with those presented here. However, the larger pore sizes of the colloid system necessitated careful control of the environment prior to launch as the presence of water vapor in amounts greater than 2500 ppm at room temperature could overcome the capillary pressure.

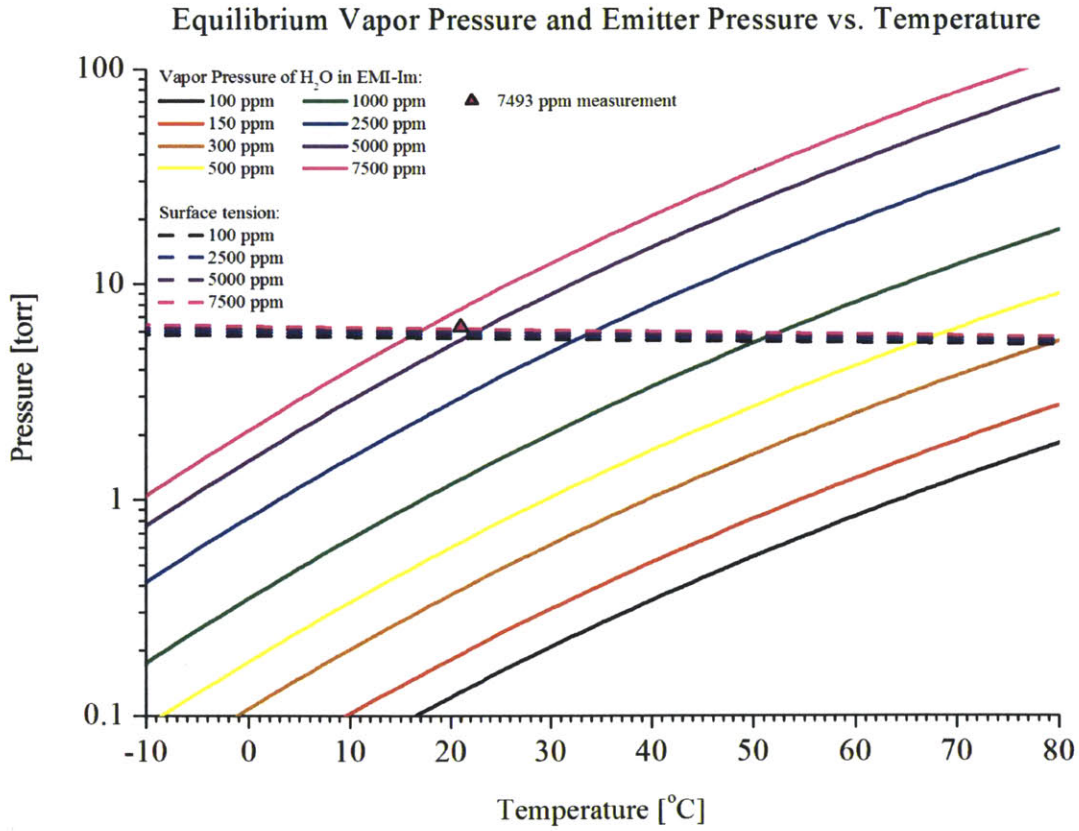

Figure C-5: NASA JPL ST-7 results showing allowable water contamination levels for a range of temperatures [12].

Appendix D

Destabilization of a pool of liquid under the presence of an electric field

An instability can be produced by the applied electric field as the electric traction pulls on a pool of conductive liquid, creating a protuberance which enhances the traction, which in turn causes it to grow further, and so on [88]. This process can become unstable if the surface tension is not strong enough to overcome the traction, ie., if the radius of curvature of the liquid is sufficiently large. We are already familiar with this process as that which produces the Taylor cones required for emission. However, it can lead to the adverse effects of instabilities we observed during testing when applied to a flooded area of liquid pushed from a pore onto a wettable material, for instance.

The balance of the traction force with contributions from the externally applied electric field and the field due to the perturbations themselves with the surface tension

restoring force will indicate liquid pool areas above which we expect instabilities to present [88]. Traction, F_E, is the force per unit area exerted by the normal electric field:

$$F_E = \frac{1}{2}\epsilon_o E_n^2 \tag{D.1}$$

and the restoring force is $F_\gamma = \gamma/R_c$ where R_c is the radius of curvature of the liquid protuberance. The balance we seek to evaluate is then

$$\frac{1}{2}\epsilon_o E_n^2 = \frac{\gamma}{R_c} \tag{D.2}$$

For a small, sinusoidal surface perturbation, or "ripple", the potential outside the liquid obeys $\nabla^2\phi = 0$ and can be represented by a superposition of the potential due to the externally-applied field, E_∞, plus a small perturbation

$$\phi \approx -E_\infty y + \phi_1 e^{-\alpha y}\cos\alpha x \tag{D.3}$$

At the surface where $\phi = 0$,

$$y \approx \frac{\phi_1}{E_n}\cos\alpha x \tag{D.4}$$

from which the surface curvature is

$$\frac{1}{R_c} \approx \left|\frac{d^2y}{dx^2}\right| = \frac{\phi_1\alpha^2}{E_\infty} \tag{D.5}$$

The normal field on the crests where $\cos\alpha x = 1$ is

$$E_y = \frac{-\partial\phi}{\partial y} = E_\infty + \alpha\phi_1 e^{-\alpha y} \tag{D.6}$$

At $\alpha y << 1$, this gives

$$E_y \approx E_\infty + \alpha\phi_1 \tag{D.7}$$

Equation D.2 can now be evaluated with Equations D.5 and D.7, giving the applied field for electric traction instabilities of

$$E_\infty > \sqrt{\frac{\gamma\alpha}{\epsilon_o}} \tag{D.8}$$

where $\alpha = 2\pi/\lambda$ with λ equal to the wavelength of the ripple. E_∞ is plotted in Figure D-1. If long wavelengths are possible, or in other words if the flooded area is large, the field required to cause an instability is small.

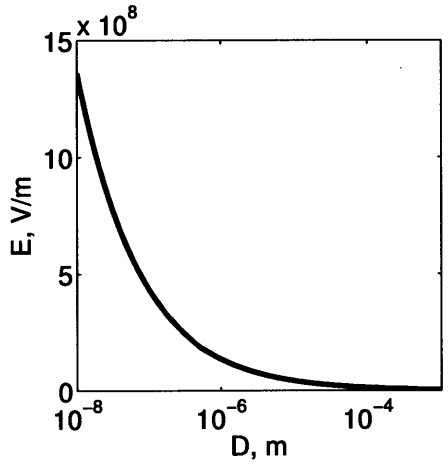

Figure D-1: The electric field for a liquid instability as a function of liquid pool diameter.

Bibliography

[1] A.S.K Pang and B. Twiggs. Citizen Satellites: Sending Experiments into Orbit Affordably, 2011. `http://www.scientificamerican.com/article/citizen-satellites/`.

[2] C. Perez-Martinez, S. Guilet, N. Gogneau, P. Jegou, J. Gierak, and P.C. Lozano. Development of Ion Sources from Ionic Liquids for Microfabrication. *Journal of Vacuum Science and Technology B*, 28(3):L25–L27, 2010.

[3] D. Courtney. *Ionic Liquid Ion Source Emitter Arrays Fabricated on Bulk Porous Substrates for Spacecraft Propulsion.* PhD thesis, Massachusetts Institute of Technology, Boston, MA, 2011.

[4] L.E. Barrosse-Antle, A.M. Bond, R.G. Compton, A.M. O'Mahony, E.I. Rogers, and D.S. Silvester. Voltammetry in Room Temperature Ionic Liquids: Comparisons and Contrasts with Conventional Electrochemical Solvents. *Chemistry, an Asian Journal*, 5(2):202–30, February 2010.

[5] M.M.A. Rahman. Ion Sources for Use in Research and Low Energy Accelerators. *International Journal of Instrumentation Science*, 1(5):63–77, January 2012.

[6] X. Wang and S. Dai. Ionic Liquids as Versatile Precursors for Functionalized Porous Carbon and Carbon-Oxide Composite Materials by Confined Carbonization. *Angewandte Chemie International Edition*, 49:6664–6668, September 2010.

[7] D.M. Goebel and I. Katz. *Fundamentals of Electric Propulsion: Ion and Hall Thrusters.* John Wiley and Sons, 2008.

[8] A. Kieckhafer and L.B. King. Energetics of Propellant Options for High-Power Hall Thrusters. *Journal of Propulsion and Power*, 23(1):21–26, January 2007.

[9] M. Nixon, A. Scheidemantel, A. Punnoose, D. Sanogo, and T. Pho. IRIS Project: Micrometeorite Environment, 2011. http://www.propagation.gatech.edu/ECE6390/project/Fall2011/group5/website/ssp/sat/env/meteorite.html.

[10] A.C. MacMillan, T.M. McIntire, J.A. Freites, D.J. Tobias, and S.A. Nizkorodov. Interaction of Water Vapor with the Surfaces of Imidazolium-Based Ionic Liquid Nanoparticles and Thin Films. *The Journal of Physical Chemistry B*, 116(36):11255–11265, September 2012.

[11] A. Hsu-Schouten, B. Brady, J. DeSain, T. Curtiss, and P.C. Lozano. Thrust Measurements and Propellant Characterization of an Electrospray Thruster. To be published in proceedings of IEPC 2015.

[12] D. Conroy and J.K. Ziemer. Water Contaminant Mitigation in Ionic Liquid Propellant. In *31st International Electric Propulsion Conference*, Ann Arbor, Michigan, 2009.

[13] Digital Solid State Propulsion LLC. Caps-3: Cubesat agile propulsion system preliminary specifications, 2014. http://dsspropulsion.com/caps-3/.

[14] Vacco Industries. Propulsion unit for cubesats specifications, 2014. http://www.vacco.com/images/uploads/pdfs/11044000-01_PUC.pdf.

[15] S. Zhang, N. Sun, X. He, X. Lu, and X. Zhang. Physical Properties of Ionic Liquids: Database and Evaluation. *Journal of Physical and Chemical Reference Data*, 35(4):1475–1517, 2006.

[16] A.L. Ward. Calculations of Cathode-Fall Characteristics. *Journal of Applied Physics*, 33(9):2789–2794, 1962.

[17] A. von Engel. *Ionized Gases.* Clarendon Press, 1965.

[18] R.S. Legge. *Fabrication and Characterization of Porous Metal Emitters for Electrospray Applications.* PhD thesis, Massachusetts Institute of Technology, 2008.

[19] R.G. Jahn. *Physics of Electric Propulsion.* McGraw-Hill Book Company, 1968.

[20] G.P. Sutton and O. Biblarz. *Rocket Propulsion Elements.* Wiley, 8th edition, 2010.

[21] Aerojet Rocketdyne. Electric propulsion sub-systems, 2006. `https://www.rocket.com/propulsion-systems/electric-propulsion`.

[22] Aerojet Rocketdyne. Monopropellant rocket engines, 2006. `https://www.rocket.com/propulsion-systems/monopropellant-rockets`.

[23] J. Mueller, R. Hofer, and J.K. Ziemer. Survey of Propulsion Technologies Applicable to CubeSats. Technical report, NASA, 2010.

[24] Process for limiting orbital debris, 2012. NASA Technical Standard, NASA-STD-8719.14A.

[25] G. Taylor. Disintegration of Water Drops in an Electric Field. *Royal Society of London Proceedings Series A*, 280:383–397, July 1964.

[26] J. Zeleny. The Electrical Discharge from Liquid Points, and a Hydrostatic Method of Measuring the Electric Intensity at their Surfaces. *The Physical Review*, 3(2), 1914.

[27] J.B. Fenn, M. Mann, C.K. Meng, S.K. Wong, and C. Whitehouse. Electrospray Ionization for Mass Spectrometry of Large Biomolecules. *Science*, 246(4926):64–71, 1989.

[28] J. Perel, J.F. Mahoney, R.D. Moore, and Y. Arthur. Research and Development of a Charged-Particle Bipolar Thruster. *AIAA Journal*, 7(3):507–511, 1969.

[29] C. Bartoli and H. von Rohden. A Liquid Caesium Field Ion Source for Space Propulsion. *Journal of Physics D: Applied Physics*, 17(12):2473–2483, 1984.

[30] D.S. Swatik. Production of High Current Density Ion Beams by Electrohydro Dynamic Spraying Techniques. Technical report, Air Force Office of Scientific Research, Urbana, 1969.

[31] M. Tajmar, I. Vasiljevich, F. Plesescu, W. Grienauer, N. Buldrini, M. Betto, and J.G. del Amo. Development of a Porous Tungsten mN-FEEP Thruster. In *Space Propulsion 2010*, San Sebastian, Spain, 2010.

[32] I. Romero-Sanz, R. Bocanegra, and J. Fernandez de la Mora. Source of Heavy Molecular Ions Based on Taylor Cones of Ionic Liquids Operating in the Pure Ion Evaporation Regime. *Journal of Applied Physics*, 94(5):3599–3605, 2003.

[33] P.C. Lozano and M. Martínez-Sánchez. Ionic liquid ion sources: Suppression of electrochemical reactions using voltage alternation. *Journal of Colloid and Interface Sciences*, 280:149–154, 2004.

[34] D.G. Courtney, H. Li, P. Maqueo, T. Fedkiw, and P.C. Lozano. On the Validation of Porous Nickel as Substrate Material for Electrospray Ion Propulsion. In *AIAA Joint Propulsion Conference*, Nashville, TN, July 2010.

[35] P.R. Chiarot, P. Sullivan, and R.B. Mrad. An Overview of Electrospray Applications in MEMS and Microfluidic Systems. *Journal of Microelectromechanical Systems*, 20(6):1241–1249, 2011.

[36] A.N. Zorzos and P.C. Lozano. The Use of Ionic Liquid Ion Sources in Focused Ion Beam Applications. *Journal of Vacuum Science and Technology B*, 26(6):2097–2102, 2008.

[37] J. Gierak. Focused Ion Beam Technology and Ultimate Applications. *Semiconductor Science and Technology*, 24(4), 2009.

[38] M. Gamero-Castaño and V. Hruby. Electrospray as a Source of Nanoparticles for Efficient Colloid Thrusters. *Journal of Propulsion and Power*, 17(5):977–987, 2001.

[39] P.C. Lozano, M. Martínez-Sánchez, and V. Hruby. *Encyclopedia of Aerospace Engineering: Electrospray Propulsion.* John Wiley and Sons, Inc., 2010.

[40] J. Fuller, R.T. Carlin, and R.A. Osteryoung. The Room Temperature Ionic Liquid 1 -Ethyl-3-methylimidazolium Tetrafluoroborate: Electrochemical Couples and Physical Properties. *Journal of the Electrochemical Society*, 144(11), 1997.

[41] T.P. Fedkiw and P.C. Lozano. Development and Characterization of an Iodine Field Emission Ion Source for Focused Ion Beam Applications. *Journal of Vacuum Science & Technology B: Microelectronics and Nanometer Structures*, 27(6):2648–2653, 2009.

[42] P.C. Lozano. Energy Properties of an EMI-Im Ionic Liquid Ion Source. *Journal of Physics D: Applied Physics*, 39:126–134, January 2006.

[43] J. Orloff, L.W. Swanson, and M. Utlaut. Fundamental Limits to Imaging Resolution for Focused Ion Beams. *Journal of Vacuum Science & Technology B*, 14(3759), 1996.

[44] P.C. Lozano and M. Martínez-Sánchez. Efficiency Estimation of EMI-BF 4 Ionic Liquid Electrospray Thrusters. In *41st AIAA Joint Propulsion Conference*, number July, 2005.

[45] K.E. Clark. Survey of Electric Propulsion Capability. *Journal of Spacecraft and Rockets*, 12(11):641–654, November 1975.

[46] S.G. Rosen. Colloid and Pulsed Plasma Thrusters for Spacecraft Propulsion. In *AIAA/SAE 9th Propulsion Conference*, Las Vegas, 1973.

[47] J.K. Ziemer, T.M. Randolph, G.W. Franklin, V. Hruby, D. Spence, N. Demmons, T. Roy, E. Ehrbar, J. Zwahlen, R. Martin, and W. Connolly. Colloid Micro-Newton Thrusters for the Space Technology 7 Mission. In *2010 IEEE Aerospace Conference*, March 2010.

[48] J. Perel, T. Bates, J. Mahoney, R.D. Moore, and A.Y. Yahiku. Research on a Charged Particle Bipolar Thrustor. In *AIAA Electric Propulsion and Plasmadynamics Conference*, Colorado Springs, 1967.

[49] J Perel, J Mahoney, and HL Daley. Duration Test of an Annular Colloid Thruster. In *AIAA Electric Propulsion Conference*, Bethesda, MD, 1972.

[50] AG Bailey, JE Bracher, and HJ Von Rohden. A Capillary-Fed Annular Colloid Thruster. *Journal of spacecraft and ...*, 9(7):518–521, 1972.

[51] R. Krpoun and H.R. Shea. Integrated out-of-plane nanoelectrospray thruster arrays for spacecraft propulsion. *Journal of Micromechanics and Microengineering*, 19, 2009.

[52] G. Lenguito. *Multiplexed Electrosprays for Space Propulsion Applications.* PhD thesis, Yale University, 2013.

[53] R. Legge and P.C. Lozano. Performance of Heavy Ionic Liquids with Porous Metal Electrospray Emitters. In *44th AIAA Joint Propulsion Conference*, Hartford, CT, 2008.

[54] L.E. Perna. Design and Manufacturing of an Ion Electrospray Propulsion System Package and Passively-Fed Propellant Supply. Master's thesis, Massachusetts Institute of Technology, 2014.

[55] R. de Levie. On Porous Electrodes in Electrolyte Solutions. *Electrochimica Acta*, 8:751–780, 1963.

[56] J. Bockris, A. Reddy, and M. Gamboa-Aldeco. *Modern Electrochemistry*, volume 2A. Springer Science + Business Media, 2 edition, 2000.

[57] M Faraday. *Experimental Researches in Electricity.* Richard and John Edward Taylor, 1844.

[58] J. Koryta, J. Dvorak, and L. Kavan. *Principles of Electrochemistry.* Wiley Chichester, 1993.

[59] C. Merlet, B. Rotenberg, P.A. Madden, P.L. Taberna, P. Simon, Y. Gogotsi, and M. Salanne. On the Molecular Origin of Supercapacitance in Nanoporous Carbon Electrodes. *Nature Materials*, 11(4):306–310, March 2012.

[60] P. Bai and M.Z. Bazant. Charge Transfer Kinetics at the Solid-Solid Interface in Porous Electrodes. *Nature Communications*, 3585(5), 2014.

[61] A.T. Blades, M.G. Ikonomou, and P. Kebarle. Electrospray Mass Spectrometry. Electrospray as an Electrolysis Cell. *Analytical Chemistry*, 63(19):2109–2114, 1991.

[62] G.J. Van Berkel and F.M. Zhou. Characterization of an Electrospray Ion Source as a Controlled-Current Electrolytic Cell. *Analytical Chemistry*, 67(17):2916–2923, 1995.

[63] P. Rai-Choudhury, editor. *Handbook of Microlithography, Micromachining, and Microfabrication*, volume 2. SPIE PRESS Monograph, 1997.

[64] D.G. Courtney, H. Li, and P.C. Lozano. Electrochemical Micromachining on Porous Nickel for Arrays of Electrospray Ion Emitters.. *Journal of Microelectromechanical Systems*, 22(2):471–482, April 2012.

[65] D.G. Courtney, H.Q. Li, and P.C. Lozano. Emission Measurements from Planar Arrays of Porous Ionic Liquid Ion Sources. *Journal of Physics D: Applied Physics*, 45(48), December 2012.

[66] P.C. Lozano and M. Martínez-Sánchez. Ionic liquid ion sources: Characterization of externally wetted emitters. *Journal of Colloid and Interface Sciences*, 282:415–421, 2005.

[67] P.C. Lozano and M. Martínez-Sánchez. On the dynamic response of externally wetted ionic liquid ion sources. *Journal of Physics D: Applied Physics*, 38(14):2371–2377, 2005.

[68] S. Castro and J. Fernandez de la Mora. Effect of Tip Curvature on Ionic Emissions from Taylor Cones of Ionic Liquids from Externally Wetted Tungsten Tips. *Journal of Applied Physics*, 105(3):903–908, 2009.

[69] K. Masuyama and P.C. Lozano. Bimodal Propulsion System Using Ionic Liquid Propellant for Pico- and Nano-satellite Applications. *49th AIAA Joint Propulsion Conference*, July 2013.

[70] V. Shmelev. Propagation Modes of an Electrical Discharge Along a Liquid Jet. *IEEE Transactions on Plasma Science*, 36(5):2522–2527, 2008.

[71] M. Yamashita and J.B. Fenn. Negative Ion Production with the Electrospray Ion Source. *The Journal of Physical Chemistry*, 88(20):4611–4615, 1984.

[72] M. Abonnenc, L. Qiao, B. Liu, and H.H. Girault. Electrochemical Aspects of Electrospray and Laser Desorption/Ionization for Mass Spectrometry. *Annual Review of Analytical Chemistry*, 3:231–254, 2010.

[73] D.P.H. Smith. The Electrohydrodynamic Atomization of Liquids. *IEEE Transactions on Industry Applications*, IA-22(3):527–535, 1986.

[74] P.B. Gray. Ignition of a Liquid Fuel Jet by an Electrical Discharge Propagating along the Jet. Master's thesis, North Carolina State University, 2010.

[75] Y. Yang, Y.I. Cho, and A. Fridman. *Plasma Discharge in Liquid: Water Treatment and Applications.* CRC Press, 2012.

[76] H Akiyama. Streamer Discharges in Liquids and Their Applications. *IEEE Transactions on Dielectrics and Electrical Insulation*, 7(5):646–653, 2000.

[77] Y.P. Raizer. *Gas Discharge Physics.* Springer-Verlag Berlin Heidelberg, 1991.

[78] H.Y. Fan. The Transition from Glow Discharge to Arc. *Physical Review*, 55:769—-775, 1939.

[79] L.B. Loeb. *Fundamental Processes of Electrical Discharge in Gases.* J. Wiley and Sons, 1939.

[80] H. Raether. The development of the electron avalanche in the radio channel. *Journal of Physics*, 112:464–489, 1939.

[81] T.J. Lewis. A New Model for the Primary Process of Electrical Breakdown in Liquids. *IEEE Transactionson Dielectrics and Electrical Insulation*, 5(3):306–315, 1998.

[82] H.R. Zeller and E. Cartier. *Electron Scattering and Dielectric Breakdown in Liquid and Solid Dielectrics.* Plenum Press, New York, 1988.

[83] N.Y. Babaeva and M.J. Kushner. Structure of Positive Streamers Inside Gaseous Bubbles Immersed in Liquids. *Journal of Physics D: Applied Physics*, 42(13), July 2009.

[84] A.L. Ward. Ionization, Diffusion, and Drift Velocities in a Pulsed Townsend Discharge. *Journal of Applied Physics*, 36(4):1291–1294, 1965.

[85] J.S. Townsend. *Electricity in Gases.* Clarendon Press, 1915.

[86] V. Baglin, J. Bojko, O. Gröbner, B. Henrist, N. Hilleret, C. Scheuerlein, and M. Taborelli. The Secondary Electron Yield of Technical Materials and Its Variation with Surface Treatments. In *Proceedings of EPAC*, pages 217–221, Vienna, 2000.

[87] J.P. Paraknowitsch, A. Thomas, and M. Antonietti. A Detailed View on the Polycondensation of Ionic Liquid Monomers Towards Nitrogen Doped Carbon Materials. *Journal of Materials Chemistry*, 20(32):6746, 2010.

[88] M. Martínez-Sánchez. Colloidal engines, appendix, 2004. Retrieved from online lecture notes. `http://ocw.mit.edu/courses/aeronautics-and-astronautics/16-522-space-propulsion-spring-2004/lecture-notes/lecture23_25.pdf`.

[89] A.W. Adamson and A.P. Gast. *Physical Chemistry of Surfaces.* John Wiley & Sons Inc, 6th edition, 1967.

[90] OS Owete and WE Brigham. Flow of Foam Through Porous Media. Technical report, US Department of Energy, 1984.

[91] M. Zhang and S.E. Burns. Surfactant Effects on the Transport of Air Bubbles in Porous Media. *Environmental Geotechnics*, pages 121–131, 2000.

[92] M. Gamero-Castaño. The Structure of Electrospray Beams in Vacuum. *Journal of Fluid Mechanics*, 604:339–368, May 2008.

[93] J.F. de la Mora. The Fluid Dynamics of Taylor Cones. *Annual Review of Fluid Mechanics*, 39(1):217–243, January 2007.

[94] A. Gañán Calvo. Cone-Jet Analytical Extension of Taylor's Electrostatic Solution and the Asymptotic Universal Scaling Laws in Electrospraying. *Physical Review Letters*, 79(2):217–220, July 1997.

[95] I. Hayati, A. Bailey, and T.F. Tadros. Investigations into the Mechanism of Electrohydrodynamic Spraying of Liquids II. Mechanism of Stable Jet Formation and Electrical Forces Acting on a Liquid Cone. *Journal of Colloid and Interface Science*, 117(1):222–230, 1987.

[96] M. Martínez-Sánchez. Electrostatic thrusters, 2004. Retrieved from online lecture notes. `http://ocw.mit.edu/courses/aeronautics-and-astronautics/16-522-space-propulsion-spring-2004/lecture-notes/lecture13_14.pdf`.

[97] J.K. Ziemer, C.M. Marrese-Reading, M. Anderson, G. Plett, and J. Polk. Colloid Thruster Propellant Stability After Radiation Exposure. In *39th AIAA Joint Propulsion Conference*, number July 2003, pages 1–9, Huntsville, 2003.

[98] D. Allen, G. Baston, A.E. Bradley, T. Gorman, A. Haile, I. Hamblett, J.E. Hatter, M.J.F. Healey, B. Hodgson, R. Lewin, K.V. Lovell, B. Newton, W.R. Pitner, D.W. Rooney, D. Sanders, K.R. Seddon, H.E. Sims, and R.C. Thied. An Investigation of the Radiochemical Stability of Ionic Liquids. *Green Chemistry*, 4(2):152–158, April 2002.

[99] J. Schenk, U. Panne, and M. Albrecht. Interaction of Levitated Ionic Liquid Droplets with Water. *The Journal of Physical Chemistry B*, 116(48):14171–7, December 2012.

[100] C. Jork, C. Kristen, D. Pieraccini, A. Stark, C. Chiappe, Y.A. Beste, and W. Arlt. Tailor-Made Ionic Liquids. *The Journal of Chemical Thermodynamics*, 37(6):537–558, June 2005.